The metabolic basis of cell identity in the pulmonary arteries and the right ventricle in pulmonary arterial hypertension

by

Yongneng Zhang

A thesis submitted in partial fulfillment of the requirements for the degree of

Doctor of Philosophy

Department of Medicine

University of Alberta

Abstract

Pulmonary arterial hypertension (PAH) is an incurable disease characterized by profound pulmonary vascular remodeling, including the development of plexogenic lesions (which is the hallmark of PAH) that results in lumen obliteration, raising the pulmonary vascular resistance (PVR) and the right ventricle (RV) afterload. While initially this leads to RV hypertrophy, it eventually advances to RV dilatation, decompensation and death.

One of the biggest challenges in PAH research is the lack of good animal models that mimic human PAH with severe high mean PA pressure (mPAP) and plexogenic lesions. In Chapter 2, we studied a cohort of 60 PAH patients and found Sirtuin 3 (Sirt3, a mitochondrial deacetylase) and uncoupling protein 2 (Ucp2, an atypical uncoupling protein enabling mitochondrial calcium entry) loss of function SNPs, often both found in the same patient in a homozygous or heterozygous manner. The presence of these SNPs correlated positively with PAH severity and 10 years outcomes (death and transplantation). We then generated a mouse model lacking both Sirt3 and Ucp2. We found that the double KO mice have an increasing severity of PAH (mPAP, right ventricular hypertrophy/dilatation and extensive vascular remodeling, including inflammatory plexogenic lesions as removed from wildtype to heterozygous to KO for both genes), along with insulin resistance. The suppressed mitochondrial function (decreased respiration, increased mitochondrial membrane potential) also exhibited a similar gene-dose dependent effect. This was the first mouse model ever described exhibiting spontaneous severe PAH with frequent plexogenic lesions and provided further support to the metabolic theory of PAH that our group had recently proposed.

In Chapter 3, we focused on the transition from compensated RV hypertrophy (cRVH) to decompensated RV hypertrophy (dRVH), because the main driver of mortality and morbidity in PAH is not the degree of PA pressure increase, but rather the function of the RV. What makes the transition from cRVH to dRVH and how one RV is more prone to failure than another RV is unknown. We hypothesized that a transition from cardiac fibroblasts (cFB) to cardiac myofibroblasts (cMFB) underlies this mechanism. We studied a cohort of rats with monocrotaline-induced pulmonary hypertension (PHT). Compared to cRVH, dRVH rats still kept high mPAP, but had lower RV systolic pressure, higher right atrial pressure, lower cardiac output, lower TAPSE and higher RV end-diastolic diameter. We found that the dRVH has an increased myofibroblast number compared with normal RV and cRVH. The dRVH myofibroblasts had increased proliferation indices and decreased mitochondrial function and mitochondrial calcium (mCa^{++}) compared with normal and cRVH cFB. It has been shown that the decrease in mCa^{++} is related to mitochondrial calcium uptake 1 (MICU1) methylation and lack of UCP2. The dRVH cMFB had increased MICU1 methylation (shown by protein arginine methyltransferase 1 (PRMT1) and asymmetric dimethylarginine (ADMA) levels) and decreased UCP2, compared to normal RV and cRVH cFB. In human RV tissue (Control, cRVH, dRVH, n=5 for each), we confirmed the result of cMFB numbers, PRMT1 and UCP2 levels as what we found in the rat model. In a cohort of 25 patients with PHT (secondary PHT vs Pulmonary Arterial Hypertension) undergoing both catheterization and echocardiography, we found that carriers of this germline UCP2 loss of function SNP, had decreased TAPSE to non-carriers despite similar PA pressures.

This thesis made two contributions to the PAH field. First, it showed a provocative correlation between the loss-of-function SNPs of SIRT3 and UCP2 with the severity of disease in patients

with PAH. We also created a novel mouse model in which to explore the true pathology of PAH since it was the first animal model with spontaneous plexogenic lesions and insulin resistance, both features of human PAH not presented in any other models. Second, we explored the mechanism of the transition from cRVH to dRVH in PAH, and we found the transformation from cFB to cMFB underlines this transition. We confirmed these findings in human RVs. This was important because we showed that this transition was not due to cardiomyocyte failure as thought until now. Furthermore, we showed that the loss-of-function SNP of UCP2 correlates with worse RV function in PAH patients regardless of the degree of mPAP, making this UCP2 SNP a potential biomarker that could predict RV function in PAH patients, if confirmed in larger cohorts.

Preface

This thesis is an original work by Yongneng Zhang. The work presented in the dissertation was mainly carried out in Dr. Evangelos Michelakis's laboratory in the University of Alberta, Edmonton, AB, Canada. Our work with human clinical data and human blood was performed with permission from the University of Alberta Human Research Ethics Board (HREB). All animal experiments were conducted in accordance with the Canadian Council for Animal Care guidelines, with protocols approved by the Animal Care and Use Committee (ACUC) at the University of Alberta.

Chapter 2 has been published in the Journal of the American Heart Association. Chapter 3 will be submitted to a peer-reviewed journal soon.

Dedications

This dissertation is dedicated to my beloved wife Ning, my son Zhenxuan, Matthew, my daughter Joanna, my mom, parents-in-law and two elder brothers who have given me constant supports and encouragement during my graduate study.

Acknowledgements

First, I would like to thank my supervisor, Dr. Evangelos D. Michelakis, whose mentorship and continuous guidance have inspired me in many ways and have guided me into a better scientist and person. I appreciate all his contributions of time, ideas, patience and funding to make the completion of my PhD study possible.

I am grateful for the supports and contributions to my projects from my committee members, Dr. Gopinath Sutendra and Dr. John R. Ussher, for their leadership and valuable insight throughout my studies. I also want to express my gratitude to all the members in Dr. Michelakis's and Dr. Sutendra's lab Aris, Sotirios, Bruno, Mo, Vikram, Areli, Saymon, Subhash, Runtai, Guocheng, Joseph, Paul, Linda, Alois, Yongsheng and Yuan for their friendship and hard work together, which made this journey a very pleasant one.

Finally, I would like to gratefully acknowledge the Li Ka Shing Foundation and the Motyl Graduate Studentships in Cardiac Sciences for providing funding and information supports. Without the generous sponsorship, none of this would be possible.

Table of Contents

List of Tables

List of Figures

List of Abbreviations

PAH	pulmonary Arterial Hypertension
PA	pulmonary artery
PVR	pulmonary vascular resistance
RV	right ventricular
BMPRII	bone morphogenetic protein receptor type II
TGFβ	transforming growth factor beta
PAECs	pulmonary arterial endothelial cells
PASMCs	pulmonary artery smooth muscle cells
DLL	Delta-like
ICD	intracellular domain
PDH	pyruvate dehydrogenase
mROS	mitochondrial reactive oxygen species
ETC	electron transport chain
HIF-1α	hypoxia inducible factor 1
NFAT	nuclear factor of activated T cells
MTP	mitochondrial permeability transition pore
SIRT3	sirtuin3
UCP2	uncoupling Protein 2
MCU	mitochondrial calcium uniporter
mCa^{++}	mitochondrial calcium
PHT	pulmonary hypertension
PDK	pyruvate Dehydrogenase kinase

DCA	dichloroacetate
iPAH	idiopathic pulmonary artery hypertension
SSc	systemic sclerosis
SNP	Single nucleotide polymorphism
VWF	von Willebrand factor
α-SMA	alpha-smooth muscle actin
PDE5i	phosphodiesterase 5 inhibitor
cRVH	compensated right ventricular hypertrophy
dRVH	decompensated right ventricular hypertrophy
mPAP	mean PA pressure
LV	left ventricle
LVH	left ventricle hypertrophy
DTT	dithiothreitol
OCR	oxygen consumption rate
ECAR	extracellular acidification rate
TMRM	tetramethyl-rhodamine methyl-ester perchlorate
ΔΨm	mitochondrial membrane potential
TAPSE	tricuspid Annular Plane Systolic Excursion
CO	cardiac output
PAD	pulmonary artery diameter
PAVTI	pulmonary artery velocity time integral
HR	heart rate
aPAH	associated PAH

SSc	systemic sclerosis
cFB	cardiac fibroblasts
cMFB	cardiac myofibroblasts
CM	cardiomyocytes
MICU1	mitochondrial calcium uptake 1
PRMT1	protein arginine methyltransferase 1
ADMA	asymmetric dimethylarginine
SDH	succinate dehydrogenase
ACL	ATP-citrate lyase
TNFα	tumour necrosis factor alpha
RVSP	right ventricle systolic pressure
KDH	ketoglutarate Dehydrogenase
SDH	succinate Dehydrogenase
ACL	ATP-citrate lyase
RVEDD	right ventricular end-diastolic diameter
LDHA/B	lactate dehydrogenase A/B
MCT1/4	monocarboxylate transporter 1/4

Chapter one

Introduction

Pulmonary Arterial Hypertension (PAH) is a progressive vascular disease with a high mortality rate. It is characterized by pulmonary vascular remodeling that results in lumen obliteration, raising the pulmonary vascular resistance (PVR) and while initially it leads to right ventricular (RV) hypertrophy, it then advances to RV dilatation, fibrosis and death from heart failure[1]. PAH is also a multiorgan disease. In addition to the pulmonary artery vascular and RV remodeling, several organs are involved in PAH including activated T cells (inflammation), bone-marrow-derived precursor cells (contributing to plexogenic lesions) and insulin resistance[2].

1.1. Pulmonary arteries

1.1.1. Pathology: PAH is characterized by profound pulmonary vascular remodeling, including muscularization of small pulmonary arteries (PAs), hypertrophy of the vessel wall, and the development of plexogenic lesions that results in lumen obliteration, raising the pulmonary vascular resistance (PVR). The vascular wall in the remodeled PAs shows a proliferative and anti-apoptotic diathesis driven by the activation of many transcription factors, for example, the NFAT (Nuclear factor of activated T-cells)[3,4], HIF (hypoxia inducible factor)[5], STAT3 (Signal transducer and activator of transcription 3)[6], etc. The pathology of the PAs in the lungs of PAH patients is complex and includes small pulmonary arterial medial and adventitial thickening and occlusive neointima. In addition, the plexogenic lesion which consist of anarchies proliferation of endothelial, smooth muscle cells, and fibroblasts in and around occluded PAs is a hall mark of the pathology of severe PAH in patients[7]. Infiltration of the perivascular space or vascular wall with immune and inflammatory cells is more prevalent than previously thought. These changes cause a vascular remodeling that eventually leads to a narrowing or obliteration of the vascular lumen.

1.1.2. Cell fate related PAH theory: Many theories have been proposed, but none of them achieves a comprehensive explanation of the whole spectrum of findings. We will just briefly discuss two of the best supported theories, as well as the only comprehensive theory that has been proposed so far.

1.1.2.1. BMPRII mutation and TGFb signaling pathway: The first theory describes an overall suppression of the bone morphogenetic protein receptor type II (BMPRII) axis, whether due to mutations or more commonly due to a malfunction of its down signalling[8]. The dysregulation of the BMPRII- Smad1/5/8 pathway promotes a pro-proliferative and anti-apoptotic diathesis in the cells of the pulmonary artery wall[9]. Although the TGF axis is very important in embryo development and changes of cell identity, this has not been explored in PAH so far. Nevertheless, this theory suggests that at first the pulmonary artery endothelial cells (PAECs) become apoptotic, followed by a proliferative phase, perhaps as an attempt to repair, practically in the pulmonary artery smooth muscle cells (PASMCs)[10].

1.1.2.2. JAG1-Notch3 signaling: Another mechanism involves JAG1-Notch3 signaling, another pathway that also involves downstream SMADs and epigenetic mechanisms. NOTCH3 is a member of the Notch receptor family (NOTCH1 to NOTCH4) that binds to the ligands Jagged (JAG-1 and JAG-2) and Delta-like (DLL-1, DLL-3, and DLL-4). NOTCH3 is mostly expressed on PASMCs and is up regulated in animal and human PAH and plays a central role in PAH development in animal models[11]. JAG-1 binding to NOTCH3 induces NOTCH3 cleavage and release of its intracellular domain (ICD), which translocate into the nucleus and activates target genes. Therefore, the proliferation of PASMC is increased and PASMC were shifted to an

undifferentiated smooth muscle cell phenotype[12]. Once again, like BMPRII, the implication on cell identity regulation, plexogenic lesion pathogenesis, insulin resistance, and RV decompensation remains unknown.

1.1.2.3. Metabolic theory: Our group proposed the metabolic theory of PAH that suggested that a suppression in mitochondrial function can explain the cellular anti-apoptotic and pro-proliferative diathesis within the wall of the pulmonary arteries, the RV myocardium dysfunction, the T cell activation (a feature of human and animal PAH and insulin resistance)[2]. For example, we found that PAH PASMC mitochondria have suppressed glucose oxidation and increased cytoplasmic glycolysis (similar to the cancer Warburg effect) due to inhibition of the glucose oxidation gatekeeping enzyme PDH[13]. Therefore, the production of mitochondrial reactive oxygen species (mROS: produced in electron transport chain (ETC) complexes) is decreased, which activates transcription factors that are important in human and animal PAH, including the nuclear factor of activated T cells 2 (NFATc2)[13] and hypoxia inducible factor-1a (HIF-1a)[5,14]. Also, the Krebs cycle–derived α-ketoglutarate (αKG) can regulate HIF-1α because it is a required cofactor for the prolyl-hydroxylases that destabilize HIF-1α[15]. Thus, the primary changes in mitochondrial function occurring in PAH-PASMCs decreases mROS and αKG production, resulting in aerobic HIF-1α stabilization and activation[5,14]. The activation of NFATc2 and HIF1α directly promotes proliferation[2]. Moreover, suppressed mitochondrial PDH activity and glucose oxidation also cause increased mitochondrial membrane potential, inhibition of the mitochondrial permeability transition pore (MTP), and confinement of proapoptotic mediators such as cytochrome c and apoptosis-inducing factor to the mitochondria, leading to apoptosis resistance[16]. Sirtuin3 (SIRT3) is a mitochondrial deacetylase, regulating the activity of several metabolic enzymes and ETC

components[17]. Uncoupling protein 2 (UCP2) is a component of the mitochondrial calcium transporter (MCU), thus, regulating the function of several mitochondria and Krebs cycle enzymes[18,19]. Inhibition of UCP2 leads to a decrease in mitochondrial calcium (mCa^{++}). Our previous research showed that mice lacking either SIRT3 or UCP2 develop pulmonary hypertension (PHT) and vascular remodeling[20,21].

A more recent study from our group in a cohort of PAH patients supported our metabolic theory. We found that administration of the Pyruvate dehydrogenase kinase (PDK, phosphorylates and deactivates PDH) inhibitor dichloroacetate (DCA) to patients with PAH already on approved iPAH therapies, reduced mean PA pressure and PVR and improved functional capacity[22]. However, patients that had a loss of function SNPs for UCP2 and SIRT3 fail to respond to DCA, because as can be seen as the schematic below (**Fig 1.1)**[22]. In those patients, PDH was inhibited not just by PDK, but also by independent mechanisms, including increased acetylation (by the lack of SIRT3) and decrease mCa^{++} (by the lack of UCP2).

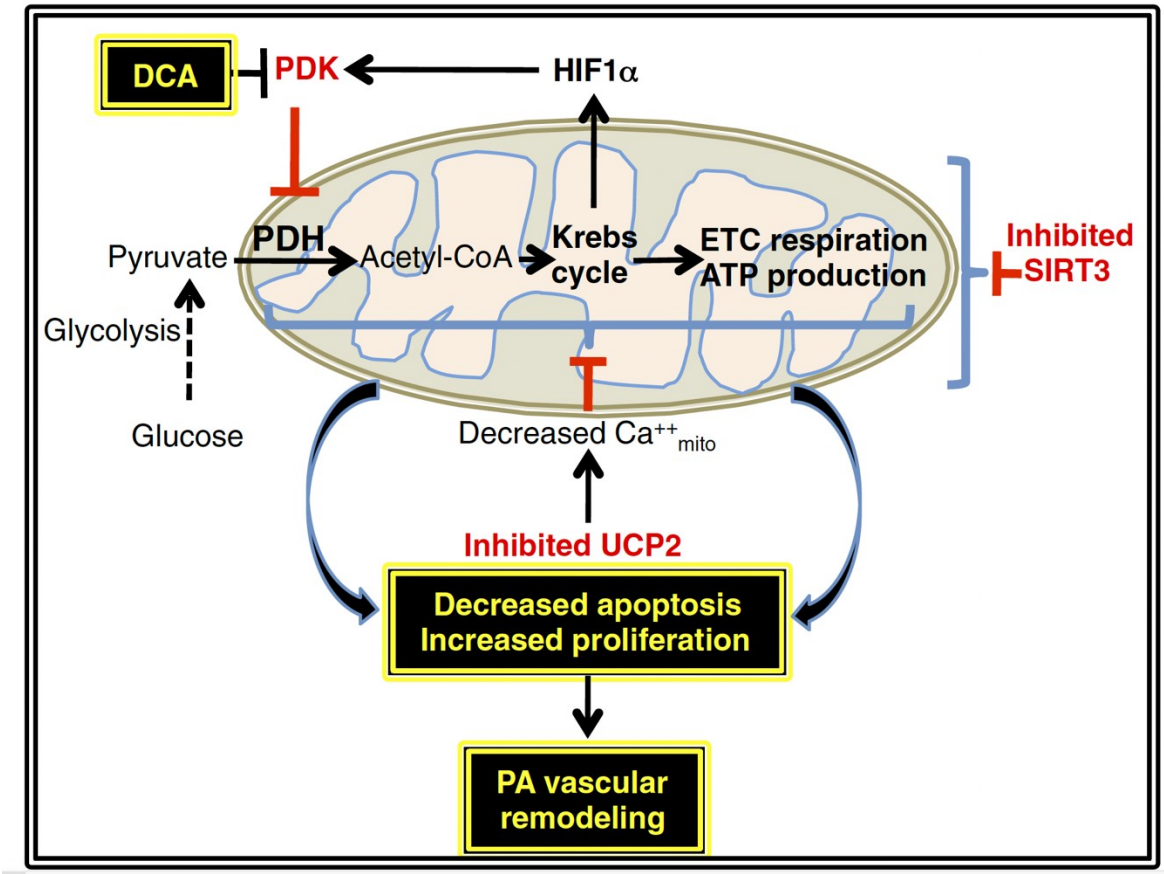

Figure 1. 1. The metabolic theory of PAH and how does dichloroacetate (DCA) works.

The schematic shows how loss of function of SIRT3 and UCP2 suppress mitochondrial function independently. In pulmonary arterial smooth muscle cells (PASMCs) of PAH, the glucose oxidation is inhibited while the glycolysis is activated, which decrease mitochondrial ROS production, and activate HIF-1α. HIF-1α activates PDK which phosphorylates and deactivates PDH. Therefore, this loop contributes to mitochondrial suppression. This mitochondrial suppression inhibits apoptosis and promotes proliferation, leading to the proliferative vascular remodeling in PAH. Dichloroacetate (DCA) is a selective PDK inhibitor which inhibits the PDK-driven mitochondrial suppression. However, it doesn't work properly when there is loss of function of UCP2 or SIRT3 as SIRT3 and UCP2 affect mitochondrial function in a PDK-independent manner. SIRT3 is a mitochondrial deacetylate (affect multiple enzymes in Krebs Cycle) and UCP2 is an atypical uncoupling protein enabling mitochondrial calcium entry (affect mitochondrial Ca^{++}-dependent enzymes, i.e. PDH).

1.1.3. Limitations of current rodent models for pulmonary hypertension (PHT): While mice are critical for the molecular studies of most diseases, because of the relative ease to create transgenic animals. Their contribution to PAH studies has been limited, at least compared to rats. Typically, there are few transgenic or KO mice that have been shown to develop spontaneous PAH. They do so in a limited way: the PA pressures typically are mildly or at most moderately elevated and the vascular remodeling and RV dysfunction is limited[23,24]. There has been no mouse model shown to develop spontaneous severe PAH associate with extensive vascular remodeling including plexogenic lesions[24]. The inflammatory involvement in such models is also limited and none shows the metabolic features throughout the body, with the exception of the Sirt3 or Ucp2 KO mice[20,21]. These 2 mouse types however, exhibit only mild PAH, similar to the mice exposed to chronic hypoxia, without significant vascular remodeling (no plexogenic lesions)[20,21]. The only model that reliably exhibits plexogenic lesions and severe PAH with high mortality, is the rat receiving Sugen (a VEGF inhibitor) plus hypoxia, although the plexogenic lesions appear only at the late stages of PAH[25]. Another weakness of that model is that a non-physiologic drug has to be used, confounding the interpretation of the data, particularly on the role of endothelial cells.

1.1.4. SNP of SIRT3 or UCP2: We recognized that central to pathogenesis of PAH is mitochondrial dysfunction due to an inhibition of the glucose oxidation gatekeeping enzyme PDH. Therefore, in our recently published study, we conducted a small clinical trial to test the response of PAH patients to Dichloroacetate (DCA), a drug that has been shown to reactivate mitochondrial suppression by inhibiting Pyruvate Dehydrogenase kinase (PDK, a mitochondrial enzyme that inhibits PDH), showing potential beneficial effects[22]. To study the subgroup of patients that did not respond to DCA, we performed genotyping. We found that several patients had loss of function

SNPs in Sirt3 (rs11246020) and Ucp2 (rs659366) in one or both alleles and in fact some patients carried both SNPs in either one or both alleles. Clinically, the presence of these relatively common SNPs has been associated with the metabolic syndrome and type 2 diabetes in humans[25-28], i.e. conditions in which a generalized metabolic abnormality is present throughout the body. The Sirt3 SNP affects the catalytic domain of the SIRT3 protein, inhibiting its activity by up to 34%, whereas the Ucp2 SNP affects the promoter of the gene, resulting in decreased Ucp2 mRNA levels[28,29]. Either way, the patients that carry these SNPs, which are not in linkage disequilibrium, would have abnormal mitochondrial function and maybe predisposed to more severe PAH, particularly when both SNPs are present. we hypothesized that these two Sirt3 and Ucp2 SNPs may be prevalent in patients with PAH and may be correlated with the severity of disease, the presence of type 2 diabetes and perhaps the outcomes of the disease. Second, to mechanistically explore this hypothesis, we generated mice that lack both Sirt3 and Ucp2 and hypothesized that they may develop severe PHT and perhaps recapitulate more features of human PAH than other commonly used rodent PHT models. We specifically aimed to determine whether they would develop spontaneous and severe PHT at a young age (without the use of external triggers like hypoxia or Sugen), as well as inflammatory plexogenic lesions.

1.2. Right Ventricle

1.2.1. Critical differences between the RV and the left ventricle (LV): The RV has a different embryologic origin, metabolism, vascularity and response to pressure overload than the LV which can remain hypertrophied (LVH) in a compensated state for decades in systemic hypertension[30,31]. In contrast, in PAH, the compensated RV hypertrophy (RVH) stage (cRVH) is much shorter, with

decompensation occurring often in months[32]. Thus, we cannot extrapolate knowledge from the LV to the RV. Despite the difficulty of the RV to adapt to disease states, it has a remarkable ability to adapt to physiologic changes. For example, in utero, due to the physiology of the fetal circulation, the afterload of the RV is high and as a result the RV at the time of birth is hypertrophied. With the first breath at birth and the transition to the adult circulation (characterized by a low-pressure pulmonary circulation) the RV afterload decreases and within a few weeks the RV remodels to the thin-walled, non-hypertrophied adult RV. However, in some patients that the transition to the adult circulation does not occur at birth (e.g. patients with pulmonary stenosis resulting in Eisenmenger's syndrome), the fetal RV does not regress to an adult RV phenotype and remains hypertrophied [30,31]. These patients live with very high pulmonary artery pressure and can survive for many decades[33]. The explanation for this intriguing clinical observation is lacking. It has been proposed that the persistence of the "fetal heart gene program" in these patients is the underlying mechanism[33]. This is unlikely to be the only or the most important factor. There is recent evidence showing that in a model of *acquired* adult RV hypertrophy, i.e. the PA banding model (PAB), the RV is much more resistant to failure compared to the RVs from other PAH models (like Monocrotaline induced PAH, MCT-PAH)[34]. In addition, within the group of patients with PAH, there is variability on survival and the duration of cRVH varies: patients with scleroderma-PAH have worse prognosis than patients with other idiopathic PAH (iPAH). A big difference between MCT-PAH and PAB-PHT and between Scleroderma and iPAH patients is much more systemic inflammation in the former. There is a critical need to identify the factors that regulate the transition from cRVH to a dRVH, in order to develop much need therapies and biomarkers. Recently it has become apparent that there are 2 characteristics of PAH that affect the whole body: a) an overall metabolic switch that has features of the metabolic remodeling in cancer and in

patients with insulin resistance[35,36] and b) a strong inflammatory environment with high levels of inflammatory cytokines in the blood[37-39], both independent predictors of morbidity and mortality[40]. It appears that the pulmonary circulation is much more sensitive to these metabolic and inflammatory signals compared to systemic arteries, explaining perhaps why in PAH the pulmonary arteries are affected far more than the systemic vessels[40]. The same could be true in the RV.

1.2.2. Transition from normal to compensated RV hypertrophy (cRVH) to decompensated RV hypertrophy (dRVH): In both animal and human PAH, the RV hypertrophy (cRVH: compensated RV hypertrophy) is one of the most common features in early stage. Then the RV hypertrophy will become RV dilation and failure (dRVH: decompensated RV hypertrophy) quickly. Therefore, the cRVH has increased RV free wall thickness but not severally increased RV end-diastolic diameter (RVEDD), increased mPAP and RV systolic pressures (RVSP) but preserved cardiac output compared to normal RV. In contrast, compared to cRVH, dRVH is characterized by a still high mean PA pressure but a drop in RVSP and cardiac output, as well as a further increase in right atrial (RA) pressure and RVEDD.

During the three stages of RV, a metabolic shift has been described. Compared to the mitochondria-driven glucose oxidation phenotype in normal RV, cRVH shows a glycolytic phenotype with a promotion of HIF1α activation and angiogenesis[41,42]. From cRVH to dRVH, the metabolic shift seems to be opposite from normal RV to cRVH. In dRVH, an increased mitochondrial reactive oxygen species (mROS) results in a suppression of HIF1α, reversing the glycolytic phenotype, and suppressing angiogenesis in the hypertrophied myocardium,

contributing to ischemia and RV failure[43]. Mitochondrial enzymes PDK and PDH are also involved in this metabolic remodeling[42,43]. This metabolic shift may not only affect cardiomyocytes but also cardiac fibroblasts which could differentiate to myofibroblasts in response to injury or stress (i.e. myocardial infarction, diabetes, etc)[44,45].

1.3. Two remaining mysteries of PAH

1.3.1. The mechanism of plexogenic lesions: At this point, the plexogenic lesion is described as an anarchic proliferation of cells in the PA vascular wall, including smooth muscle cells, endothelial cells and fibroblasts. This is because pathologists do traditional staining on these lesions in human samples and observe expression of von Willebrand factor (vWF), a-SMA and Vimentin. They conclude that this means that all three cell types proliferate independently. The work in this thesis challenges this interpretation as described in the Conclusion section (Chapter four), proposes that a change of cell identity may actually be taking place with all vascular cell types transforming to myofibroblasts, a cell type that expresses all these markers. If proven correct, our work suggests a major change in the therapeutic targeting for PAH, changing from anti-proliferative approaches to those that target cell identity regulation, including metabolic and epigenetic therapies.

A major impediment in our understanding of the plexogenic lesions is the lack of animal models. All the existing therapies of PAH have been developed on animal models that exhibit of increased vascular proliferation but no plexogenic lesions. The only animal model exhibiting plexogenic lesions is the old rat exposed to hypoxia and the VGEF inhibitor Sugen. But human PAH happens

in relatively younger patients, who are not hypoxic and are not exposed to Sugen. These deficiencies in the field explain why the current PAH therapies do not improve survival and do not reverse disease. It is easy to explain why simple vasal dilators like PDE5 inhibitors cannot reverse structural vascular remodeling in PAH, but other PAH therapies like endothelin antagonists and particular prostacyclin analogs like epoprostenol, which do have anti-proliferative effect, also fail to reverse PAH and prolong survival. For example, the most powerful and most expensive of the PAH therapies epoprostenol, was recently shown to have no effects on plexogenic lesions in patients treated for years, compared to other therapies (these patients provided tissues at the time of transplantation)[46,47].

1.3.2. The mechanism of transition from cRVH to dRVH: Another mystery is what drives the transition from cRVH to dRVH in PAH. The main driver of mortality and morbidity in PAH is the function of the RV rather than the degree of rise in mean Pulmonary Artery Pressure (mPAP)[1,40]. The RV has a much shorter compensated state compared to LV due to different embryologic origin, metabolism, vascularity and response to pressure overload[30,31,32]. Thus, the knowledge of the transition from LV hypertrophy to LV failure would not be applicable to the RV. Also, between 2 patients with the same age/sex and PA pressures, one may have a much shorter cRVH stage and decompensate much faster than other. Knowing what drives the transition of cRVH to dRVH will have a significant clinical impact because when a patient develops decompensated RV failure, it may be too late to even referred to transplant, because the patient may die in less than a year while typically patients wait for several years in transplant list. Therefore, understanding the mechanism that drives RV decompensation is very important, not only because it will provide a therapeutic target for RV remodeling (right now there is no RV-targeted treatment), but we may also find a

relevant biomarker to identify the patients that will be at risk of failing the RV quickly. In this case, patients with this biomarker could be considered for an early combination therapy and/or early referral to transplant.

In summary, my thesis addresses two critical questions in the PAH field that are currently not answered.

Chapter two: SNPs for genes encoding the mitochondrial proteins sirtuin3 and uncoupling protein 2 are associated with disease severity, type 2 diabetes, and outcomes in patients with pulmonary arterial hypertension and this is recapitulated in a new mouse model lacking both genes.

SNPs for genes encoding the mitochondrial proteins sirtuin3 and uncoupling protein 2 are associated with disease severity, type 2 diabetes, and outcomes in patients with pulmonary arterial hypertension and this is recapitulated in a new mouse model lacking both genes

Yongneng Zhang, Sotirios D. Zervopoulos, Aristeidis E. Boukouris, Maria Areli Lorenzana-Carrillo, Bruno Saleme, Linda Webster, Yongsheng Liu, Alois Haromy, Seyed Amirhossein Tabatabaei Dakhili, John R. Ussher, Gopinath Sutendra, Evangelos D. Michelakis

Affiliations

Department of Medicine (Cardiology), Faculty of Medicine and Dentistry (Y.Z., S.D.Z., A.E.B., M.A.L., B.S., L.W., Y.L., A.H., G.S., E.D.M.) and Faculty of Pharmacy and Pharmaceutical Sciences (S.A.T.D., J.R.U.), University of Alberta, Edmonton, Alberta, Canada.

A version of this chapter has been published as: Zhang Y, Zervopoulos SD, Boukouris AE, Lorenzana-Carrillo MA, Saleme B, Webster L, Liu Y, Haromy A, Tabatabaei Dakhili SA, Ussher JR, Sutendra G, Michelakis ED. SNPs for Genes Encoding the Mitochondrial Proteins Sirtuin3 and Uncoupling Protein 2 Are Associated With Disease Severity, Type 2 Diabetes, and Outcomes in Patients With Pulmonary Arterial Hypertension and This Is Recapitulated in a New Mouse Model Lacking Both Genes. J Am Heart Assoc 10, e020451 (2021).

2.1. Abstract

Background: Isolated loss-of function single nucleotide polymorphisms (SNPs) for *SIRT3* (a mitochondrial deacetylase) and *UCP2* (an atypical uncoupling protein enabling mitochondrial calcium entry) have been associated with both pulmonary arterial hypertension (PAH) and insulin resistance, but their collective role in animal models and patients is unknown.

Methods and Results: In a prospective cohort of PAH patients (n=60) we measured SNPs for both *SIRT3* and *UCP2,* along with several clinical features (including invasive hemodynamic data) and outcomes. We found *SIRT3* and *UCP2* SNPs often both in the same patient in a homozygous or heterozygous manner, correlated positively with PAH severity and associated with the presence of type II diabetes and 10-year outcomes (death, transplantation). To explore this mechanistically, we generated double knockout (KO) mice for Sirt3 and Ucp2 and found increasing severity of PAH (mean pulmonary artery pressure, right ventricular hypertrophy/dilatation and extensive vascular remodeling, including inflammatory plexogenic lesions), in a gene dose-dependent manner), along with insulin resistance, compared to wild-type (WT) mice. The suppressed mitochondrial function (decreased respiration, increased mitochondrial membrane potential) in the double KO pulmonary artery smooth muscle cells was associated with apoptosis-resistance and increased proliferation, compared to WT mice.

Conclusions: Our work supports the metabolic theory of PAH and shows that these mice exhibit spontaneous severe PAH (without environmental or chemical triggers) that mimics human PAH and may explain the findings in our patient cohort. Our study offers a new mouse model of PAH, with several features of human disease that are typically absent in other PAH mouse models.

KEYWORDS: Mitochondria, Vascular Disease, Pulmonary Arterial Hypertension, Vascular Remodeling, Vascular Smooth Muscle Cells, Plexogenic Arteriopathy, Insulin Resistance

Clinical Perspective

What Is New?

- We found a provocative correlation between the loss-of-function SNPs of sirtuin3 and uncoupling protein 2 (both encode mitochondrial proteins) with the severity of disease in patients with pulmonary arterial hypertension (PAH), as well as an association with the presence of type 2 diabetes (a previously described feature of patients with PAH that remains unexplained) and outcomes (death or transplantation).
- We also created a novel mouse model (sirtuin3 and uncoupling protein 2 double-knockout) of PAH in which to explore our clinical data, and we found that it has more features of human PAH than any previously described rodent model of PAH.
- This is the first mouse model of PAH with spontaneous and extensive plexogenic lesions (the *sine qua non* of human PAH).

What Are the Clinical Implications?

- Our mouse model supports our provocative clinical data in our cohort and is directly relevant to a subgroup of patients with PAH carrying more than 1 loss-of-function SNPs in genes encoding mitochondrial proteins, particularly for those patients who carry them in both alleles.
- These are relatively common SNPs in the general population and thus they could be further explored as potential biomarkers in Precision Medicine studies.
- Also, since mouse models of PAH have been criticized for the lack of important clinical features of human PAH (including the mild increase in pulmonary artery pressures and the lack of plexogenic lesions), our new mouse PAH model is important for the translational

research field of PAH, strengthening the role of genetic mouse models for mechanistic studies.

2.2. Introduction

Pulmonary Arterial Hypertension (PAH) is characterized by pulmonary arterial remodeling that results in lumen obliteration, raising the pulmonary vascular resistance (PVR). While initially this leads to right ventricular (RV) hypertrophy, it then advances to RV dilatation and death from RV failure[1,32]. The vascular wall cells in the remodeled pulmonary arteries are characterized by activation of many transcription factors (e.g. NFATc2; nuclear factor of activated T-cells c2, HIF1α; Hypoxia Inducible Factor 1α, etc.) that promote proliferation; and by a multifactorial suppression of mitochondrial function that promotes apoptosis-resistance in a cancer-like manner[1]. Our proposed metabolic theory of PAH suggests that such a mitochondrial suppression is a critical and early event that has the potential to also activate many of the transcription factors implicated in PAH[2,16,48]. It could also promote the inflammation that has recently been shown to play a central role in the disease (e.g. the remodeled pulmonary arteries are surrounded by many activated inflammatory cells)[2,48,49]. Inhibition of mitochondrial oxidative phosphorylation (glucose oxidation) is an early and necessary event in T cell activation[50]. There is also evidence that patients with PAH have features of the metabolic syndrome and insulin resistance (without necessarily being obese)[36]. In fact, in skeletal muscle biopsies in PAH patients, there is evidence of mitochondrial dysfunction (downregulation of mitochondrial enzymes and upregulation of glycolytic enzymes)[51]. In animals with PAH, decreased respiration in skeletal muscle was shown to be present early in the development of PAH[52]. This suggests that a systemic metabolic disturbance may affect the whole body in a PAH patient, although the vascular pathology is specific to the pulmonary arteries (compared to systemic vessels). This is why knocking out mitochondrial proteins in the whole animal (as opposed to cell or tissue-specific KO) is clinically relevant.

Indeed, KO mice lacking either sirtuin3 (*Sirt3*)[20] (a major mitochondrial deacetylase) or uncoupling protein 2 (*Ucp2*)[21,53] (an atypical uncoupling protein that mostly facilitates calcium entry into the mitochondria) developed spontaneous pulmonary hypertension (PHT) and vascular remodeling. However, as is commonly the case with mice PHT models, the increase in PA pressure was mild and the mice did not develop plexogenic lesions, perhaps the most typical pathology finding in human PAH (anarchic proliferation of diverse vascular and inflammatory cells causing near-complete obliteration of the vascular lumen)[54]. In fact, the only model that reliably exhibits plexiform lesions and severe PAH with high mortality, is the rat in response to Sugen (a VEGF inhibitor) plus hypoxia, although the plexiform lesions appear only at the late stages of the disease[25]. A potential limitation of that model is that a non-physiologic drug has to be used, confounding the interpretation of the data, particularly on the role of endothelial cells. Currently, there is no mouse model that develops predictably and commonly plexogenic lesions.

Loss of *Sirt3* or *Ucp2* expression or function leads to hyperacetylation of mitochondrial proteins and enzymes (inhibiting their function[20,29]) and decreased intramitochondrial calcium[55] (inhibiting the function of Ca^{++}-dependent enzymes like Pyruvate Dehydrogenase (PDH), the gatekeeping enzyme in glucose oxidation[21]) respectively. This results in mitochondrial hyperpolarization and decreased production of diffusible mitochondrial reactive oxygen species (mROS, like H_2O_2) causing apoptosis-resistance[2,16,48] (mechanism can be found in Chapter I Introduction at 1.1.2.3. Metabolic Theory). Along with the decreased production of diffusible metabolites (like α-ketoglutarate) in pulmonary vascular cells, these redox changes promote activation and nuclear translocation of pro-proliferative transcription factors, like HIF1α (even in the absence of hypoxia) or NFATc2, which have been implicated in the pathogenesis of PAH[2,16,48].

We recently conducted a small clinical trial to test the response of PAH patients to a metabolic modulator, showing potential beneficial effects[22]. To study the subgroup of patients that did not respond to Dichloroacetate, a drug that has been shown to reactivate mitochondrial suppression by inhibiting Pyruvate Dehydrogenase kinase (PDK, a mitochondrial enzyme that inhibits PDH), we performed genotyping. We found that several patients had loss of function single nucleotide polymorphisms (SNPs) in *SIRT3* (rs11246020) and *UCP2* (rs659366) in one or both alleles and in fact some patients carried both SNPs in either one or both alleles[22]. Clinically, the presence of these relatively common SNPs has been associated with the metabolic syndrome and type 2 diabetes in humans[26-29,56], i.e. conditions in which a generalized metabolic abnormality is present throughout the body. The *SIRT3* SNP affects the catalytic domain of the SIRT3 protein, inhibiting its activity by up to 34%, whereas the *UCP2* SNP affects the promoter of the gene, resulting in decreased *UCP2* mRNA levels[28,29]. Either way, the patients that carry these SNPs, which are not in linkage disequilibrium, would have abnormal mitochondrial function and maybe predisposed to more severe PAH, particularly when both SNPs are present.

First, we hypothesized that these two *SIRT3* and *UCP2* SNPs may be prevalent in patients with PAH and may be correlated with the severity of disease, the presence of type 2 diabetes and perhaps the outcomes of the disease. Second, to mechanistically explore this hypothesis, we generated mice that lack both *Sirt3* and *Ucp2* and hypothesized that they may develop severe PHT and perhaps recapitulate more features of human PAH than other commonly used rodent PHT models. We specifically aimed to determine whether they would develop spontaneous and severe PHT at a young age (without the use of external triggers like hypoxia or Sugen), as well as inflammatory plexogenic lesions.

2.3. Methods

Our work with human clinical data and human blood as well as our work with mice, was performed with permission from the University of Alberta Human Research Ethics Board (HREB) and Animal Care and Use Committee (ACUC), respectively.

SNP genotyping assay: Genomic DNA was extracted from buffy coat using FlexiGene DNA Kit (QIAGEN) following manufacturer's instruction. DNA samples were quantified with a Nanodrop Spectrophotometer (ND-8000) and normalized to a concentration of 6.5 ng/μL. Samples (50ng per each) were genotyped by TaqMan® SNP Genotyping Assays for rs11246020 (*SIRT3*) and rs659366 (*UCP2*), and processed and read on the Droplet Digital PCR QX200 (Bio-Rad) according to the manufacturer's protocol. Each sample was partitioned into 20,000 discrete droplets and after amplification, each droplet was analyzed individually using a two-color detection system (FAM and VIC). Amplifications were carried out as follows: at 94 °C for 10 min, followed by 40 cycles at 94 °C (30 sec), 60 °C (1 min, ramp rate: 2-3°C per second); followed by holding at 98 °C (10 min), and holding at 4 °C.

***Sirt3* and *Ucp2* Mutant Genotyping**; Mice were genotyped by PCR using genomic DNA isolated from ear notching biopsies as described by Jackson Laboratories. *Sirt3* mutant mice have deletion of exons 2-3 which abolishes gene function. A combination of two forward primers (one for mutant, sequence: TAC TGA ATA TCA GTG GGA ACG and one for wild type, sequence: CTT CTG CGG CTC TAT ACA CAG) along with one common reverse primer (sequence: TGC AAC AAG GCT TTA TCT TCC) was used to detect the wild type allele (562bp) and the mutant allele (200bp, deletion of exons 2-3 result in a smaller fragment). The *Sirt3* heterozygous mice are positive for both alleles (wild type; 562bp and mutant; 200bp). The targeted *Ucp2* mutant mice have an insertion of a PGK-NEO cassette replacing exons 3-7 to create the larger mutant allele. Two sets

of primers are used in combination to identify wildtype (forward primer sequence: GCG TTC TGG GTA CCA TCC TA, reverse primer sequence: GCT CTG AGC CCT TGG TGT AG) and mutant mice (forward primer sequence: CTT GGG TGG AGA GGC TAT TC, reverse primer sequence: AGG TGA GAT GAC AGG AGA TC). The mutant allele (that expresses the larger PGK-NEO cassette) is expressed at 280bp, while the wild type allele (which does not express the PGK-NEO cassette) is expressed at a lower 156bp. The *Ucp2* heterozygous mice are positive for both alleles (mutant; 280bp and wild type; 156bp). PCRs were carried out on a MasterCycler PCR Thermal Cycler (Eppendorf Cat # 5345) by direct amplification of the DNA from ear notching biopsies with the use of Phire Tissue Direct PCR Master Mix (ThermoFisher Scientific Cat # F170) following manufacturer's protocol. Amplifications were carried out as follows: at 94 °C for 5 min, followed by 10 cycles at 94 °C (20 sec), 65 °C (15 sec,-0.5°C per cycle decrease), 68 °C (10 sec); followed by 32 cycles at 98 °C (15 sec), 60 °C (15 sec), 72 °C (10 sec); finishing at 72 °C (2 min) and holding at 4 °C.

RNA isolation and qRT-PCR: mRNA was isolated using Qiazol (Qiagen). mRNA isolated from lung were added to a microwell plate with TaqMan probes and reagents. Quantitative RT-PCR was performed using TaqMan RNA-to-CT 1-Step Kit (Applied Biosystems 4392938), and 18S was used as a housekeeping gene. Primers were purchased from Thermo Fisher Scientific (*Sirt3* Mm01275637_g1, *Ucp2* Mm00627599_m1).

Cell Culture: Pulmonary artery smooth muscle cells (PASMCs) from WT*, Sirt3*$^{-/-}$*-Ucp2*$^{+/-}$*,Sirt3*$^{+/-}$*-Ucp2*$^{-/-}$ and *Sirt3*$^{-/-}$*-Ucp2*$^{-/-}$ mice were freshly isolated from intra-pulmonary arteries (>4th division), with an enzymatic cocktail containing papain (1mg/ml) (Sigma Aldrich), dithiothreitol (DTT; 0.5mg/ml) (Sigma Aldrich), collagenase I (0.8 mg/ml) (Worthington), and bovine serum albumin (0.8 mg/ml) (Sigma-Aldrich). PASMCs were cultured in Dulbecco's Modified Eagle's

Medium (DMEM, Gibco) with 10% fetal bovine serum (FBS) (Sigma-Aldrich) and 1% penicillin/streptomycin (Gibco) at 9% CO_2. Passages 2–4 PASMCs were used for all experiments.

Mitochondrial respiration measurements: Oxygen consumption rates (OCR) and extracellular acidification rates (ECAR) were assessed using a Seahorse XF24 Extracellular Flux Analyzer (Agilent, Santa Clara, CA, USA) according to the manufacturer's instructions. PASMCs were seeded and cultured overnight in Seahorse XF-24 plates at a density of $4*10^4$ cells per well. The next day, plating medium was removed and replaced with bicarbonate-free Seahorse XF Base medium without phenol red (Agilent) supplemented with 25 mM glucose. Following incubation of the cells in the CO2-free incubator for 1 h, cells were placed in the Seahorse Analyzer. OCR and ECAR were calculated using 3 min mix and 3 min measure cycles. After the run, cells were washed with PBS and lysed in 100 µl per well of RIPA buffer (supplemented with protease inhibitors) for 30 min at 4℃ with constant agitation. Protein concentration was measured with a BCA assay and used to normalize the OCR and ECAR values.

Immunoblots: Tissues were collected and granulated on dry ice and lysed in ice-cold RIPA buffer via sonication with 10 quick pulses using a handheld homogenizer (VWR, PA, USA). Samples were then spun down at 10,000 rpm for 25 min in a tabletop centrifuge (Eppendorf AG, Hamburg, Germany). After centrifugation, the supernatant was collected. Protein concentration was quantified with a BCA kit (Thermo Fisher Scientific, Waltham, MA, USA) and measured on a SpectraMax iD3 plate reader (Molecular Devices, San Jose, CA, USA). Samples were then diluted to a final concentration of 1 µg / µl in RIPA buffer and 2x Laemmli Sample Buffer (Sigma-Aldrich). Finally, they were boiled at 95℃ for 5 min. All samples were loaded on SDS-PAGE polyacrylamide gels. Proteins were then transferred onto 0.45 nm pore nitrocellulose membranes using a Trans-blot Turbo transfer system (Bio Rad, Hercules, CA, USA) according to the

manufacturer's instructions. After transferring, membranes were incubated with Ponceau S (Thermo Fisher Scientific) to verify efficient transferring of the proteins. Membranes were then washed with TBST and blocked with 5% BSA in TBST for 1 h at room temperature. Membranes were then incubated with the primary antibody in 1% BSA in TBST overnight at 4 ℃ with gentle rotation. The following day, membranes were washed with TBST and incubated with the appropriate HRP-conjugated secondary antibodies (Cell Signaling Technology, Danvers, MA, USA). Proteins were detected after incubation of the membranes with ECL buffer (Thermo Fisher Scientific) and visualized on a ChemiDoc imaging system (Bio-Rad). Antibodies and dilutions: Sirt3 (Cell signaling technology, 5490) 1:1000, Ucp2 (Santa Cruz, sc-6525) 1:300, p-AKT (Ser473) (Cell signaling technology, 4060T) 1:1000, AKT (Cell signaling technology, 4691) 1:3000 and β-Actin (Santa Cruz sc81178) 1:2,000.

Confocal Imaging: Immunofluorescence staining was performed using a Zeiss LSM-710 model, equipped with an Airyscan module (Carl Zeiss). Cultured PASMC were grown on coverslips overnight. They were fixed with 2% PFA at 37℃ for 15 min, followed by permeabilization with Triton X-100 (0.25%) for 10 min. They were then treated with Image-iT FX Signal Enhancer (Thermo Fisher Scientific) for 30 min at room temperature and blocked for 1 h with 10% serum from the host of the secondary antibody. Cells were incubated with the primary antibodies overnight at 4℃. The following day, incubation with the secondary antibodies was performed for 1h at room temperature in the dark. Finally, they were counterstained with 1 μM DAPI (Molecular Probes, Oregon, USA) at room temperature for 10 min, prior to mounting in ProLong Glass (Thermo Fisher Scientific). Lung tissues were collected and prepared after injecting Optimal cutting temperature (OCT) through trachea to expand the lung, then embedded in OCT compound and stored in -80℃ freezer for frozen section. Tissue slices (5 μm thickness) from lung tissue were

processed and stained similar to cultured cells. Antibodies used were alpha smooth muscle actin (SMA) (Abcam, ab5694), von Willebrand Factor (vWF) (Abcam, ab11713), CD4 (Invitrogen, LS14004182), Ki67 (Abcam, ab16667), NFATc2 (Abcam, ab2722), HIF-1 alpha (Abcam, 51608) and ^{Y705}p-STAT3 (Cell signaling technology, 9131). All antibodies used for immunofluorescence were diluted in 1:100 and all secondary antibodies in 1:1000.

For measuring muscularization, vessels (<40μm) were classified as fully (100%), partially, or non-muscularized (0%), based on the percentage of vWF surrounded by SMA in each vessel.

Apoptosis was measured using the Apoptag Apoptosis Detection Kit for TUNEL (Invitrogen) and the Dead Cell Apoptosis Kit with Annexin V FITC and Propidium iodide (Invitrogen) according to the manufacturer's instructions. The mitochondrial membrane potential ($\Delta\Psi m$) was measured by staining live PASMCs with 20nM tetramethyl-rhodamine methyl-ester perchlorate (TMRM) (Invitrogen) and 500nM Hoechst 33342 (Invitrogen) for 30 minutes at 37°C. The mROS were measured by staining live PASMCs with 5μM MitoSOX (Invitrogen) and 500nM Hoechst 33342 in non-serum media for 15 minutes at 37°C, then cells were washed and replaced with regular media for imaging.

Images were quantified by measuring fluorescence intensity by using ZEN Microscopy Software (ZEN, ZEISS).

Echocardiography: Mice were anesthetized with isoflurane and maintained a heart rate of 350-450 beats per minutes and the Vevo 3100 High Resolution Imaging System (VisualSonics, Toronto, Canada) was used. Right ventricular thickness, right ventricular end-diastolic diameter and tricuspid annular plane systolic excursion (TAPSE) were recorded in the M-Mode. TAPSE was calculated by measuring the vertical movement of the tricuspid annulus between end-diastole and end-systole in the four chamber view, reflecting the longitudinal contraction of the RV.

Cardiac output (CO) was calculated after determining the pulmonary artery diameter (PAD), pulmonary artery velocity time integral (PAVTI), and heart rate (HR) using the formula: CO = 7.85 x PAD^2 x PAVTI x HR/10,000. Images with heart rate < 350 were excluded from the analysis.

Hemodynamic Measurements: Mice were placed in a supine position on a heated table under inhaled isoflurane anesthesia (3%–4% isoflurane initially and 2% isoflurane during process). A modified (curved) Millar catheter (microtip, 1.4F, Millar Instruments) was advanced through the jugular vein in closed-chest animals into right atrium (RA), RV and PA. RA pressure, RV pressure and PA pressure tracings were recorded continuously and mPAP was calculated (Power Lab, with Chart software 5.4, ADInstruments). LVEDP was recorded by retrograde advancement of the catheter from the carotid artery into the left. Mice were euthanized after hemodynamic measurements.

Histology: Lung sections (5µm) from Frozen lung samples were stained using hematoxylin and eosin (H&E) stain for histology, and SMA and vWF (endothelial cell marker) for immunofluorescence. For measuring medial wall thickness, vessels >40µm and <300µm were identified and measured at the two ends of the shortest external diameter of the pulmonary arteries, and the average was taken [(2 x wall thickness / external diameter) x 100]. For measuring right ventricular fibrosis, Lung sections (5µm) from Frozen lung samples were stained using Masson's Trichrome Stain Kit following manufacturer's instruction. Fibrotic area was quantified by morphometric methodology (ImageJ).

In vivo Assessment of glucose homeostasis: Glucose and insulin tolerance tests were performed in mice fasted overnight or after a 6 h fast, following which IP glucose (2 g/kg) or insulin (0.5 U/kg) was administered. Blood glucose measurements were assessed via tail whole-blood at the end of the fast (0 min), followed by samples at 15, 30, 60, 90, and 120 min post-glucose or insulin

administration, using the Contour Next blood glucose monitoring system (Bayer). Plasma was also collected during the glucose tolerance test from tail whole-blood at the 0 and 15 min time points for the assessment of circulating insulin levels, using a commercially available enzyme-linked immunosorbent assay kit (Alpco Diagnostics) according to the manufacturer's instructions. In brief, 5 µL of each sample was added to each well with 75 µL of a provided enzyme conjugate, and the 96 well plate was then incubated for 2 h at room temperature on an orbital microplate shaker at ~700-900 RPM. After incubation, the plate was washed 6x with a provided working strength wash buffer, and then 100 µL of a provided substrate was added to each well to start the reaction, which was terminated after 30 min via addition of 100 µL of stop solution. Any air bubbles were removed and plasma insulin levels "ng/mL" were determined via reading the absorbance of the plate at a wavelength of 450 nm.

Statistical analysis: All statistical analyses performed on STATA (StataCorp LLC, Texas, USA). Values are expressed as mean ± SEM. The use of parametric or non-parametric tests was decided after assessment of normal distribution of the values by the Shapiro-Wilk normality test. For parametric tests, we used two-tailed, unpaired Student's t test to assess statistical significance between two groups, and multiple groups were compared using one-way analysis of variance (ANOVA) or two-way repeated measures ANOVA followed by a Bonferroni post hoc analysis. For non-parametric tests, Mann-Whitney U test was used for comparisons between two groups and Kruskal-Wallis test was used to compare multiple groups. Non-parametric correlation analysis of the clinical data was performed using the Spearman correlation co-efficient. Significance for all statistical testing was considered to be $p < 0.05$.

2.4. Results

To study the presence of *SIRT3* and *UCP2* SNPs, we used a small (n=60) but well-characterized prospective cohort of PAH patients that had agreed to participate in our clinical database and also offer blood for our biobank, at the time of their referral, over the past 10 years. These consisted of associated PAH (aPAH; mainly patients with autoimmune collagen vascular diseases like scleroderma or history of anorectic drugs use) and idiopathic PAH (iPAH). All patients underwent right heart catheterization, echocardiography, pulmonary function testing, V/Q scan and lung CT scans, as well as extensive bloodwork, so that all the potentially secondary causes of PHT were excluded and the patients could accurately be diagnosed with PAH. Patients were not included if they had a severe disease other than PAH, including cancer, evidence of significant systemic vascular disease, morbid obesity or renal failure. The hemodynamics shown in **Table 2.1** reflect the first catheterization, before the initiation of PAH therapies. All the patients were followed at least 3 times a year and all received a protocol-driven initiation of PAH therapies, which included: phosphodiesterase type 5 inhibitors as a first line of therapy; addition of an endothelin receptor antagonist if 3-4 months later the 6-minute walk test remained below 350 meters; and addition of a prostacyclin analogue if at any point the 6 minute walk dropped below 200 meters with clinical evidence of right ventricular failure resistant to diuretics. **Table 2. 1** also shows the therapies for each patient, at the last review of the 10-year database (i.e. June 2020). The common, protocol-driven therapeutic approach and the exclusion of significant co-morbidities at inclusion, allowed us to follow outcomes (death or lung transplantation) in our cohort. All the deaths shown in **Table 2. 1** were considered, to the best of our knowledge, to be a direct result of PAH worsening and right heart failure.

Digital PCR was utilized with primers for both the SNP variant and the wild-type (WT) versions of each of the *SIRT3* and *UCP2* genes. We used an SNP score method that we previously described[22], by which a score of 0 was given if both alleles were WT; a score of 1 if one of the SNPs was present in a heterozygous manner; a score of 2 if both SNPs were present in a heterozygous manner or one SNP was present in a homozygous manner; and a score of 3 if one SNP was present in a homozygous and the other was present in a heterozygous manner (**Table 2. 1; Figure 2. 1A**). **Table 2. 1** lists the SNP (i.e. gene variant) in both alleles for both *SIRT3* and *UCP2* genes. We found that the majority of patients had an SNP score of 1, many had a score of 2 and one patient had a score of 3 (**Table 2. 1**). A non-parametric correlation analysis using the Spearman coefficient revealed a weak but statistically significant positive correlation between the PVR (mean PAP-PAWP / CO) and the SNP score (**Figure 2. 1B**), meaning the increase of PVR is a dosage effect of gene alleles. We found that type 2 diabetes was more prevalent in patients with SNP score of 1 and 2-3 (attributable risk from the presence of the SNPs 58% and 75% respectively), and the same was true for death/transplantation (attributable risk 29% and 47%), compared to patients with an SNP score of 0 (**Table 2. 1; Figure 2.1B**). We realize the small size of our single center cohort does not allow us to conclude that there is either a true or a causal association with disease severity, type 2 diabetes or negative outcomes, but this was a motivation to explore this provocative association mechanistically with an animal model.

We generated a double knockout colony from a double heterozygous colony that was initially generated by crossing heterozygote $Sirt3^{+/-}$ mice (129/Sv background) with $Ucp2^{+/-}$ mice (C57BL6 background), both of which are commercially available and previously published by our group[20,21]. We then crossed double heterozygous mice to obtain a Mendelian mix of $Sirt3^{+/-}$-$Ucp2^{+/-}$, $Sirt3^{-/-}$-$Ucp2^{+/-}$, $Sirt3^{+/-}$-$Ucp2^{-/-}$ and $Sirt3^{-/-}$-$Ucp2^{-/-}$ mice. We crossed the double

heterozygous sub-colony for 10 generations before we established a stable new mixed background WT mouse (WT, *Sirt3*$^{+/+}$-*Ucp2*$^{+/+}$) and after that, we started crossing and studying littermate mice (**Figure 2. 2 A-C**). We chose this approach (rather than backcrossing toward one of the two backgrounds) because it better reflects the genetic variability of our PAH patients. *Sirt3*$^{-/-}$-*Ucp2*$^{-/-}$ mice were viable at birth (i.e. no embryonic lethality), and they also fit the predicted Mendelian ratio, suggesting that double loss of *Sirt3* and *Ucp2* is not required for embryogenesis.

By the 3-4th month of age, both male and female mice showed clinical evidence of disease (i.e. decreased activity, agitation, decreased feeding). Echocardiography and closed-chest right heart catheterization (via the jugular vein) at 3-4 months-old mice revealed PHT with elevated systolic and mean arterial pressures, increased right atrial pressure, decreased cardiac output, RV hypertrophy and RV dilatation (both by ECHO and at euthanasia) and decreased systolic RV function (by TAPSE in echocardiography) (**Figure 2. 3 A-B**). Absence of any increase in LVEDP (**Figure 2. 4**) and macroscopic/histology evidence of lung parenchymal abnormalities, suggested that this was PAH. Importantly and as hypothesized, there was a dose-response between the degree of gene loss and the severity of PAH, as the worse PAH was found in *Sirt3*$^{-/-}$-*Ucp2*$^{-/-}$ mice, less in the *Sirt3*$^{-/-}$-*Ucp2*$^{+/-}$ *or Sirt3*$^{+/-}$-*Ucp2*$^{-/-}$ mice and less in the *Sirt3*$^{+/-}$-*Ucp2*$^{+/-}$ mice, while all showed higher pressures than the WT mice (**Figure 2. 3 A**). Even at this young age of 3-4 months, the mice had clear right ventricular hypertrophy (RVH), and decreased systolic RV function and RV dilatation was mostly present at the *Sirt3*$^{-/-}$-*Ucp2*$^{+/-}$ *or Sirt3*$^{+/-}$-*Ucp2*$^{-/-}$ and the *Sirt3*$^{-/-}$-*Ucp2*$^{-/-}$mice (**Figure 2. 3 A**). We also performed the Masson's trichrome staining to the right ventricles to measure fibrosis. These data showed that *Sirt3*$^{-/-}$-*Ucp2*$^{+/-}$ (three allele-KO), and *Sirt3*$^{-/-}$-*Ucp2*$^{-/-}$ (double KO) mice have a significant increase of fibrosis, compared to wild-type controls (Figure III Data Supplement). Moreover, the mortality (as assessed by Kaplan Meier survival curve) was

significantly increased in the *Sirt3*$^{-/-}$-*Ucp2*$^{-/-}$ mice, compared to wild type (Figure IV Data Supplement). Although most of the mice studied were male, at least 2 female mice were included in each of the groups shown in **Figure 2.3 A**. No difference was detected between male and female mice and the data were expressed as one group for each study.

Lung histology showed the presence of extensive vascular remodeling, with the worse shown in *Sirt3*$^{-/-}$-*Ucp2*$^{-/-}$ and *Sirt3*$^{-/-}$-*Ucp2*$^{+/-}$ *or Sirt3*$^{+/-}$-*Ucp2*$^{-/-}$, in keeping with the hemodynamic data. There was an increase in % medial thickness in medium sized pulmonary arteries (40-100μm) (**Figure 2. 5 A**) and increased muscularization of the small sized vessels (<40μm), shown in both H&E staining and confocal microscopy immunohistochemistry, using SMA to mark smooth muscle cells and vWF to mark the endothelium (**Figure 2. 5 B**). More importantly, there were extensive plexogenic lesions in the pulmonary vessels of the *Sirt3*$^{-/-}$-*Ucp2*$^{-/-}$ and *Sirt3*$^{-/-}$-*Ucp2*$^{+/-}$ *or Sirt3*$^{+/-}$-*Ucp2*$^{-/-}$mice (**Figure 2.6**). The remodeled pulmonary arterioles also had increased levels of the proliferation marker Ki67 (**Figure 2. 7**). Futhermore, the fibrosis in the right ventricle is increased from WT to *Sirt3*$^{-/-}$-*Ucp2*$^{+/-}$ to *Sirt3*$^{-/-}$-*Ucp2*$^{-/-}$ (**Figure 2. 8**). The Sirt3 and Ucp2 double knockout mice showed a significant decreased survival compared with wildtype (**Figure 2. 9**).

An unanswered question in the PAH field is the mechanism of the plexogenic arteriopathy and particularly whether this is downstream or upstream to the increase in pressure. Performing closed-chest right heart catheterization in young mice is challenging and very difficult in mice of 2 months of age. We managed to perform reliable catheterization in three 2-month old mice/group and we found that the *Sirt3*$^{-/-}$-*Ucp2*$^{-/-}$ mice had established plexogenic arteriopathy despite the fact that the PA pressure (at least at rest) was within normal levels and similar to the WT mice (**Figure 2. 10**).

We then tested whether there was increased presence of inflammatory cells within and around the remodeled pulmonary vessels by staining the lungs with a marker of Treg cells (CD4), which have been directly implicated in the pathogenesis of PAH, although whether they promote injury or they participate in the healing response, remains unclear[57,58]. Similar to the vascular remodeling degree, the *Sirt3*$^{-/-}$-*Ucp2*$^{-/-}$ and *Sirt3*$^{-/-}$-*Ucp2*$^{+/-}$ *or Sirt3*$^{+/-}$-*Ucp2*$^{-/-}$ mice exhibited a large pulmonary vascular infiltration with CD4^{+} T cells, compared to lungs from WT mice (**Figure 2.11**).

We then isolated and cultured PASMCs from the intrapulmonary pulmonary arteries of these mice (>4th division) and we showed that even in *in vitro* conditions they maintained their proliferative phenotype, with the *Sirt3*$^{-/-}$-*Ucp2*$^{-/-}$ and *Sirt3*$^{-/-}$-*Ucp2*$^{+/-}$ *or Sirt3*$^{+/-}$-*Ucp2*$^{-/-}$ PASMCs expressing more Ki67, higher nuclear levels of the pro-proliferative master transcription factors HIF1α and NFATc2 and a higher ratio of nuclear/cytoplasmic of ^{Y705}p-STAT3, than PASMCs from the WT mice (**Figure 2.12 and 2. 13A**). Under serum starvation (0.1%), the *Sirt3*$^{-/-}$-*Ucp2*$^{-/-}$ and *Sirt3*$^{-/-}$-*Ucp2*$^{+/-}$ *or Sirt3*$^{+/-}$-*Ucp2*$^{-/-}$ PASMCs exhibited less apoptosis compared with the WT cells, measured with the TUNEL and Annexin V assays (**Figure 2. 13B and 2. 14**). We have previously shown that proliferative PASMCs from PAH animals had more hyperpolarized mitochondria (measured by TMRM) and produced less mROS (measured by MitoSox)[20,21,59,60]. This was confirmed in these cells as well, with the *Sirt3*$^{-/-}$-*Ucp2*$^{-/-}$and *Sirt3*$^{-/-}$-*Ucp2*$^{+/-}$ *or Sirt3*$^{+/-}$-*Ucp2*$^{-/-}$ PASMCs exhibiting higher ΔΨm (higher TMRM fluorescence) and lower levels of mROS (lower MitoSox fluorescence) (**Figure 2. 15A**). The increased mitochondrial potential contributes to the suppression of mitochondria-dependent apoptosis and is consistent with a suppression of mitochondrial function, as we have previously shown in both PAH PASMCs and cancer cells[5,22,61]. Thus, we measured respiration and glycolytic rates in PASMCs. As expected, we found that *Sirt3*$^{-}$

$^{/-}$-*Ucp2*$^{-/-}$and *Sirt3*$^{-/-}$-*Ucp2*$^{+/-}$ *or Sirt3*$^{+/-}$-*Ucp2*$^{-/-}$ PASMCs had lower respiration rates and higher glycolytic rates compared to WT PASMCs, using the SEAHORSE platform (**Figure 2. 15B**).

Last, we assessed for signs of insulin resistance in *Sirt3*$^{-/-}$-*Ucp2*$^{-/-}$mice, which demonstrated marked elevations in blood glucose levels in response to a glucose tolerance test, compared to WT mice (**Figure 2. 16A**)[62]. The glucose intolerance in *Sirt3*$^{-/-}$-*Ucp2*$^{-/-}$mice was associated with no change in circulating insulin levels, suggesting that there is skeletal muscle insulin resistance, rather than pancreatic dysfunction. Accordingly, the insulin's ability to lower blood glucose was markedly diminished in *Sirt3*$^{-/-}$-*Ucp2*$^{-/-}$mice during an insulin tolerance test, compared to WT mice (**Figure 2. 16A**). Moreover, Akt phosphorylation was impaired in the gastrocnemius muscle collected from *Sirt3*$^{-/-}$-*Ucp2*$^{-/-}$mice during the insulin tolerance test, whereas the Akt phosphorylation increased appropriately in WT gastrocnemius muscle (**Figure 2. 16B**). This finding also supported insulin resistance in *Sirt3*$^{-/-}$-*Ucp2*$^{-/-}$mice, likely because of impaired insulin signaling immediately downstream from the insulin receptor.

2.5. Discussion

Our work supports the metabolic theory of PAH which suggests that mitochondrial suppression is central to the pathogenesis of PAH, and not secondary or downstream to other abnormalities described in PAH pathogenesis[2,48]. There are two important and novel findings in our work:

First, we describe a somewhat unexpected high prevalence of loss-of-function SNPs in 2 genes encoding mitochondrial proteins in a small but well-characterized prospective cohort of PAH patients, in whom we collected blood at the time of their original assessment and we followed over the past 10 years. We found a provocative association between these SNPs and the severity of PAH or the presence of type 2 diabetes (a previously described feature of PAH patients that

remains unexplained[36,51]) and outcomes (death or transplantation), which clearly needs to be prospectively studied in larger and independent studies, before it can be claimed to be either true or causal (**Table 2. 1; Figure 2. 1B**). Moreover, PAH affects more women than men, but the prognosis of male patients is worse than female patients. This is in keeping with our data since male PAH patients have higher SNP score than female. For example, 33% of male patients have SNP score 2-3 compared to 23% in female patients, while 36% of female patients have SNP score 0 compared to 23% of male patients; and a higher SNP score correlates positively with PAH severity and outcomes (death and transplantation). However, the overall small sample size does not allow for any conclusive statements when it comes to outcomes, other that hypothesis generation.

The fact that all patients received the same protocol-driven therapeutic approach, the absence of significant comorbidities upon entering the cohort, along with the fact that PAH therapies are not known to affect survival[32], allow us to report this association with outcomes. Importantly, we previously showed that PAH patients with a high SNP score for these two SNPs had more inhibited PDH function and mitochondrial respiration than patients without SNPs, studied in lungs right after they were explanted at transplant surgery[22]. The *SIRT3* SNP variant (rs11246020) that affects the enzyme's catalytic activity has been shown to decrease the enzymatic activity of Sirt3 in patient carriers[29]. Carriers of the *UCP2* SNP (rs659366) that affects the promoter of the gene, have a variant-dependent decrease in *UCP2* mRNA in the subcutaneous fat (i.e. the SNP homozygotes have the lowest level, followed by the heterozygotes and the patients carrying both wild-type alleles)[28]. Yet another study showed that the carriers of the same SNP had increased levels of *Ucp2* mRNA in the intra-abdominal fat, suggesting that the regulation of *Ucp2* is tissue-dependent and may also be affected by additional factors[63]. In summary, although from

our small sample size we cannot be certain that this association will stand when tested in other multicenter and larger cohorts, we believed it deserved mechanistic exploration in an animal model that mimics the loss of function of *Sirt3* and *Ucp2*.

Second, we created a novel mouse model of PAH in which to explore our clinical data, and we found that it has more features of human PAH than in previously described rodent models. **First**, the severe PHT found in mice lacking both *Sirt3* and *Ucp2* is spontaneous, occurs at a young age and leads to definitive objective features of RV failure, i.e. increased RA pressure, decreased CO, dilatation of the RV and a significant decrease in RV function (studied in vivo with TAPSE) (**Figure 2. 3A**). **Second**, After following the strict pathology criteria that have been described for these plexogenic lesions in both the rat sugen/hypoxia model and humans[7,25], we found these mice had frequent plexogenic lesions, even at the age of 2 months, before the establishment of hemodynamic evidence of PHT (at least at rest) (**Figure 2. 6 and 2.10**). There is no other mouse model that shows frequent and predictable plexogenic lesions. This finding may offer a potential answer to the question of whether the plexogenic lesions follow or precede the increase in PA pressures. If anything, existing models (i.e. the Sugen/hypoxic rat model) had suggested that these lesions appear late in the disease when PHT is already severe[25]; and human data (because of the lack of biopsies at earlier stages of the disease) cannot provide an answer[54]. **Third**, we found an increased infiltration of the pulmonary arterioles with $CD4^+$ T cells (**Figure 2. 11**). Recently, the role of inflammation in PAH has emerged as central to the pathogenesis of PAH[49,57]. The lack of these 2 mitochondrial proteins from T cells themselves is predicted to facilitate their activation, since inhibition of oxidative phosphorylation is both necessary and precedes T cell activation[50]. Thus, we cannot determine whether the increased infiltration of T cells in the pulmonary vessels of these mice is a result of signaling from the lung microenvironment or it reflects T cell activation

in the bone marrow. On the other hand, considering the presence of these SNPs in patients, the same applies to patients having suppressed mitochondrial function throughout the body. **Fourth**, the insulin resistance found in the *Sirt3*$^{-/-}$-*Ucp2*$^{-/-}$ without the addition of high fat diet (**Figure 2.16A**), mimics clinical PAH, where some patients have evidence of unexplained metabolic syndrome without being obese. A hypothesis that stems from our work is that the patients with insulin resistance and skeletal muscle mitochondrial suppression, reported previously by other groups[36,51], may actually be patients with higher SNP scores for *SIRT3* and *UCP2* allelic SNPs. *Sirt3* KO mice are predisposed to insulin resistance in keeping with our data[29]. *Ucp2* KO mice are also predisposed to diabetes as they exhibit suppressed glucose induced insulin secretion[64] (although in our case we found insulin resistance and not diabetes relating to pancreas dysfunction) but this appears to depend on mice background[65]. Regardless of their background, the fact that severe PAH coexists with insulin resistance in the same animal with a global mitochondrial deficiency, directly supports our clinical finding that the presence of these SNPs is associated with the presence of type 2 diabetes in PAH patients. It also allows us to speculate that this association is potentially causal. In fact, the skeletal muscle from the offspring of patients with type 2 diabetes has insulin resistance because of an inherited defect in oxidative phosphorylation[66], a finding similar to what is reported for the skeletal muscle of PAH patients[51].

Another important aspect of our work is that, while in our patient cohort the correlation of SNP score with the severity of PAH (PVR, outcomes) was weak (but statistically significant), our mice showed a very strong and positive gene dose-dependent relation between the loss of *Sirt3*/*Ucp2* and the increase in PA pressure, as well as the worsening of RV failure (RV end-diastolic diameter, RA pressure, CO and TAPSE) and vascular remodeling (**Figure 2. 3A**). This supports our clinical data showing a correlation between the SNP score and PVR. Our animal

ethics committee did not allow us to perform death end-point studies, but the degree of RV failure and the clinical signs of the *Sirt3*$^{-/-}$-*Ucp2*$^{-/-}$and *Sirt3*$^{-/-}$-*Ucp2*$^{+/-}$ *or Sirt3*$^{+/-}$-*Ucp2*$^{-/-}$ mice (decreased activity/withdrawal, decrease appetite, irritability) suggested a significant burden of disease requiring euthanasia. Thus, our mice data also support the association of these SNPs with outcomes (death or transplantation) in our clinical cohort.

Since mouse models of PAH have been criticized for the lack of important clinical features of human PAH (including the mild increase in PA pressures and the lack of plexogenic lesions), our new mouse PAH model may prove to be helpful in the field. Mice are far more useful in molecular and genetic studies than other animal models. In the future, our mice could be crossed with other KO or transgenic mice that lack genes that either worsen or protect from PAH, further improving our tools for the study of PAH, a disease that is clearly multifactorial.

Two month-old *Sirt3*$^{-/-}$-*Ucp2*$^{-/-}$ mice have plexogenic lesions but normal PA pressures. Therefore, it appears that even in the early phase of the disease (2 month-old), the lack of *Ucp2* and *Sirt3* still induces hyperproliferative phenotype of PASMCs, pulmonary artery endothelial cells (PAECs) and fibroblasts which are components of plexogenic lesion (we stained for both PASMCs and PAECs). The observed proliferation of PAEC maybe a repair response to an initial loss/injury of PAEC, as some theories suggest for early PAH. Our data show that at this very young age however, there is already evidence of proliferation throughout the vascular wall, although the possibility of increased loss of PAEC at an even earlier stage cannot be excluded. We have previously summarized in original publications and reviews the potential mechanisms that are downstream of mitochondrial suppression (both in PAH and cancer), which explain both the proliferation and anti-apoptotic phenotype in PASMCs, including the mechanism of activation of critical transcription factors that have been shown to be activated in human and animal PAH[2,16,48]

(**Figure 2. 16C**). In addition to loss of *Sirt3* and *Ucp2*, other factors have been shown to contribute to the mitochondrial suppression in PAH PASMCs, including endoplasmic reticulum stress[59,67], or abnormalities in mitochondrial fission/fusion[68,69]. Our current work now further suggests that mitochondrial suppression is not only "permissive" for the development of PAH, as we have previously suggested in our metabolic theory of PAH[2,16,48], but may be actually causal, since these mice recapitulate many features of human PAH.

We also previously proposed that although mitochondrial abnormalities may be present throughout the body, the fact that the vascular phenotype is restricted to the lung vasculature, may have to do with the fact that there are differences between pulmonary vascular mitochondria and systemic vascular mitochondria[70] (a fact that may also explain why hypoxic pulmonary vasoconstriction is a specific feature of the pulmonary and not systemic circulation), making cells in pulmonary microvessels more responsive earlier to mitochondrial abnormalities, than cells in systemic vessels. Although we did not study that in detail, we did not observe systemic vascular abnormalities, at least enough to affect LVEDP. This allowed us to "diagnose" PAH in these mice, but we cannot be certain that these mice would not develop systemic vascular diseases if they were to survive to grow older.

Since *Sirt3* KO mice have also been shown to develop pulmonary fibrosis[71], it is possible that our *Sirt3*$^{-/-}$-*Ucp2*$^{-/-}$ mice may develop worsening pulmonary fibrosis with age, although they did not have anatomic evidence of fibrosis or hypoxemia at the time that we studied them. If these mice were to develop pulmonary fibrosis with age (either directly or secondary to inflammation) they would still be relevant to the clinical associated PAH because of collagen vascular diseases like scleroderma, which is characterized by pulmonary fibrosis in addition to PAH.

However, this study also has some limitations. Firstly, the size of PAH patient cohort is small, so we were not able to analyse the subgroups of SNP score 2-3 to show whether there are any differences between *SIRT3* SNP and *UCP2* SNP. Secondly, to support the human data, our mouse model used gene knockout (KO) rather than a mouse expressing the human SNP. This is extraordinarily difficult and even more difficult is to express two human SNPs. On the other hand, the double KO mice allowed us to also study the lack of genes in a variety of homozygote/heterozygote combinations, allowing is to assess "gene dose-dependent" associations, that strengthen the causality aspect of our mechanism. Thirdly, we cannot rule out primary effects of *Ucp2* or *Sirt3* loss on the RV myocardium. However, because the left ventricular size and function was not affected, this somewhat unlikely. In addition, the mild RV enlargement and dysfunction that we noted in our young mice is not out of proportion with the degree of PAH that we measured.

In conclusion, our mouse model supports our provocative clinical data in our cohort and is directly relevant to a subgroup of PAH patients carrying more than one loss-of-function SNPs in genes encoding mitochondrial proteins, particularly those that carry them in both alleles.

Table 2.1. Single nucleotide polymorphism (SNP) scores for *UCP2*/*SIRT3* and clinical information related to the PAH cohort.

	age	sex	type	mPAP (mmHg)	PVR (dyn·s/cm^5)	type 2 DM	meds	outcomes	*SIRT3*	*UCP2*	SNP score
1	63	F	aPAH	40	429	Y	P, E	Dead	V/Wt	V/Wt	2
2	62	F	aPAH	52	665	Y	P	Alive	Wt/Wt	V/Wt	1
3	77	M	iPAH	54	804	N	P, E, Pr	Alive	Wt/Wt	V/Wt	1
4	78	M	iPAH	52	752	N	P, E	Dead	Wt/Wt	V/Wt	1
5	74	M	aPAH	47	663	Y	P, E	Dead	V/Wt	V/Wt	2
6	48	M	iPAH	61	905	N	P, E, Pr	Alive	V/Wt	Wt/Wt	1
7	38	F	aPAH	60	634	N	P	Dead	Wt/Wt	V/Wt	1
8	66	F	aPAH	48	1376	N	P, E, Pr	Dead	Wt/Wt	V/V	2
9	68	F	aPAH	40	695	N	P, E, Pr	Alive	V/Wt	Wt/Wt	1
10	64	F	aPAH	28	597	N	P	Alive	Wt/Wt	V/Wt	1
11	53	F	iPAH	64	1429	N	P, E	Alive	V/Wt	Wt/Wt	1
12	67	F	aPAH	39	281	N	P	Alive	Wt/Wt	Wt/Wt	0
13	52	F	aPAH	70	609	N	P, E, Pr	Alive	V/Wt	Wt/Wt	1
14	46	F	iPAH	68	838	Y	P, Pr	Alive	Wt/Wt	V/V	2
15	45	F	aPAH	44	451	N	P, E	Dead	V/Wt	Wt/Wt	1
16	73	M	iPAH	53	640	N	P, E	Dead	V/Wt	V/Wt	2
17	55	M	aPAH	59	812	N	P, E, Pr	Alive	V/Wt	V/Wt	2
18	70	M	aPAH	60	580	N	P, E, Pr	Dead	Wt/Wt	V/V	2
19	63	F	aPAH	54	567	N	P,Pr	Alive	Wt/Wt	Wt/Wt	0
20	36	M	iPAH	68	1011	N	P, Pr	Transpl	V/Wt	V/Wt	2

21	48	F	aPAH	51	1502	N	P, Pr	Dead	Wt/Wt	V/Wt	1
22	51	F	aPAH	42	463	N	P, E	Alive	Wt/Wt	Wt/Wt	0
23	48	F	iPAH	69	709	N	P, E	Alive	Wt/Wt	V/Wt	1
24	24	F	iPAH	37	348	N	P, E	Alive	Wt/Wt	Wt/Wt	0
25	57	M	iPAH	55	775	N	P, E, Pr	Alive	Wt/Wt	Wt/Wt	0
26	72	M	iPAH	60	584	Y	P	Dead	Wt/Wt	V/Wt	1
27	74	M	iPAH	48	417	N	P	Dead	Wt/Wt	V/Wt	1
28	40	F	iPAH	48	950	N	P,E	Alive	Wt/Wt	Wt/Wt	0
29	22	F	iPAH	48	1097	N	P, E, Pr	Alive	V/Wt	Wt/Wt	1
30	70	F	iPAH	58	987	N	P, Pr	Alive	Wt/Wt	V/V	2
31	58	M	iPAH	94	1387	N	P, Pr	Dead	V/V	Wt/Wt	2
32	31	M	aPAH	29	434	N	P	Alive	V/Wt	Wt/Wt	1
33	58	M	aPAH	27	316	N	P	Alive	Wt/Wt	Wt/Wt	0
34	42	M	iPAH	65	592	N	P, E	Dead	Wt/Wt	V/Wt	1
35	70	F	iPAH	62	527	Y	P, Pr	Dead	Wt/Wt	Wt/Wt	0
36	53	M	iPAH	52	770	N	P, E	Dead	V/Wt	V/Wt	2
37	43	F	iPAH	34	465	N	P	Alive	Wt/Wt	V/V	2
38	36	F	iPAH	52	710	N	P, E	Dead	Wt/Wt	Wt/Wt	0
39	71	F	aPAH	31	480	N	P, E	Dead	Wt/Wt	Wt/Wt	0
40	73	F	aPAH	40	493	N	P, E, Pr	Dead	Wt/Wt	V/Wt	1
41	57	M	aPAH	37	617	N	P, B	Dead	Wt/Wt	V/Wt	1
42	49	M	aPAH	39	512	N	P	Alive	Wt/Wt	Wt/Wt	0
43	51	F	aPAH	29	336	N	P, E	Dead	Wt/Wt	V/Wt	1
44	56	F	iPAH	69	850	N	P, E, Pr	Dead	Wt/Wt	Wt/Wt	0
45	31	F	iPAH	26	357	N	P	Alive	Wt/Wt	Wt/Wt	0

46	74	F	aPAH	43	311	Y	P, E	Dead	Wt/Wt	V/Wt	1
47	31	F	iPAH	70	738	N	P, E	Alive	Wt/Wt	Wt/Wt	0
48	70	F	iPAH	51	710	N	P,E	Alive	V/Wt	Wt/Wt	1
49	60	F	iPAH	59	648	Y	P, E	Dead	Wt/Wt	V/Wt	1
50	48	M	aPAH	86	1067	N	P,E	Dead	Wt/Wt	V/Wt	1
51	44	F	aPAH	25	309	N	P	Dead	Wt/Wt	V/Wt	1
52	50	F	aPAH	60	832	N	P,E	Alive	V/Wt	V/V	3
53	71	M	iPAH	42	640	N	P, E	Dead	Wt/Wt	Wt/Wt	0
54	54	F	aPAH	45	577	N	P, E	Dead	Wt/Wt	Wt/Wt	0
55	47	F	iPAH	58	756	N	P, E, Pr	Dead	V/V	Wt/Wt	2
56	24	F	iPAH	56	912	N	P, E, Pr	Transpl	Wt/Wt	Wt/Wt	0
57	27	F	iPAH	50	1050	N	P, E, Pr	Dead	V/Wt	V/Wt	2
58	19	M	aPAH	40	334	N	P	Alive	Wt/Wt	Wt/Wt	0
59	61	F	iPAH	57	800	N	P, E, Pr	Dead	Wt/Wt	V/V	2
60	36	F	iPAH	52	710	Y	P,E	Alive	Wt/Wt	Wt/Wt	0

aPAH = associated Pulmonary arterial Hypertension

iPAH = idiopathic Pulmonary Arterial Hypertension

P = Phosphodiesterase type 5 inhibitors

E = Endothelin Receptor Antagonists

Pr = Prostacyclin analogues

V = gene variant (SNP)

Wt = wild type (normal

A

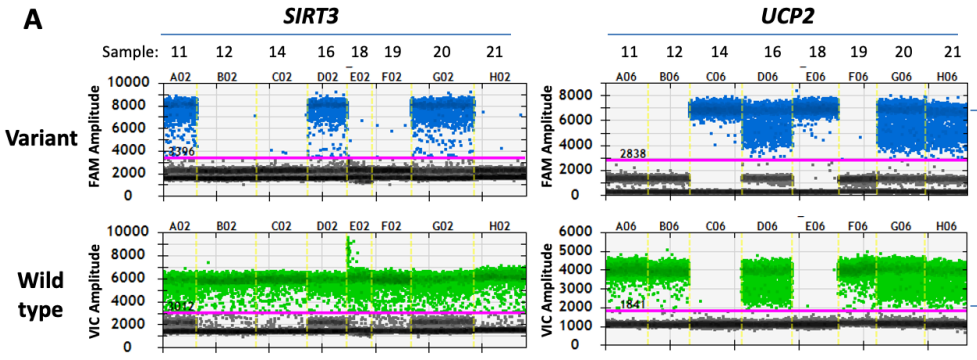

Sample	*Sirt3*	*Ucp2*
11	V/Wt	Wt/Wt
12	Wt/Wt	Wt/Wt
14	Wt/Wt	V/V
16	V/Wt	V/Wt
18	Wt/Wt	V/V
19	Wt/Wt	Wt/Wt
20	V/Wt	V/Wt
21	Wt/Wt	V/Wt

V = variant (SNP)
Wt = wild type

B

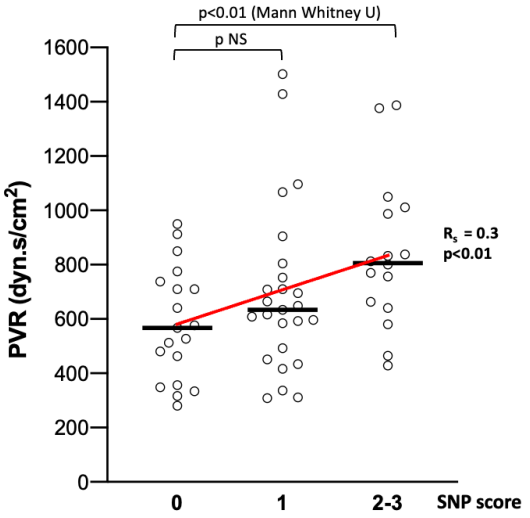

SNP score	0	1	2-3
PVR (mean)	605	687	837
Death number (%) *Attributable risk (c/w SNP 0)*	7 (36)	13 (52) **29%**	11 (69) **47%**
DM type 2 number (%) *Attributable risk (c/w SNP 0)*	1 (5)	3 (12) **58%**	3 (19) **75%**
Mean age	50	55	55
% male	27	32	43
n	19	25	16

Figure 2. 1. SIRT3 and UCP2 single nucleotide polymorphisms (SNPs) in a cohort of PAH patients.

A) Representative PCR studies of a few PAH patients showing how the detection of the gene variant (SNP) or the wild type gene in each of the two alleles, allowed us to calculate the SNP score for each patient. For each sample the presence of "hits" above the threshold line (in pink) determines whether the variant is in none (Wt/Wt), one (V/Wt) or both alleles (V/V). **B)** Spearman coefficient of 0.3 shows a weak but statistically significant ($p<0.01$) correlation between the SNP score and the pulmonary vascular resistance (PVR) (see Table 1). (**left**) Mann Whitney U testing shows a significant difference between SNP score 0 and 2-3. The sample size, the % of death/transplantation and the % of type 2 diabetes for each SNP score group as well as the attributable risk for the SNP 1 and SNP 2-3 groups (compared to the SNP 0 group) is shown in the table to the **right**. c/w indicates compared with; DM, diabetes mellitus; FAM, fluorescein amidite; NS, not significant; PCR, polymerase chain reaction; SIRT3, sirtuin3; UCP2, uncoupling protein 2; V, variant; and Wt, wild type.

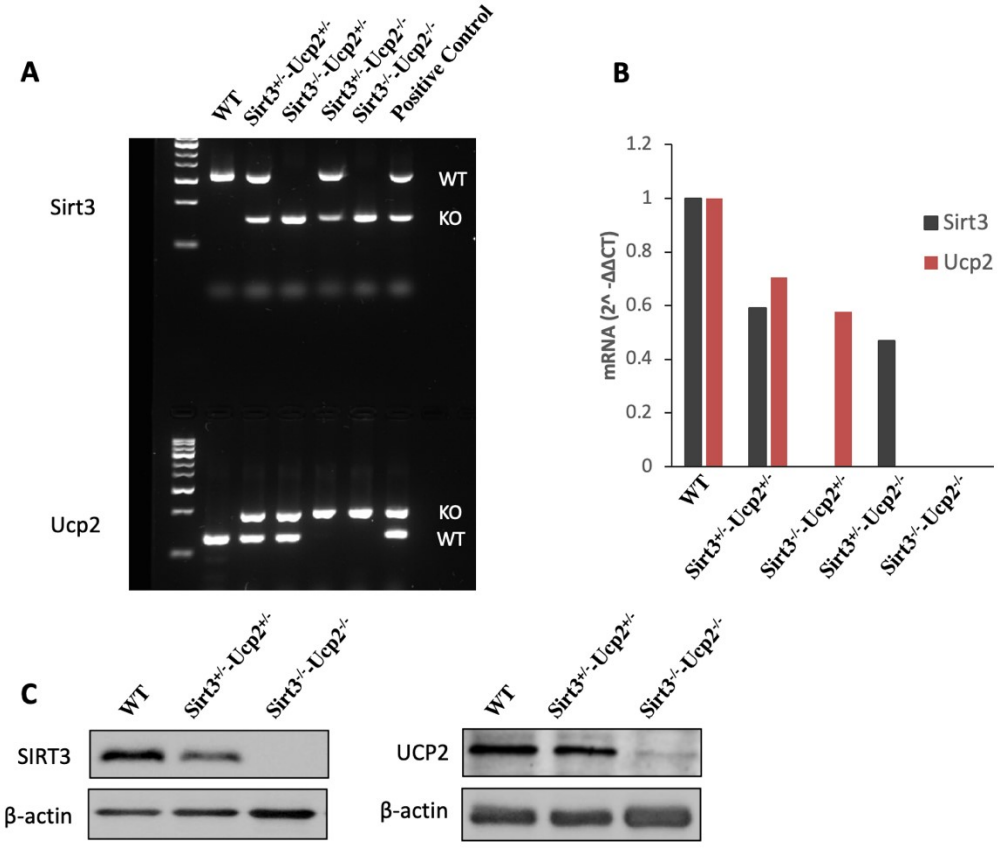
A
WT
Sirt3+/-Ucp2+/-
Sirt3-/-Ucp2+/-
Sirt3+/-Ucp2-/-
Sirt3-/-Ucp2-/-
Positive Control
Sirt3
WT
KO
Ucp2
KO
WT
B
mRNA (2^ -ΔΔCT)
1.2
1
0.8
0.6
0.4
0.2
0
Sirt3
Ucp2
WT
Sirt3+/-Ucp2+/-
Sirt3-/-Ucp2+/-
Sirt3+/-Ucp2-/-
Sirt3-/-Ucp2-/-
C
WT
Sirt3+/-Ucp2+/-
Sirt3-/-Ucp2-/-
SIRT3
β-actin
WT
Sirt3+/-Ucp2+/-
Sirt3-/-Ucp2-/-
UCP2
β-actin

Figure 2. 2. Genotyping of Sirt3 and UCP2.

A. Representative PCR blot confirming the genotype for the Sirt3 and Ucp2 mutant mice. Sirt3 mutant mice have deletion of exons 2-3. Based on the primer sequences used, the wild type allele shows at 562bp and the mutant allele shows at 200bp. The Sirt3 heterozygous mice are positive for both alleles (Top blot). The Ucp2 mutant mice have an insertion of a PGK- NEO cassette replacing exons 3-7 to create the larger mutant allele. The Ucp2 mutant allele shows at 280bp, while the wild type allele shows at 156bp. The Ucp2 heterozygous mice are positive for both alleles (bottom). **B.** qRT-PCR (in lung tissues) shows that the double knockout mice have no detectable levels of Sirt3 or Ucp2 mRNA, compared to wild type controls, while the double heterozygous mice express ~50% mRNA levels. **C.** Lung tissue from mice heterozygous or homozygous to the lack of both genes shows no detectable levels of either Sirt3 or Ucp2, and decreased expression of either SIRT3 or UCP2 compared to WT mice, using immunoblots. The remaining "smear" in the Ucp2 blot of $Sirt3^{-/-}$-$Ucp2^{-/-}$ mice, is likely due to the well-known cross- reactivity of the Ucp2 antibody with Ucp3, in all known commercially available antibodies (Ucp2 shares a 72% homology with Ucp3).

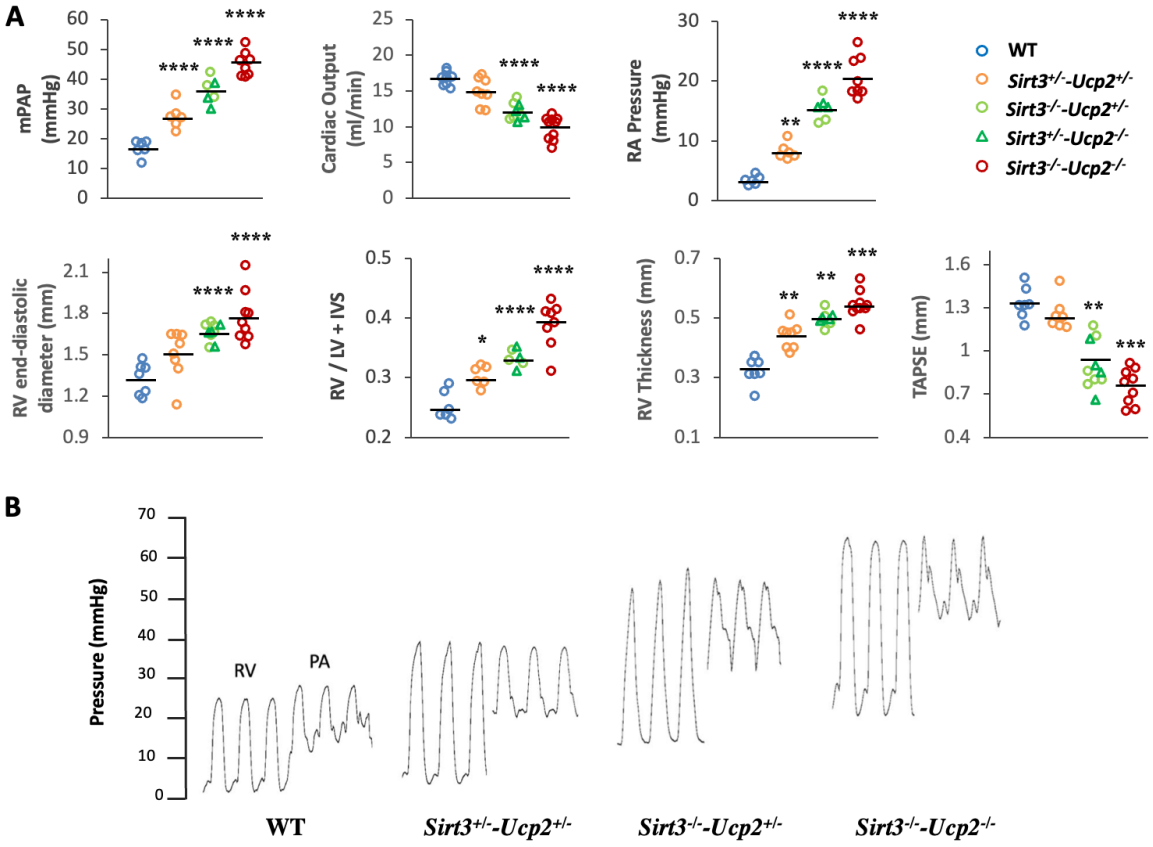
A
mPAP (mmHg)
Cardiac Output (ml/min)
RA Pressure (mmHg)
RV end-diastolic diameter (mm)
RV / LV + IVS
RV Thickness (mm)
TAPSE (mm)
WT
Sirt3+/--Ucp2+/-
Sirt3-/--Ucp2+/-
Sirt3+/--Ucp2-/-
Sirt3-/--Ucp2-/-
B
Pressure (mmHg)
RV
PA
WT
Sirt3+/--Ucp2+/-
Sirt3-/--Ucp2+/-
Sirt3-/--Ucp2-/-

Figure 2. 3. A gene dose-dependent effect on the severity of PAH in mice heterozygote or homozygote to the loss of both Sirt3 and Ucp2.

A) Several parameters measured by closed-chest right heart catheterization (mean PA pressure, RA pressure), echocardiography (cardiac output, RV thickness, RV end-diastolic diameter, TAPSE) or measured after euthanasia (RV/LV+septum weight) are shown. In each graph, the third column of data shows a mixture of *Sirt3*$^{+/-}$-*Ucp2*$^{-/-}$ or *Sirt3*$^{-/-}$-*Ucp2*$^{+/-}$, represented by circles or triangles. These two groups were graphed together since their values were similar. For mPAP, Cardiac Output, RV diameter: ****p<0.0001; for RA pressure: **p=0.008, ****p<0.0001; for RV/ LV+IVS: *p=0.024, ****p<0.0001; for RV Thickness: **p=0.0008, ***p=0.0004; for TAPSE: **p=0.0006, ***p=0.0009, compared to WT mice. These comparisons (as well as in the subsequent figures) were done post hoc (Bonferroni) since the overall one-way ANOVA for the groups was significant. **B)** Representative tracings of RV and PA pressures in several mice groups. IVS indicates Interventricular septum; LV, left ventricular; mPAP, mean pulmonary artery pressure; PA, pulmonary artery; PAH, pulmonary arterial hypertension; RA, right atrium; RV, right ventricular; Sirt3, sirtuin3; Ucp2, uncoupling protein 2; TAPSE, tricuspid annular plane systolic excursion; and WT, wild type.

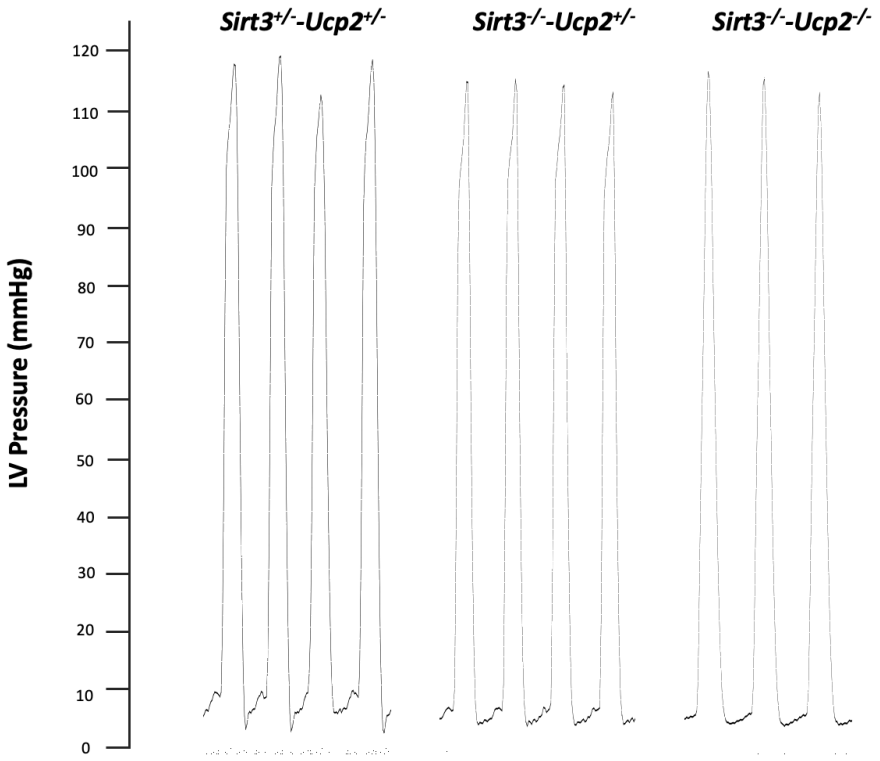

Figure 2. 4. LVEDP of mice heterozygote or homozygote to the loss of both Sirt3 and Ucp2.

Representative Left ventricular end-diastolic pressure (LVEDP) traces from anesthetized mice lacking Sirt3 and Ucp2 shows that they all have normal values.

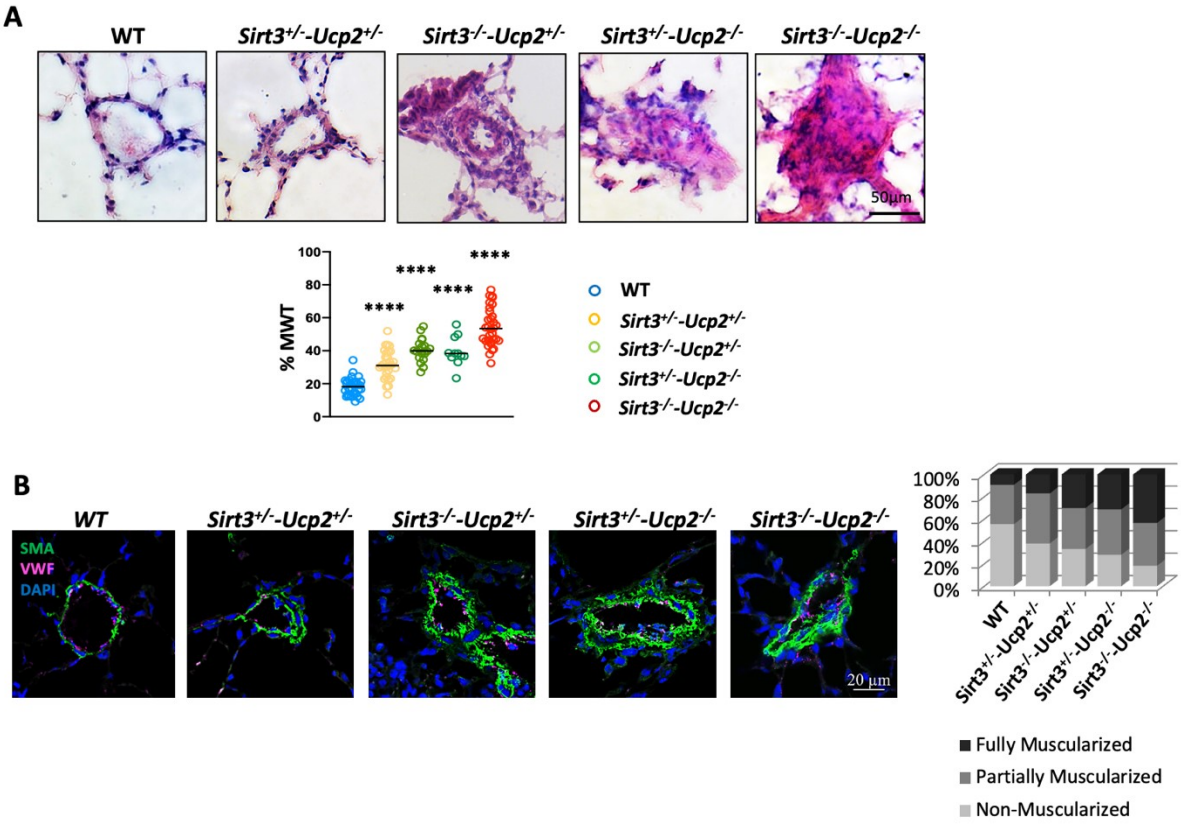
A
WT
Sirt3+/-Ucp2+/-
Sirt3-/-Ucp2+/-
Sirt3+/-Ucp2-/-
Sirt3-/-Ucp2-/-
50μm
% MWT
100
80
60
40
20
0
****
****
****
****
WT
Sirt3+/-Ucp2+/-
Sirt3-/-Ucp2+/-
Sirt3+/-Ucp2-/-
Sirt3-/-Ucp2-/-
B
WT
Sirt3+/-Ucp2+/-
Sirt3-/-Ucp2+/-
Sirt3+/-Ucp2-/-
Sirt3-/-Ucp2-/-
SMA
VWF
DAPI
20 μm
100%
80%
60%
40%
20%
0%
WT
Sirt3+/-Ucp2+/-
Sirt3-/-Ucp2+/-
Sirt3+/-Ucp2-/-
Sirt3-/-Ucp2-/-
Fully Muscularized
Partially Muscularized
Non-Muscularized

Figure 2. 5. Pulmonary vascular remodeling in mice heterozygote or homozygote to the loss of both Sirt3 and Ucp2.

A) Representative images (H&E staining) from lungs of all the mice groups along with mean data of % medial wall thickness (MWT) of pulmonary arterioles (40-300μm) are shown. ****$p<0.0001$ compared to WT mice. These comparisons were done post hoc (Bonferroni) since the overall one-way ANOVA for the groups was significant. n=35 arteries/group.

B) Representative confocal images of small arterioles (<40μm) and mean data of % muscularization are shown. SMA: smooth muscle actin, vWF: von Willebrand factor (marking endothelial cells), DAPI (nuclear stain). The mean percent muscularization is shown to the right. n=50 arteries/group.

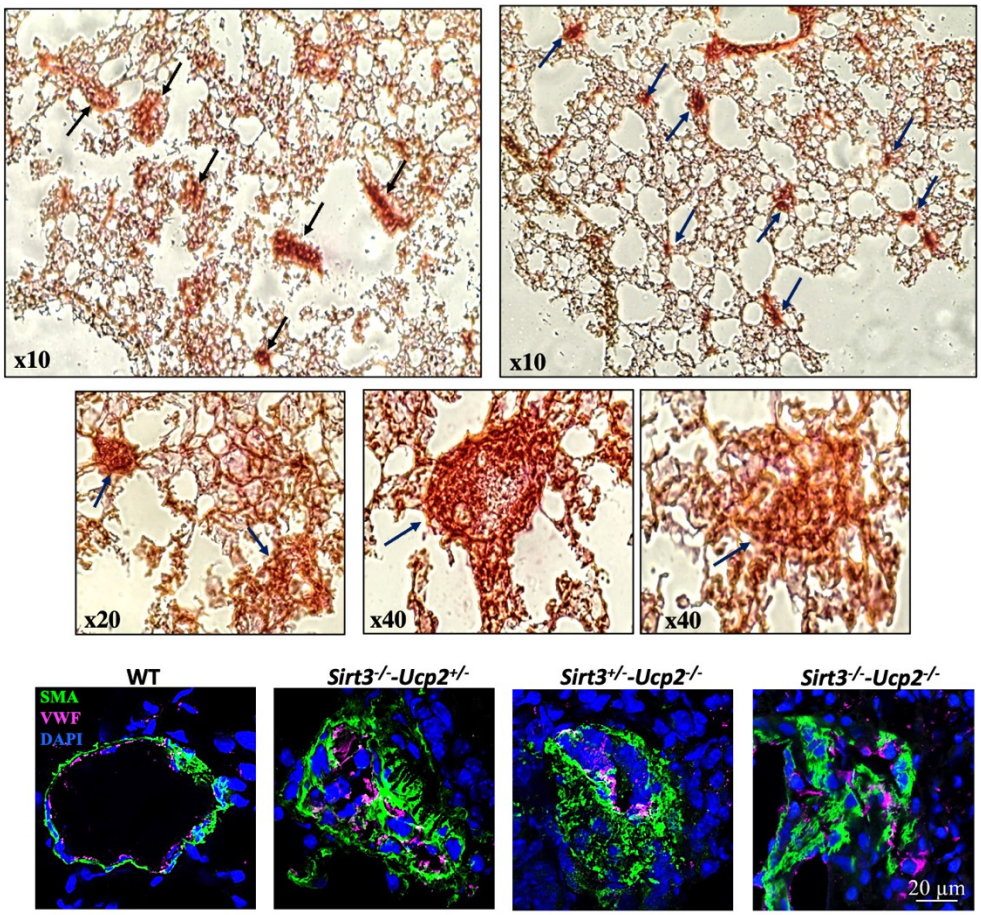

Figure 2. 6. Plexogenic arteriopathy in mice lacking both Sirt3 and Ucp2.

Representative pictures of lung histology (top) and confocal immunohistochemistry of small pulmonary arteries from *Sirt3*$^{+/-}$-*Ucp2*$^{-/-}$, *Sirt3*$^{-/-}$-*Ucp2*$^{+/-}$, and *Sirt3*$^{-/-}$-*Ucp2*$^{-/-}$ mice. Arrows indicate plexogenic lesions in top 5 images. DAPI indicates 4',6-diamidino-2- phenylindole (nuclear stain); Sirt3, sirtuin3; SMA, smooth muscle actin; Ucp2, uncoupling protein 2; and vWF, von Willebrand factor (marking endothelial cells).

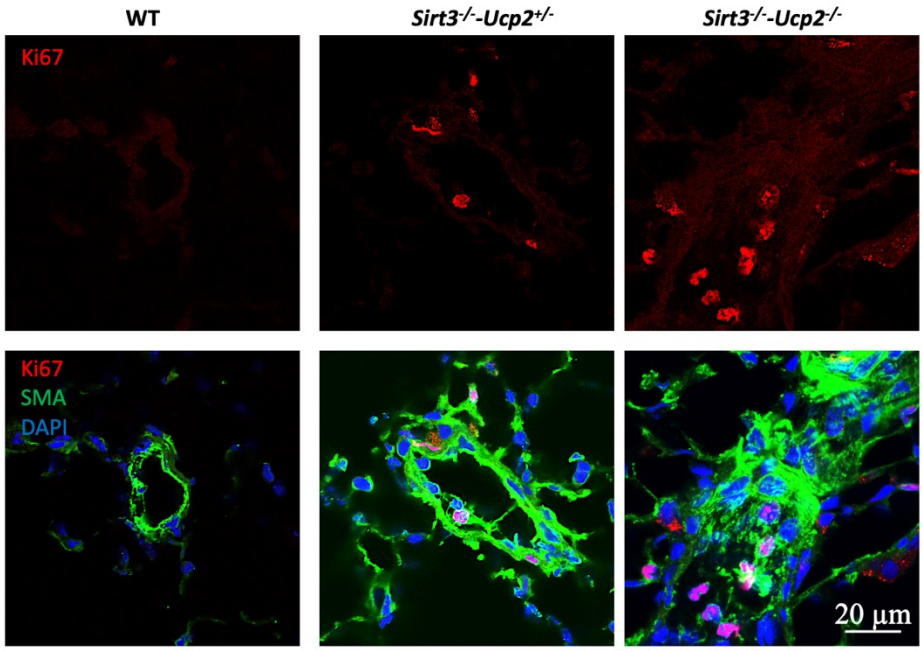

Figure 2. 7. Proliferative vascular cells in pulmonary arteries from mice heterozygote or homozygote to the loss of both Sirt3 and Ucp2.

Representative confocal immunohistochemistry images of pulmonary arteries from mice lacking *Sirt3* and *Ucp2* shows that they express higher levels of the proliferation marker Ki67 in their vascular wall.

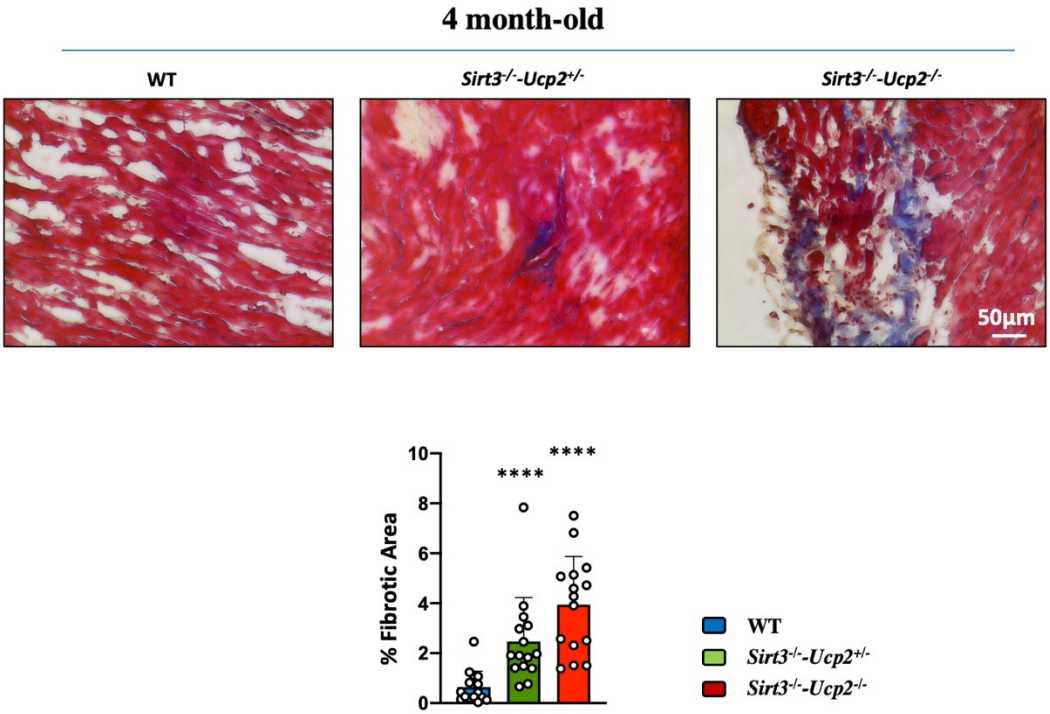

Figure 2. 8. Right ventricular fibrosis of mice heterozygote or homozygote to the loss of both Sirt3 and Ucp2.

Representative Masson's trichrome pictures of right ventricles from Sirt3$^{-/-}$-Ucp2$^{+/-}$ and Sirt3$^{-/-}$-Ucp2$^{-/-}$ mice shows that they have a significant increase of fibrosis compared to WT mice. ****p<0.0001 (Kruskal-Wallis test) compared to WT mice, n=15 images from 3 mice / group.

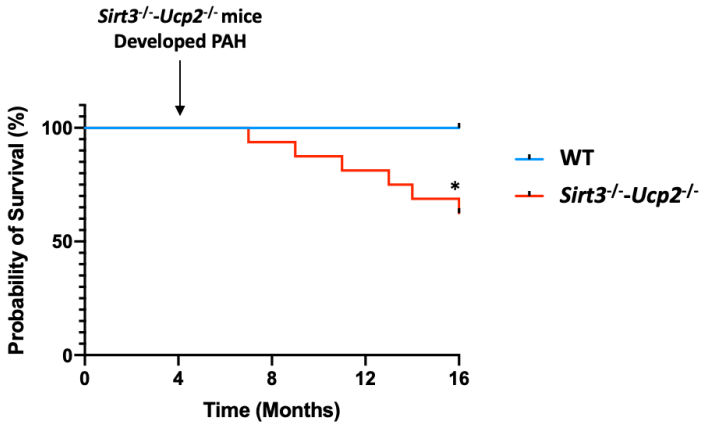

Figure 2. 9. survival of mice lacking both Sirt3 and Ucp2

Sixteen-month (12 months after developing PAH) Kaplan-Meier survival plot shows the Sirt3$^{-/-}$-Ucp2$^{-/-}$ mice have decreased survival compared to WT mice. *$p<0.05$ compared to WT mice, n=16 mice / group.

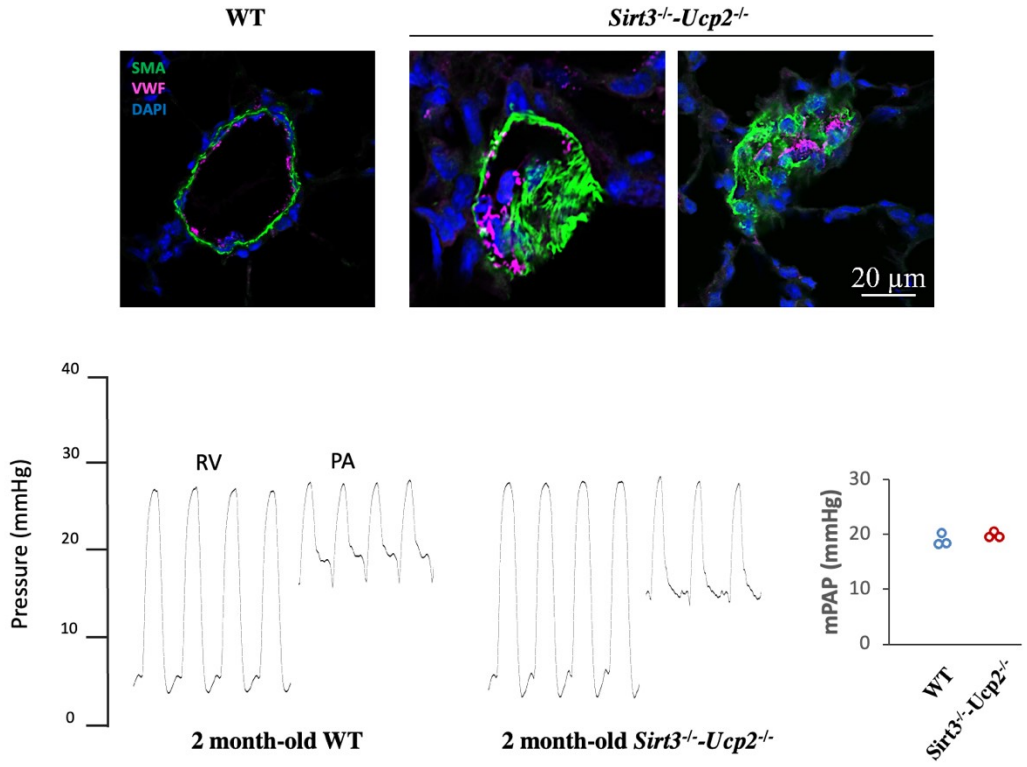

Figure 2. 10. The formation of plexogenic lesions is earlier than the rise of mean pulmonary arterial pressure.

Confocal immunohistochemistry of small pulmonary arteries (showing plexogenic lesions) as well as right heart catheterization data (pulmonary artery tracings and mean PA pressure data) shows normal pressures in 3 WT and 3 Sirt3$^{-/-}$-Ucp2$^{-/-}$ 2 month-old mice, suggesting that the plexogenic arteriopathy is a very early event in the disease process. mPAP: mean pulmonary arterial pressure.

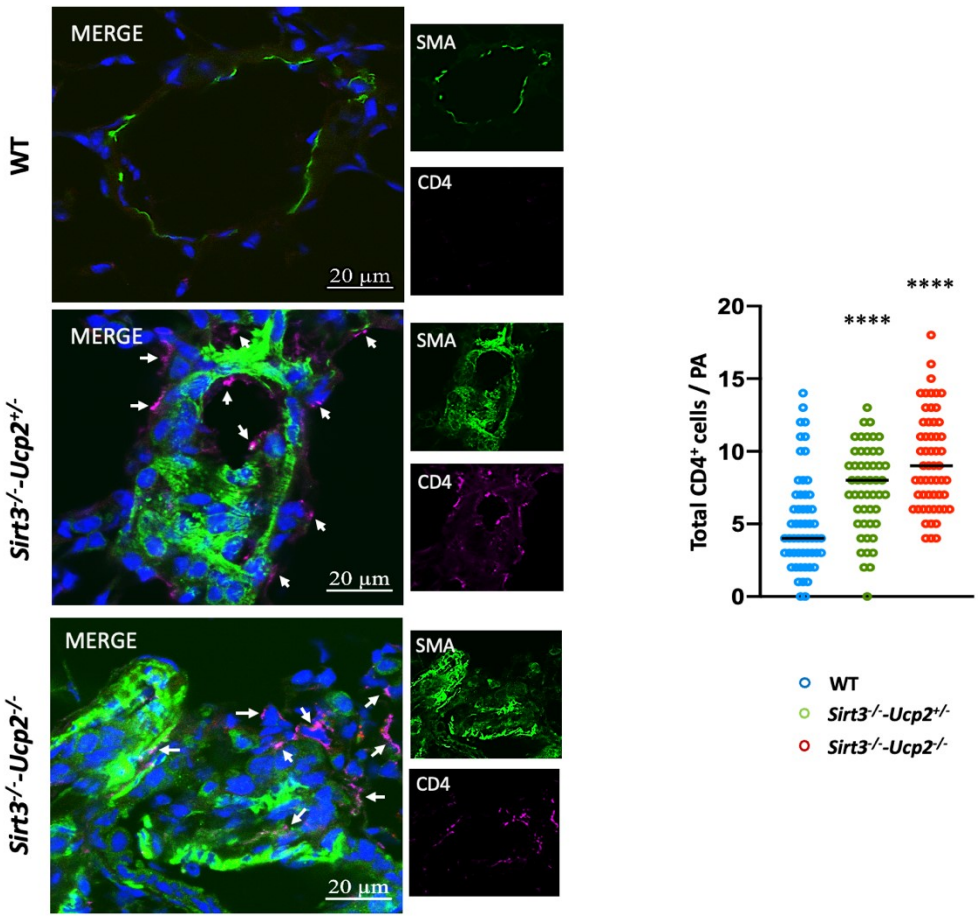

Figure 2. 11. CD4 T cells mice heterozygote or homozygote to the loss of both Sirt3 and Ucp2.

Representative confocal immunohistochemistry images of small pulmonary arteries and mean data shows increased $CD4^+$ T cells within and around the vascular wall of $Sirt3^{-/-}$- $Ucp2^{+/-}$, and $Sirt3^{-/-}$-$Ucp2^{-/-}$ mice compared to WT mice. ****p<0.0001 (Bonferroni) compared to WT mice, n = 50 arteries / group.

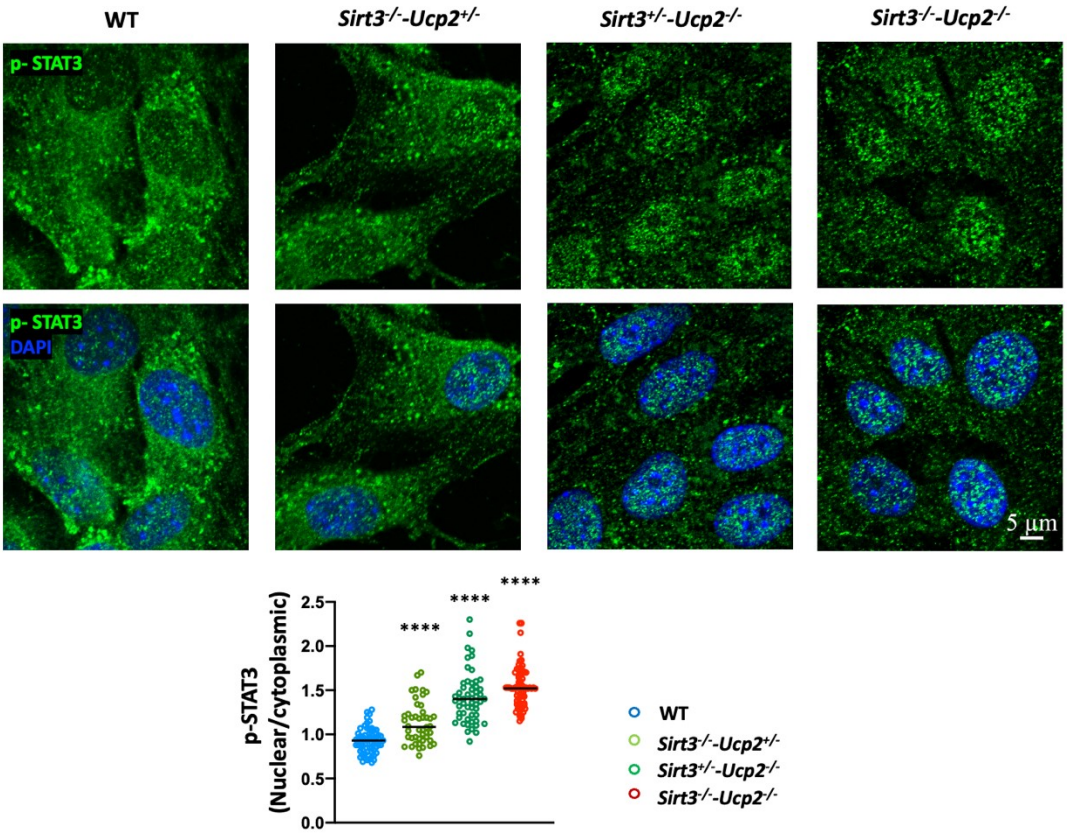

Figure 2. 12. Proliferative phenotype in cultured PASMCs from mice heterozygote or homozygote to the loss of both Sirt3 and Ucp2.

Representative confocal immunohistochemistry images of PASMCs shows increased ratio of nuclear/cytoplasmic of ^{Y705}p-STAT3 in PASMCs from mice lacking Sirt3 and Ucp2 compared to PASMCs from WT mice. ****p<0.0001 (Bonferroni) compared to WT mice, n = 60 cells / group (3 experiments).

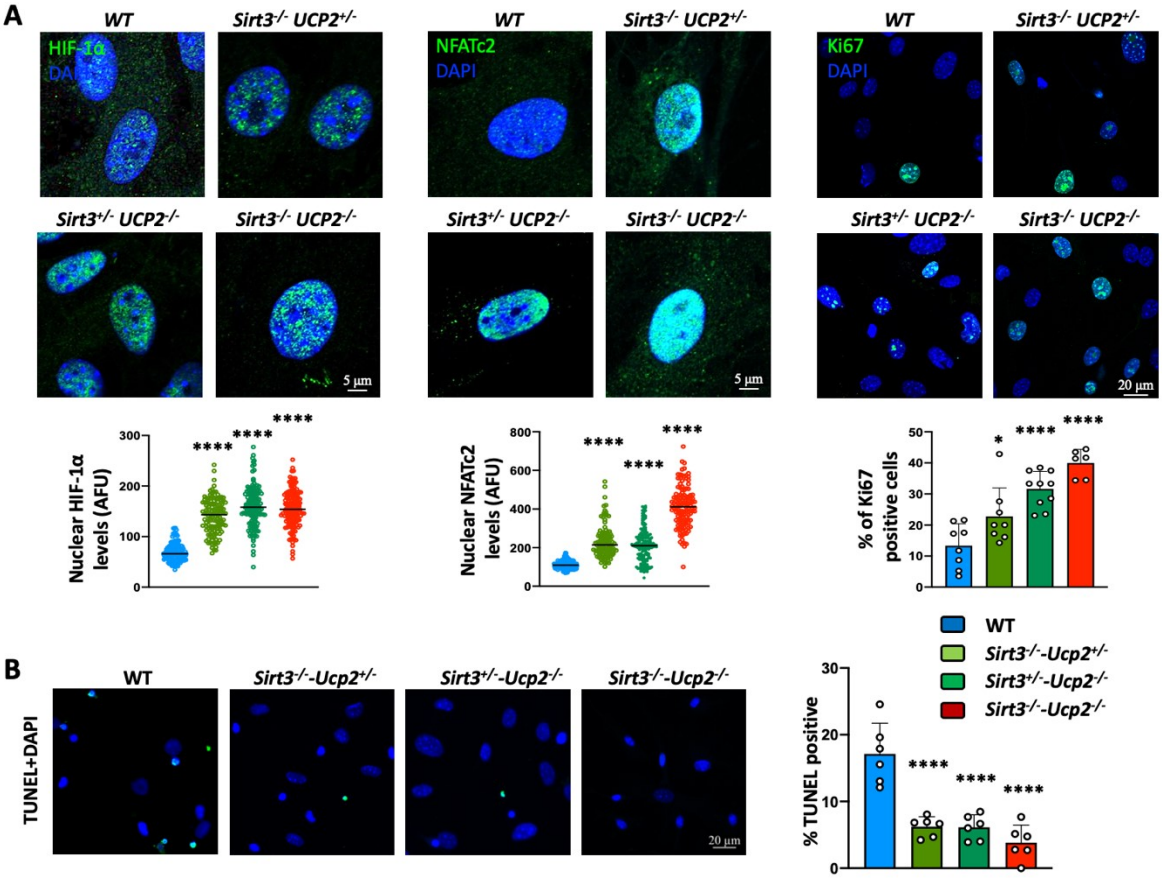
A
WT
Sirt3-/- UCP2+/-
HIF-1α
DAPI
NFATc2
Ki67
Sirt3+/- UCP2-/-
Sirt3-/- UCP2-/-
5 μm
20 μm
Nuclear HIF-1α levels (AFU)
Nuclear NFATc2 levels (AFU)
% of Ki67 positive cells
****
*
B
TUNEL+DAPI
Sirt3-/--Ucp2+/-
Sirt3+/--Ucp2-/-
Sirt3-/--Ucp2-/-
% TUNEL positive

Figure 2. 13. Proliferative and anti-apoptotic phenotype in cultured PASMCs from mice heterozygote or homozygote to the loss of both Sirt3 and Ucp2.

A) Increased intranuclear levels of HIF1α, NFATc2 and Ki67 in PASMCs from mice lacking *Sirt3* and *Ucp2* compared to PASMCs from WT mice. *p=0.0377, ****p<0.0001 (Bonferroni) compared to the WT PASMCs, following one-way ANOVA, n=~150 cells/group (HIF1α and NFATc2), n=~240 cells/group (Ki67) (from 3 mice/group). **B)** Increased resistance to apoptosis (less TUNEL-positive PASMCs) in response to serum starvation for 48 hours is shown in PASMCs from mice lacking *Sirt3* and *Ucp2* compared to PASMCs from WT mice. ****p<0.0001 (Bonferroni) compared to the WT PASMCs, following one-way ANOVA, n=~240 cells/group (from 3 mice/group). AFU indicates absolute fluorescence units; DAPI, 4',6-diamidino-2-phenylindole (nuclear stain); HIF1α, hypoxia inducible factor 1 α; NFATc2, nuclear factor of activated T cells 2; PASMCs, pulmonary artery smooth muscle cells; sirt3, sirtuin3; TUNEL, terminal deoxynucleotidyl transferase-mediated dUTP-biotin nick-end labeling; Ucp2, uncoupling protein 2; and WT, wild type.

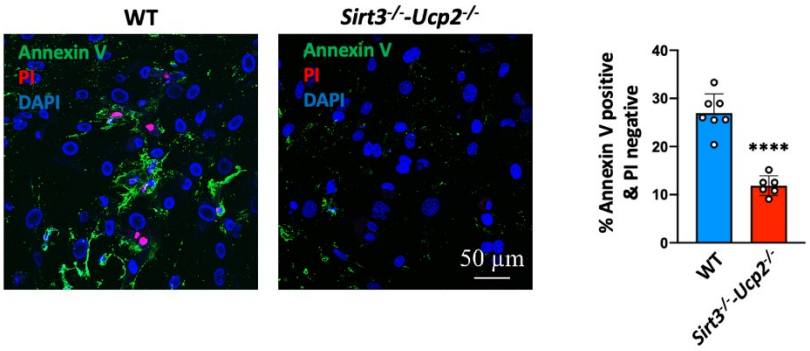

Figure 2. 14. Anti-apoptotic phenotype in cultured PASMCs from mice lacking both Sirt3 and Ucp2.

Annexin V / Propidium Iodide (PI) staining of PASMCs exposed to serum starvation for 48 hours shows decreased apoptosis in the Sirt3$^{-/-}$-Ucp2$^{-/-}$ compared to the WT PASMCs. The cells stained only for Annexin V (marking apoptosis) and not PI (which marks death) are counted to measure apoptosis (and not necrosis). ****$p<0.0001$ (Mann-Whitney U test) compared to the WT PASMCs, n = ~240 cells / group (3 experiments).

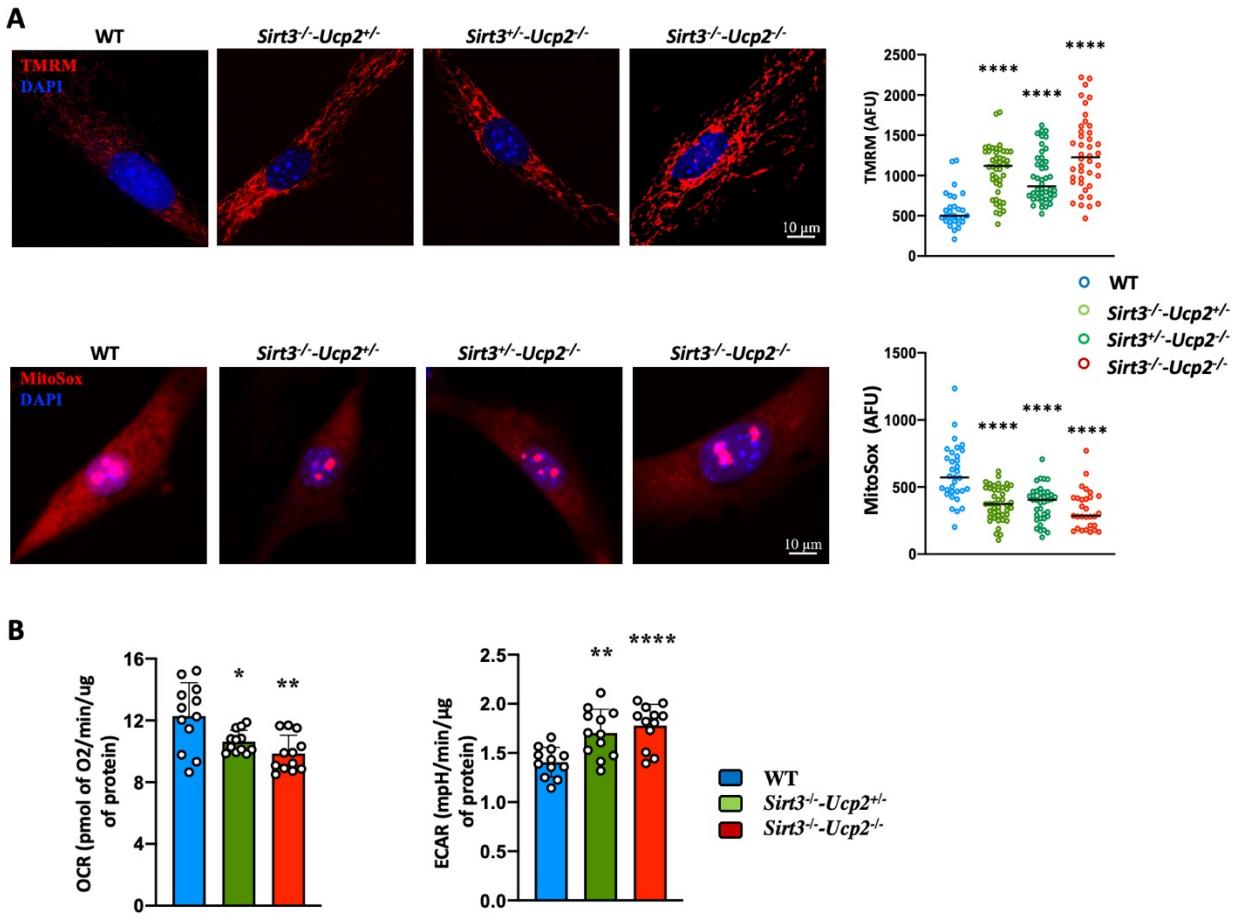
A
WT
Sirt3-/--Ucp2+/-
Sirt3+/--Ucp2-/-
Sirt3-/--Ucp2-/-
TMRM
DAPI
10 μm
TMRM (AFU)
2500
2000
1500
1000
500
0
****
****
****
WT
Sirt3-/--Ucp2+/-
Sirt3+/--Ucp2-/-
Sirt3-/--Ucp2-/-
MitoSox
DAPI
MitoSox (AFU)
1500
1000
500
0
****
****
****
B
OCR (pmol of O2/min/ug of protein)
16
12
8
4
0
*
**
ECAR (mpH/min/μg of protein)
2.5
2.0
1.5
1.0
0.5
0.0
**
****
WT
Sirt3-/--Ucp2+/-
Sirt3-/--Ucp2-/-

Figure 2. 15. Metabolic remodeling in PASMCs from mice lacking Sirt3 and Ucp2.

A) Staining with the mitochondrial tracer TMRM and MitoSox shows that PASMCs from *Sirt3*$^{-/-}$*-Ucp2*$^{+/-}$, *Sirt3*$^{+/-}$*-Ucp2*$^{-/-}$ and *Sirt3*$^{-/-}$*-Ucp2*$^{-/-}$ mice have higher mitochondrial membrane potential and lower production of mitochondrial derived ROS respectively, compared to mitochondrial from WT PASMCs. ****p<0.0001 (Mann-Whitney U test) compared to the WT PASMCs, n=50 cells/group (3 experiments). **B)** SEAHORSE measurements of respiration (oxygen consumption rate, OCR) and extracellular acidification rate (ECAR, indicative of glycolysis) show that PASMCs from *Sirt3*$^{-/-}$*-Ucp2*$^{+/-}$ and *Sirt3*$^{-/-}$*-Ucp2*$^{-/-}$ mice have suppressed OCR (i.e. suppressed mitochondrial function) and increased ECAR (i.e. secondary increase in glycolysis) compared to PASMCs from WT mice. For OCR: *p=0.0196, **p=0.0025; for ECAR: **p=0.0016, ****P<0.0001 (Bonferroni) compared to the WT PASMCs, following one-way ANOVA. n=12 measurements from 3 mice/group. AFU indicates absolute fluorescence units; DAPI, 4',6-diamidino-2-phenylindole (nuclear stain); ECAR, extracellular acidification rate; OCR, oxygen consumption rate; PASMCs, pulmonary artery smooth muscle cells; ROS, reactive oxygen species; sirt3, sirtuin3; TMRM, tetramethylrhodamine methyl ester; Ucp2, uncoupling protein 2; and WT, wild type.

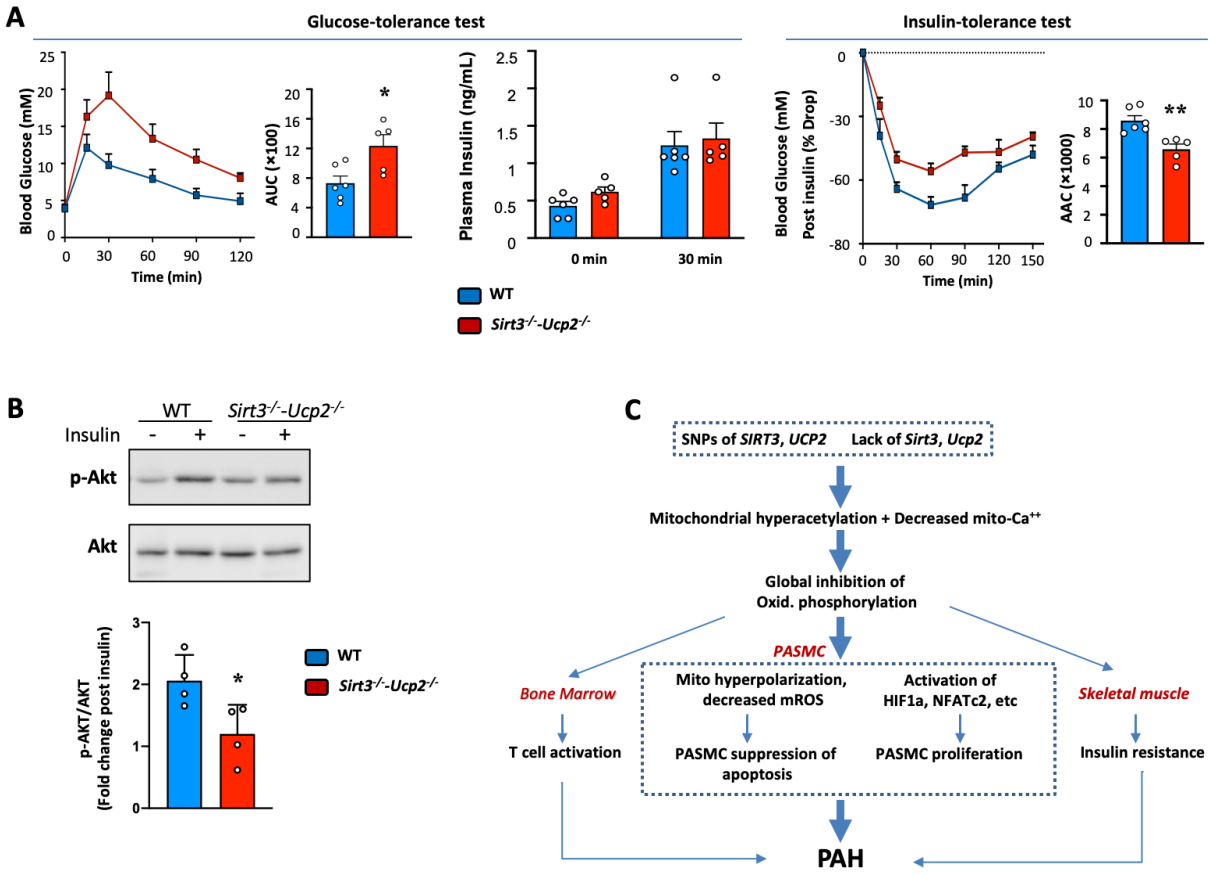
A
Glucose-tolerance test
Insulin-tolerance test
Blood Glucose (mM)
Time (min)
AUC (×100)
Plasma Insulin (ng/mL)
0 min
30 min
Blood Glucose (mM)
Post insulin (% Drop)
Time (min)
AAC (×1000)
WT
Sirt3-/--Ucp2-/-
B
WT
Sirt3-/--Ucp2-/-
Insulin
p-Akt
Akt
p-AKT/AKT
(Fold change post insulin)
WT
Sirt3-/--Ucp2-/-
C
SNPs of SIRT3, UCP2
Lack of Sirt3, Ucp2
Mitochondrial hyperacetylation + Decreased mito-Ca++
Global inhibition of
Oxid. phosphorylation
PASMC
Bone Marrow
Mito hyperpolarization,
decreased mROS
Activation of
HIF1a, NFATc2, etc
Skeletal muscle
T cell activation
PASMC suppression of
apoptosis
PASMC proliferation
Insulin resistance
PAH

Figure 2. 16. Insulin resistance in mice lacking Sirt3 and Ucp2 and an overall proposed mechanism for the diverse effects of SIRT3 and UCP2 loss in humans and mice with PAH.

A) Following starvation for 16 hours, the glucose levels in the blood *Sirt3*$^{-/-}$-Ucp2$^{-/-}$ are higher following glucose administration at time 0, compared to WT mice (glucose 2gr/Kg IP), but the blood insulin levels are not different (*glucose tolerance test*). The glucose levels decrease less after insulin administration (0.5U/Kg IP) following 6 hours starvation (the *insulin tolerance test* was performed 5 days after the glucose tolerance test), compared to WT mice. Areas under the curves (AUC) (for GTT test) and areas above the curves (AAC) (for ITT test) are shown in the bar graphs. Differences were determined by the use of an unpaired two-tailed Student's t test (AUC and AAC) or a two-way repeated measures ANOVA followed by Bonferroni post hoc analysis (GTT and ITT)[32]. *p=0.0173, ** p=0.0035 compared to WT mice, n=5-6 mice/group. **B)** Skeletal muscle (gastrocnemius) was removed at time 0 and 30 min during the insulin tolerance test. Fold increase in p-AKT/AKT shows that while the WT muscles showed the expected increase in Akt phosphorylation, the *Sirt3*$^{-/-}$-*Ucp2*$^{-/-}$ muscle did not show any change. A representative immunoblot is shown along with the mean data. *p=0.0331 (t test) compared to WT mice, n=4 mice/group. **C)** A proposed mechanism of how a primary mitochondrial abnormality can explain the presence of PAH, vascular inflammation and insulin resistance in human and mouse PAH (see discussion). AAC indicates areas above the curves; AUC, areas under the curves; GTT, glucose tolerance test; HIF1α, hypoxia inducible factor 1α; ITT, insulin tolerance test; mROS, mitochondrial reactive oxygen species; NFATc2, nuclear factor of activated T cells C2; PAH, pulmonary arterial hypertension; PASMC, pulmonary artery smooth muscle cell; Sirt3, sirtuin3; SNPs: single nucleotide polymorphisms; Ucp2, uncoupling protein 2; and WT, wild type.

Chapter three: A critical contribution of cardiac myofibroblasts and a predictive role of UCP2 SNPs in the RV decompensation in pulmonary hypertension

A critical contribution of cardiac myofibroblasts and a predictive role of UCP2 SNPs in the RV decompensation in pulmonary hypertension

Yongneng Zhang, Maria Areli Lorenzana-Carrillo, Saymon Tejay, Alois Haromy, Yongsheng Liu, Yuanyuan Zhao, Gopinath Sutendra, Evangelos D. Michelakis

Affiliations

Department of Medicine (Cardiology), Faculty of Medicine and Dentistry, University of Alberta, Edmonton, Alberta, Canada.

A version of this chapter will be submitted to a peer-reviewed journal as: Zhang Y, Lorenzana-Carrillo MA, Mohseni M, Tejay S, Haromy A, Liu Y, Zhao Y, Sutendra G, Michelakis ED. A critical contribution of cardiac myofibroblasts in RV failure and the role of UCP2 SNPs in the predisposition to RV decompensation in pulmonary arterial hypertension

3.1. Abstract

Introduction/hypothesis: The mechanism driving the transition from compensated (cRVH) to decompensated right ventricular hypertrophy (dRVH) in pulmonary hypertension (PHT) is unknown. We hypothesized that a transition from cardiac fibroblasts (cFB) to cardiac myofibroblasts (cMFB) underlies this mechanism. Decreased mitochondrial calcium (mCa^{++}) promotes cMFB differentiation (from cFB). Methylation of mCa^{++} uptake 1 (MICU1) and lack of UCP2 (uncoupling protein 2, a component of the mCa^{++} uniporter complex) decrease mCa^{++}, and therefore, activity of Krebs enzymes that produce diffusible metabolites, regulating epigenetic mechanisms that drive change in cell identity.

Methods/Results: In the monocrotaline-rat PHT model, we separated cRVH from dRVH based on strict hemodynamics (canulating the main pulmonary artery through the jugular vein) and Echo: dRVH had decreased cardiac output, increased right atrial pressure, decreased TAPSE and increased RV end diastolic diameter compared to cRVH. In isolated hearts, RV systolic pressure was lower in dRVH but in isolated cardiomyocytes (CM), contractility (sarcomere shortening) was not, pointing to a non-cardiomyocyte difference. The number of cMFB was not different between cRVH and Control, but dramatically increased in dRVH. Mitochondrial respiration was lower in dRVH cMFB than cRVH cFB. mCa^{++} was progressively decreased from Control to cRVH to dRVH c(M)FB, while it was not different in CM. The MICU1 methyltransferase (PRMT1) levels and methylation of immunoprecipitated MICU1 were increased but the expression of UCP2 was decreased from Control to cRVH to dRVH c(M)FB (but not CM). In human RV tissues (from autopsy, biopsy, n=15), the number of myofibroblasts increased mildly from Control to cRVH, but increased sharply in dRVH. The cytoplasmic PRMT1 level increases from CTRL to cRVH but did

not increase any further in dRVH while UCP2 continue to decrease from CTRL to cRVH to dRVH. In a cohort of 25 patients with PHT that had Echo and right heart Cath within 48 hours, carriers of the loss-of-function UCP2 SNP (rs659366) had decreased TAPSE compared to non-carriers that had similar mean PA pressure.

Conclusion: A change of cell identity (cFB to cMFB) in the RV may be the basis of cRVH to dRVH transition, rather than contractile failure of CM. UCP2 SNP may predict early dRVH, if confirmed in larger cohorts.

KEYWORDS: Myofibroblasts, Right Ventricular Hypertrophy, Right Ventricular Failure, UCP2, MICU1, Mitochondrial Calcium, Pulmonary Arterial Hypertension

3.2. Introduction

The main driver of mortality and morbidity in Pulmonary Arterial Hypertension (PAH) is the function of the right ventricle (RV) rather than the degree of rise in mean Pulmonary Artery Pressure (mPAP)[1,40]. In PAH, the compensated RV hypertrophy (RVH) stage (cRVH) is quite short, with decompensation occurring often in months[32], compared to the left ventricular hypertrophy where the compensation can last decades. Furthermore, between 2 patients with the same age/sex and PA pressures, one may have a much shorter cRVH stage and decompensate much faster than the other. What makes the transition from cRVH to dRVH and how one RV more prone to failure than another RV is unknown. The presumption so far in the field is that there is an energetic failure of cardiomyocytes along with collagen deposition and structural remodeling. The role of cardiac fibroblasts (cFB) and myofibroblasts (cMFB) is not understood in the transition from cRVH to dRVH.

In the left ventricle (LV) cMFB increase quickly post myocardial infarction, mostly by differentiation from cardiac fibroblasts (cFB) in order to limit the myocardial wound, via secretion of collagen and scar formation[44,72]. In contrast to cFB, cMFB express high levels of alpha-smooth muscle actin (α-SMA) that allows them to both contract and migrate to the wound site, but also increase the stiffness of the ventricle and compromise its function. cMFB increase in other cardiac pathologies as well, like LVH or diabetes, and can reach >30-40% of the cell population in the heart. Although this is a dynamic (and thus potentially reversible) process[44,72], excessive proliferation of cMFB can cause permanent scaring and severe cardiac dysfunction. There is accumulating evidence that differentiation and proliferation of cMFB can both be halted and even reversed, providing a rationale for therapeutic targeting of cMFB. Although this has not been tested

in the RV, it is very important because once dRVH ensues, any improvement in the pulmonary vascular remodeling and PA pressures (currently the focus of preclinical and clinical research), will be obsolete if the RV cannot recover, underlying the need for studies to understand the mechanisms promoting dRVH and cMFB regulation in the RV, which may be different than the LV since the two ventricles have different embryologic origin form different heart fields, and different metabolism and biochemistry in the adult heart.

Recently, a central role of mitochondrial calcium (mCa^{++}) was described in LV cMFB differentiation and activation. Mitochondria are important sinks of both cytosolic and endoplasmic reticulum Ca^{++}. They are the most negatively charged organelles in the cell with a membrane potential <-220mV, facilitating entry of the positively changed Ca^{++}. When mCa^{++} uptake is decreased, cytosolic Ca^{++} increases. A decreased mCa^{++} (which overall results in inhibition of mitochondria function as critical mitochondrial enzymes are very Ca^{++}-dependent) and the resultant increase in cytosolic Ca^{++} are both features of differentiating and proliferating cells. Indeed, when mCa^{++}uptake is reduced, it triggers cMFB activation: Pro-fibrotic stimulation (TGFβ or angiotensin II) of mouse cFB results in increased expression of mitochondrial calcium uptake 1 (MICU1), a major component of the mitochondrial calcium uniporter (MCU), the structure/function of which was recently elucidated. The MICU1 upregulation can reduce mCa^{++} uptake, since MICU1 controls the gating of MCU negatively[73]. In agreement, genetic deletion of *Mcu* results in increased cMFB differentiation in vivo following myocardial infarction. The regulatory role of decreased MCU activity in cMFB is multifactorial[74]. **First**, by decreasing the capacity of mitochondria to buffer local cytosolic Ca^{++}, more Ca^{++}, is available to enhance the myofibroblast gene program though Ca^{++}-dependent transcription factors like nuclear factor of

activated T cells (NFAT). **Second**, decreasing Ca^{++} entry into the mitochondria protects the cMFB against mitochondrial-dependent apoptosis in the stressful fibrotic environment because it results in an increase in the mitochondrial membrane potential, which regulates the opening of the mitochondria transition pore and the efflux of pro-apoptotic mediators. **Third**, altering mitochondrial matrix Ca^{++} concentration is a direct mechanism to regulate cellular metabolism: mCa^{++} is a regulator of PDH (pyruvate dehydrogenase) via activation of PDH phosphatase[75], and cMFB activation correlates with decreased PDH activity[76]. Further, fibrotic stimulation increases aerobic glycolytic flux and decreases glucose oxidation (and thus ATP production because of PDH inhibition)[77,78], decreasing the production of diffusible Krebs cycle metabolites that regulate the cMFB differentiation program via epigenetic mechanisms in the nucleus: e.g. Citrate is involved in histone acetylation via the production of acetyl-coA in the nucleus by the ATP-citrate lyase (ACL)[79], and α-ketoglutarate is a critical cofactor in the enzymes that regulate DNA demethylation[80], which like histone acetylation is a major epigenetic mechanism for the change in cell identity like the transformation of cFB to cMFB[81,82].

In addition to the MICU1, several other components of the MCU have recently been identified, including UCP2, allowing a revisit of MCU function models[72,83,84]. Asymmetric Arginine methylation of MICU1 by PRMT1, allows its interaction with UCP2 within the MCU, increasing the dependency to UCP2 for mCa^{++} uptake[84]. PRMT1 is increased in the failing heart and PRMT1 activity is known to be increased in hypoxia and reduced redox conditions (asymmetric dimethylarginine, ADMA, level is the measure of PRMT1 activity). We and others have shown that the cRVH is hypoxic due to incomplete angiogenesis, that does not keep up with the increase

in cardiomyocyte mass and the increased number of fibroblasts, potentially more than what happens to left ventricle hypertrophy (LVH)[43,85].

We previously showed that inflammatory cytokines like TNFα keeps increasing from normal, cRVH to dRVH rats[85] and are also increased in the serum of PAH patients. TNFα is known to inhibit UCP2 expression and thus decrease mCa^{++}. In addition, if UCP2 is genetically missing (eg, in KO mice or in germline loss of function SNPs in humans), dRVH will be promoted even more. We have published that genetic loss of UCP2 in mice promotes PAH and RV failure and Loss-of-function single nucleotide polymorphisms (SNPs) are both prevalent in PAH patients and associated with worse outcomes.

3.3. Methods

Our work with human clinical data and human tissues/blood as well as our work with rats/mice, was performed with permission from the University of Alberta Human Research Ethics Board (HREB) and Animal Care and Use Committee (ACUC), respectively.

Monocrotaline induced PAH rat model: Sprague Dawley rats were commercially purchased from the Charles River Laboratories, Canada. Rats were intraperitoneally injected with 60mg/kg monocrotaline (Sigma, C2401) at 8-week-old. Echocardiography was performed every week from 2weeks post injection. Based on the echo and terminal right heart catheterization criteria, rats were divided to CTRL (Normal RV), cRVH (usually in week3-4), dRVH groups (usually in week5-6).

***Ucp2* KO Model**: We generated a WT, UCP2 Heterozygous and UCP2 KO mice from a UCP2 heterozygous colony that was commercially available and previously published by our group[21,86].

***Ucp2* Mutant Genotyping**; Mice were genotyped by PCR using genomic DNA isolated from ear notching biopsies as described by Jackson Laboratories. The targeted *Ucp2* mutant mice have an insertion of a PGK-NEO cassette replacing exons 3-7 to create the larger mutant allele. Two sets of primers are used in combination to identify wildtype (forward primer sequence: GCG TTC TGG GTA CCA TCC TA, reverse primer sequence: GCT CTG AGC CCT TGG TGT AG) and mutant mice (forward primer sequence: CTT GGG TGG AGA GGC TAT TC, reverse primer sequence: AGG TGA GAT GAC AGG AGA TC). PCRs were carried out on a MasterCycler PCR Thermal Cycler (Eppendorf Cat # 5345) by direct amplification of the DNA from ear notching biopsies with the use of Phire Tissue Direct PCR Master Mix (ThermoFisher Scientific Cat # F170) following manufacturer's protocol. Amplifications were carried out as follows: at 94 °C for 5 min, followed by 10 cycles at 94 °C (20 sec), 65 °C (15 sec,-0.5°C per cycle decrease), 68 °C (10

sec); followed by 32 cycles at 98 °C (15 sec), 60 °C (15 sec), 72 °C (10 sec); finishing at 72 °C (2 min) and holding at 4 °C.

Cardiomyocyte and cardiac fibroblast isolation: Cardiomyocyte and cardiac fibroblast isolation and culture were done as previously described[87]. Briefly, adult cardiomyocytes were isolated from CTRL, cRVH and dRVH rats by digestion with type II collagenase (Worthington Biochemical Corpora-tion, LS004177) using a modified Langendorff perfusion apparatus (Harvard Apparatus, 73-4393). The cells were separated by centrifugation at 20g for 3 min (supernatant as nonmyocytes and pellet as enriched cardiomyocytes).

Cardiomyocyte culture

After isolation, cardiomyocytes were resuspended in a stopping buffer containing 2 mM ATP followed by centrifugation at 20g for 3 min and calcium reintroduction process by sequential resus-pension in a stopping buffer containing increasing concentrations of $CaCl_2$ at 100, 400, and 900 mM. Before plating, culture plates were coated with laminin (Sigma-Aldrich, 11243217001) for 2 hours at room temperature, and plating medium [minimum essential medium (MEM)] with Hanks' salts and 2 mM glutamine (Gibco, 11575032) supplemented with 10% fetal bovine serum (FBS) (Sigma-Aldrich, F1051), 10 mM 2,3-butanedione monoxime (BDM) (Sigma-Aldrich, B0753), 2 mM ATP (Sigma-Aldrich, A6419), and 1% penicilin/streptomycin/amphotericin (PSF) (Gibco, 15240-062) was prepared and kept in an incubator at 37°C with 2% CO2. Cells were plated for 1 hour, and the medium was changed to fresh culture medium containing MEM with Hanks' salts and 2 mM glutamine, 1% PSF, 0.1% bovine serum albumin (Sigma-Aldrich, A7906), 10 mM BDM, and 1% insulin transferrin selenium at final concentrations of 5 µg/ml for insulin, 5 µg/ml for transferrin, and 5 ng/ml for selenium (Sigma-Aldrich, I1884).

Cardiac (myo)fibroblast culture

Nonmyocytes were washed five times with Dulbecco's Modified Eagle Medium: Nutrient Mixture F12 (DMEM/F12) with 1 μM ascorbic acid and 10% FBS by centrifugation at 1500 rpm for 3 min. Fibroblasts were allowed to adhere for 2.5 hours at 37°C with 5% CO2, and then, fresh complete culture medium was added. The following day, the growth medium was replaced. When the cells become spindle shape (around day3), 2% FBS DMEM/F12 was replaced.

Confocal Imaging: Immunofluorescence staining was performed using a Zeiss LSM-710 model, equipped with an Airyscan module (Carl Zeiss). Cultured rat cardiac (myo)fibroblasts were grown on coverslips overnight. They were fixed with 2% PFA at 37℃ for 15 min, followed by permeabilization with Triton X-100 (0.25%) for 10 min. They were then treated with Image-iT FX Signal Enhancer (Thermo Fisher Scientific) for 30 min at room temperature and blocked for 1 h with 10% serum from the host of the secondary antibody. Cells were incubated with the primary antibodies overnight at 4℃. The following day, incubation with the secondary antibodies was performed for 1h at room temperature in the dark. Finally, they were counterstained with 1 μM DAPI (Molecular Probes, Oregon, USA) at room temperature for 10 min, prior to mounting in ProLong Glass (Thermo Fisher Scientific). Rat right ventricles were embedded in OCT compound and stored in -80℃ freezer for frozen section. Tissue slices (5 μm thickness) from right ventricles were processed and stained similar to cultured cells. Antibodies used were alpha smooth muscle actin (α-SMA) (Abcam, ab5694), Vimentin (Abcam, ab20346), Ki67 (Abcam, ab16667), PRMT1 (Cell Signaling, 2449S), ADMA (Cell Signaling, 13522S), MICU1 (Sigma Aldrich, HPA037480) and UCP2 (Cell Signaling, 89326S). All antibodies used for immunofluorescence were diluted in 1:100 and all secondary antibodies in 1:1000.

Mitochondrial respiration measurements: Oxygen consumption rates (OCR) was assessed using a Seahorse XF24 Extracellular Flux Analyzer (Agilent, Santa Clara, CA, USA) according to

the manufacturer's instructions. Rat cardiomyocytes and cardiac (myo)fibroblasts were seeded and cultured overnight in Seahorse XF-24 plates at a density of $5*10^3$ cardiomyocytes and $4*10^4$ cardiac fibroblasts per well. The next day, plating medium was removed and replaced with bicarbonate-free Seahorse XF Base medium without phenol red (Agilent) supplemented with 5.5 mM glucose. Following incubation of the cells in the CO2-free incubator for 1 h, cells were placed in the Seahorse Analyzer. OCR was calculated using 3 min mix and 3 min measure cycles. After the run, cells were washed with PBS and lysed in 100 µl per well of RIPA buffer (supplemented with protease inhibitors) for 30 min at 4℃ with constant agitation. Protein concentration was measured with a BCA assay and used to normalize the OCR values.

RNA isolation and qRT-PCR: mRNA was isolated using Qiazol (Qiagen). mRNA isolated from lung were added to a microwell plate with TaqMan probes and reagents. Quantitative RT-PCR was performed using TaqMan RNA-to-CT 1-Step Kit (Applied Biosystems 4392938), and beta-2-Microglobulin was used as a housekeeping gene. Primers were purchased from Thermo Fisher Scientific (*Ucp2* Rn01754856_m1).

Immunoblots: Tissues were collected and granulated on dry ice and lysed in ice-cold RIPA buffer via sonication with 10 quick pulses using a handheld homogenizer (VWR, PA, USA). Cardiomyocytes and cardiac (myo)fibroblasts cells were collected and lysed in ice-cold RIPA buffer for 30 min with vortexing every 10 min.Samples were then spun down at 10,000 rpm for 25 min in a tabletop centrifuge (Eppendorf AG, Hamburg, Germany). After centrifugation, the supernatant was collected. Protein concentration was quantified with a BCA kit (Thermo Fisher Scientific, Waltham, MA, USA) and measured on a SpectraMax iD3 plate reader (Molecular Devices, San Jose, CA, USA). Samples were then diluted to a final concentration of 1 µg / µl in RIPA buffer and 2x Laemmli Sample Buffer (Sigma-Aldrich). Finally, they were boiled at 95℃

for 5 min. All samples were loaded on SDS-PAGE polyacrylamide gels. Proteins were then transferred onto 0.45 nm pore nitrocellulose membranes using a Trans-blot Turbo transfer system (Bio Rad, Hercules, CA, USA) according to the manufacturer's instructions. After transferring, membranes were incubated with Ponceau S (Thermo Fisher Scientific) to verify efficient transferring of the proteins. Membranes were then washed with TBST and blocked with 5% BSA in TBST for 1 h at room temperature. Membranes were then incubated with the primary antibody in 1% BSA in TBST overnight at 4 ℃ with gentle rotation. The following day, membranes were washed with TBST and incubated with the appropriate HRP-conjugated secondary antibodies (Cell Signaling Technology, Danvers, MA, USA). Proteins were detected after incubation of the membranes with ECL buffer (Thermo Fisher Scientific) and visualized on a ChemiDoc imaging system (Bio-Rad). Antibodies and dilutions: PRMT1 (Cell Signaling, 2449S) 1:1000, ADMA (Cell Signaling, 13522S) 1:1000, MICU1 (Sigma Aldrich, HPA037480) 1:1000, MCU (Cell Signaling, 14997S) 1:1000, UCP2 (Cell Signaling, 89326S) 1:1000, VDAC ½ (Proteintech, 10866-1-AP) and β-Actin (Santa Cruz sc81178) 1:4,000.

Immunoprecipitation: Co-immunoprecipitations were done using the Dynabeads Co-IP kit (Thermofisher 14321D), Dynabeads ProteinA (Thermofisher 10002D), and Pierce IP lysis buffer (Thermofisher 87787) as per manufacturer's recommendations. Briefly, (myo)fibroblast mitochondrial was isolated by using Mitochondria Isolation Kit (Abcam) according to the manufacturer's instructions. Mitochondria was lysed with IP buffer. 50 mg equivalent of cell pellet volume (lysed in 500 µL of IP buffer) was added to 1 µg of antibody or the appropriate IgG isotype control antibody conjugated to beads and incubated at 4℃ rotating overnight. Beads were then washed, eluted using a pH 2.6 0.2 M glycine solution and neutralized with equal volume of 20 mM Tris pH 8, and boiled in 4x Laemmli buffer (Biorad).

Imaging of Mitochondrial Ca2+ Concentration (mCa^{++}): Mitochondrial Ca2+ concentration was measured by using Rhod-2 AM. Cells were incubated with DMEM/F12 media with 5 μM Rhod-2 AM for 30min at 37˚C, followed by an incubation with serum-free DMEM/F12 medium with 200 nM MitoTracker Green to detect the localization of mitochondria for another 30min. Then a confocal fluorescence microscope (Carl Zeiss) was used to evaluate the $mCa2^{++}$ levels. Rhod-2 was excited at 514 nm, and emission was monitored at 530-580 nm. MitoTracker Green was excited at 488 nm, and emission was monitored at 505-535 nm.

Echocardiography: Rats were anesthetized with isoflurane and maintained a heart rate of 300-400 beats per minutes and the Vevo 3100 High Resolution Imaging System (VisualSonics, Toronto, Canada) was used. Right ventricular thickness, right ventricular end-diastolic diameter and tricuspid annular plane systolic excursion (TAPSE) were recorded in the M-Mode. TAPSE was calculated by measuring the vertical movement of the tricuspid annulus between end-diastole and end-systole in the four chamber view, reflecting the longitudinal contraction of the RV. Cardiac output (CO) was calculated after determining the pulmonary artery diameter (PAD), pulmonary artery velocity time integral (PAVTI), and heart rate (HR) using the formula: $CO = 7.85 \times PAD^2 \times PAVTI \times HR/10{,}000$. Images with heart rate < 300 were excluded from the analysis.

Hemodynamic Measurements: Rats were initially anesthetized with 3%–4% isoflurane and maintained with 2% during procedures. A Millar catheter (microtip, 1.4F, Millar Instruments) was advanced through the jugular vein in closed-chest animals into right atrium (RA), RV and PA by guiding with a modified plastic sheath (curved). RA pressure, RV pressure and mean PA pressure (mPAP) were recorded (Power Lab, with Chart software 5.4, ADInstruments).

Mass Spectrometry: cardiomyocytes and (myo)fibroblasts were cultured in triplicates in 60 mm dishes overnight. c(M)FB were treated with 17.5mM C-13 glucose in no-phenol red, no-glucose

DMEM for 12 h, and CM were treated with 5mM C-13 Lactate for 2h. Then cells were washed and scraped in 1 mL of cold PBS solution, followed by centrifugation at 550 g for 5 min at 4°C. Cell pellets were re-suspended in an ice-cold mixture of methanol and ddH2O (80:20 v/v) containing a Succinic Acid-d6 internal standard (C/D/N Isotopes, Quebec, Canada). Samples were periodically vortexed, then sonicated (10 pulses, 50% intensity) and centrifuged at 13,000 rpm for 10 min at 4oC. Supernatants were collected, and the extraction procedure was repeated one more time. The combined supernatants containing metabolites were transferred to a new set of tubes and dried using a SpeedVac vacuum concentrator (Thermo Fisher Scientific). For extracting metabolites in supernatants, 200ul c(M)FB supernatants were collected and mixed with 800ul methanol and the following steps are the same as cell metabolites extraction. The dried metabolites were resuspended in 100 uL of LC/MS-grade water/acetonitrile (60:40 v/v) (Fisher Scientific) before Mass Spec analysis. The extracts from supernatant were diluted in water/acetonitrile (60:40, v/v) 10 times before HPLC/MS analysis. Standard and sample solutions were analyzed using an Aria MX HPLC system (Thermo Fisher Scientific) coupled to Orbitrap Elite Mass spectrometer (Thermo Fisher Scientific). The Xcalibur software v. 2.2 (Thermo Fisher Scientific) was used for data acquisition and analysis. For the determination of Lactate and TCA cycle metabolites, a ten-point calibration curve of target compounds with a concentration range from 0.005 mg/mL to 25 mg/mL was constructed based on the peak area ratio of the target compounds/internal standard vs. the target compounds concentration. The target compounds concentration was extrapolated from this calibration curve.

Isolated RV Langendorff Perfusion (Ex-vivo): Rats were anesthetized with isoflurane. A midline sternotomy was performed, and within 1 minute, the heart was isolated and the aorta was cannulated and perfused with Krebs' buffer (NaCl 118.5mM, $NaHCO_3$ 25mM, KCl 4.7mM,

$MgSO_4$ 1.2mM, KH_2PO_4 1.2mM, $CaCl_2$ 1.4mM, Glucose 5.5mM) at 12 to 13 ml/min. The hearts had a mean intrinsic rate of 180 to 200 bpm. A pacemaker was connected to the myocardium with a pacing rate at 300/min. A 0.03 cm^3 latex balloon (Harvard Apparatus, Saint-Laurent, Quebec, Canada) filled with water and attached to a pressure transducer (Cobe, Richmond Hill, Ontario, Canada) was placed in the RV via the right atrium, and pressure traces were sampled at a rate of 1000 Hz by PowerLab. Pressure readings were converted into first-derivative traces and were analyzed with Chart 8 software (ADInstruments Inc, Colo- rado Springs, Colo).

Assessment of cell contractility: Shortening of sarcomere was assessed by a video-based edge-detection system (IonOptix, Milton, MA, USA). Briefly, ventricular myocytes were plated on a round cover glass (25mm) coated with laminin. After 2 hours incubation, glue the cover glass to an experimental chamber with a pair of electrodes placed inside and perfused with Krebs' buffer (same as EX-vivo) at 1 ml/min. Cells were stimulated with 10 volts at a frequency of 2 Hz (1msec duration) using a field stimulator. The real trace of sarcomere shortening, relaxed sarcomere length (relaxed length, RL) and shortest sarcomere length during the contraction (contracted length, CL) were recorded. The sarcomere shortening was calculated using the formula: The percent shortening = (RL-CL)/RL x100%.

Statistical analysis: All statistical analyses performed on STATA (StataCorp LLC, Texas, USA). Values are expressed as mean ± SEM. The use of parametric or non-parametric tests was decided after assessment of normal distribution of the values by the Shapiro-Wilk normality test. For parametric tests, we used two-tailed, unpaired Student's t test to assess statistical significance between two groups, and multiple groups were compared using one-way analysis of variance (ANOVA) or two-way repeated measures ANOVA followed by a Bonferroni post hoc analysis. For non-parametric tests, Mann-Whitney U test was used for comparisons between two groups

and Kruskal-Wallis test was used to compare multiple groups. Non-parametric correlation analysis of the clinical data was performed using the Spearman correlation co-efficient. Significance for all statistical testing was considered to be $p < 0.05$.

3.4. Results

We established a model in which we could study the hemodynamics of the transition between normal RV, cRVH and dRVH in a rat model of PAH due to monocrotaline. We studied rats before monocrotaline injection, 3 weeks, and 5 weeks post monocrotaline injection. And we measured hemodynamic and RV function with right heart catheterization (internal jugular canulation and advance of Millar catheter tip into the main pulmonary artery), as well as echocardiography. This model allows us to record mean PA pressure (i.e, the severity of PAH), RVSP (i.e, the contractility of the right ventricle), RA pressure and cardiac output (i.e, the stage of heart failure), RV free wall thickness, RV end-diastolic diameter (RVEDD), and tricuspid annular plane systolic excursion (TAPSE) (ie, the structural and functional RV remodeling). We defined cRVH as a state of increased mean PA pressure and RVSP, but preserved cardiac output and not severally increased RA pressure. cRVH also has increased RV free wall thickness but not severally increased RVEDD. In contrast, compared to cRVH, dRVH is characterized by a still high mean PA pressure but a drop in RVSP, cardiac output and TAPSE, as well as a further increase in RA pressure and RVEDD (**Figure 3. 1A, B, C, D**.). All the RVs and tissues labeled cRVH or dRVH came from rats that strictly fulfilled these hemodynamic criteria. This offers a very accurate distinction between the three RV stages, allowing us to study cells of these ventricles in an accurate manner as one of our goals is to discover the mechanism of the transition from cRVH to dRVH.

In order to study the RV contractility in ex-vivo, we used the Langendorff perfusion system in which we placed a balloon into the right ventricle, and we measured the contractility with and without a myocadiac pacemaker. Although we did measure the contractility without the presence of a pacemaker for the first 2 minutes, and with a pacemaker beyond this point because at that time we often observe arrhythmias that are compromising our recordings. As expected, the RV contractility decreased from cRVH to dRVH **(Fig. 3. 1E)**. However, when we isolated the cardiomyocytes to study the contractility in vitro (measured by sarcomere shortening), we found no significant differences among the three groups **(Fig. 3. 1F)**. This suggests that the differences of contractility in vitro and ex vivo hearts (as well as in vivo) may be due to factors external to cardiomyocytes.

Then we isolated RV cardiomyocytes and (myo)fibroblasts. We identified myofibroblasts (cMFB) as cells expressing both vimentin and α-SMA and we found that the number of myofibroblasts is not different between normal RV and cRVH, but it is dramatically increased in dRVH **(Fig. 3. 2A, B)**. We also found that cMFB expressed specifically high ki67, in keeping with their high proliferative nature **(Fig. 3. 2C)**.

We then studied whether there is a difference in mitochondrial function among the 3 different RV conditions using the Seahorse setup. We found that the decompensated cMFB had decrease baseline, ATP-linked and maximal respiration, compared to normal RV and cRVH cFB **(Fig. 3. 2D)**. But an opposite pattern of basal respiration was found in CM, where the decompensated CM had increased oxygen consumption rates (OCR) **(Fig. 3. 2E)**. The OCR is a reflection of the overall mitochondrial function, particularly the production of NADH and FADH from the Krebs cycle,

which is used in Electron Transport Chain to generate ATP along with oxygen. The production of NADH and FADH depends on the activity of many enzymes that are very much mCa^{++} dependent.

We measured mCa^{++} in c(M)FB from the three groups. We found decreasing mCa^{++} from normal to cRVH and a further decrease to dRVH **(Fig. 3. 3A)**. To investigate the basis of this difference, we first measure the levels of the mCa^{++} uniporter MCU and its two main components, MICU1 and UCP2. In addition, because the function of the MICU1 has been shown to depend on its methylation by the methyltransferase PRMT1**,** we also measured the expression of PRMT1, the methylation of whole cells using ADMA, as well as the methylation of immunoprecipitated MICU1.

In RV tissues, we found that the PRMT1 levels are increased from normal to cRVH cFB, and are further increased in dRVH cMFB (**Fig. 3. 3B**). The ADMA levels are also increased from normal RV to cRVH to dRVH c(M)FB (**Fig. 3. 4A**). To better visualize the location of cytoplasmic PRMT1 and ADMA (which should colocalize with MICU1 in mitochondria), we stained for PRMT1 and ADMA in cultured c(M)FB from normal RV, cRVH and dRVH. We found that the cytoplasmic PRMT1 and ADMA are increased from normal RV to cRVH to dRVH **(Fig. 3. 3C, 3. 4B)**. MICU1staining shows a mitochondrial pattern **(Fib 3. 4C)**. The ADMA is increased in dRVH cMFB compared with normal RV and cRVH cFB, and so is the ratio of aDMA (50kd)/MICU1 (ie, MICU methylation) **(Fig. 3. 5A)**. To measure the methylation status of MICU1 specifically, we isolated the mitochondria from c(M)FB, performed a MICU1 immunoprecipitation, and measured the level of ADMA and MICU1. We found the ratio of ADMA/MICU is increased from normal RV to cRVH to dRVH. More importantly, the ADMA level which indicates methylated MICU1

is increased in dRVH cMFB compared to normal RV and cRVH cFB **(Fig. 3. 5B)**. There was no difference in MCU protein level in c(M)FB among the three groups **(Fig. 3. 5C)**. Lastly, no difference in MICU1 methylation was found in CM among the three groups **(Fig. 3. 6A)**.

UCP2 level is decreased in dRVH RV tissue compared with cRVH and normal RV**(Fig. 3. 7A)**. The UCP2 level is also decreasing in c(M)FB from normal RV to cRVH to dRVH, but not in CM. To determine the role of UCP2 in the regulation of mCa^{++} independent of M1CU1 methylation, we measured mCa^{++} level in cFB from wild-type, UCP2 heterozygote and KO mice **(Fig. 3. 8A)**. We found a gene dose-dependent decrease in mCa^{++} as UCP2 levels decrease **(Fig. 3. 8B)**. These data together suggest that the reason for the progressive loss of mCa^{++} from normal to cRVH to dRVH may be an increase of MICU1 methylation combined with a progressive loss of UCP2 in cMFB. This can explain the increased number of cMFB from cRVH to dRVH.

The classic inducer of cMFB is TGFβ. The TGFβ signaling is overall abnormal in PAH patients due to mutations of BMPRII receptors and other factors. In addition, we know that patients with PAH have a very inflammatory phenotype, and we have previously shown that in the transition from cRVH to dRVH, there is an increase in the cytokine TNFα[85] and the same is true for patients with PAH compared to controls. TNFα has been shown to decrease the expression of UCP2[88]. Therefore, we studied whether TGFβ and TNFα have an additive effect in the decrease of the mCa^{++} in the right ventricular fibroblasts. The data support this view and are shown in **Figure 3. 9A, B**. Compared with vehicle-treated, cFB treated with TGFβ alone have increased α-SMA and decreased mCa^{++}. However, cFB treated with TGFβ and TNFα show further increased α -SMA and decreased mCa^{++}.

How does the change in mCa^{++} affect the transformation from cFB to cMFB? This change in cell identity is driven by epigenetic mechanisms, particularly histone acetylation[89]. TGF-β activating myofibroblast is accompanied by a decrease in total H3 acetylation[82]. The decrease in mCa^{++} causes a decrease in diffusible metabolites, like citrate (which is involved in histone acetylation via the production of acetyl-coA in the nucleus by the ATP-citrate ligase[79]). We measured citrate with mass spectrometry and found that citrate is decreased in dRVH cMFB compared with normal RV and cRVH cFB **(Figure 3. 10A)**.

We were intrigued by the disassociation between the mitochondrial function of the c(M)FB versus the cardiomyocytes during the progression of RV failure. We speculated that the two cells may communicate in a paracrine manner, in an attempt to harmonize energy homeostasis in a manner similar to what has been described between neurons and glial cells[90,91]. It is possible that the cardiomyocytes may use the glycolysis by-product lactate as a fuel to further support ATP synthesis. The decrease in OCR in myofibroblasts is typically associated with an increase in glycolysis and therefore an increase in lactate, as it has been very well described in cancer (the Warburg effect). Therefore, we speculated that the lactate produced by cMFB could be uptaken by cardiomyocytes, something that could explain the "paradoxical" increase in OCR that we found in CMs **(Figure. 3. 2E)**. Therefore, we first measured intracellular and supernatant lactate levels from decompensated cMFB and we found them to be increased **(Figure 3. 10B)**. Then we measured the levels of two enzymes: LDHA which preferentially converts pyruvate to lactate and LDHB which preferentially converts lactate to pyruvate; as well as two transporters of lactate (MCT4 for export and MCT1 is for import of lactate) **(Figure 3. 10C)**. The data shown in **Figure 3. 10D, E** are in

support of this symbiotic relationship between cMFB and cardiomyocytes. We found the LDHA increased from normal RV to cRVH to dRVH, and the ratio of LDHA/LDHB sharply increased in dRVH cMFB. Moreover, dRVH cMFB have decreased MCT1 but increased MCT4 compared with normal RV and cRVH cFB (**Figure 3. 10D**). In contrast, dRVH and cRVH CM show increased MCT1 compared with normal CM (**Figure 3. 10E**).

To show that lactate can be used in CM as a fuel to generate Krebs cycle intermediates and ATP production**,** we used C-13 labeled lactate to treat CM and found that CM can uptake C-13 lactate and generate C-13 labeled metabolites (Fumarate and Malate, etc.) **(Figure3. 10F, G)**. The proposed mechanism is shown in **Figure 3. 10H**.

We then studied human RV tissues obtained through autopsy, biopsy or transplantation. RV tissues were identified as cRVH versus dRVH based on TAPSE (>2.1cm for cRVH, <2cm for dRVH) and WHO functional class (I-II for cRVH, III-IV for dRVH). This distinction was supported by the cardiac index which were significant lower in the dRVH patients, shown in **Table 3.1** along with relevant clinical data. We found that the number of myofibroblasts increased mildly from Control (CTRL) to cRVH, but increased sharply in dRVH **(Figure 3. 11A)**. We also found the cytoplasmic ADMA levels are increased from CTRL to cRVH to dRVH c(M)FB **(Figure 3. 11B)**. Interestingly, the cytoplasmic PRMT1 level increases from CTRL to cRVH (like in the rat model) but did not increase any further in dRVH **(Figure 3. 11C)** while UCP2 continue to decrease from CTRL to cRVH to dRVH (similar to the rat model) **(Figure 3. 12A)**. This suggests that the continue deterioration of the RV function may relate to a further decrease of UCP2. Although the decrease of UCP2 maybe secondary to cytokines, likes TNFa for example, it may also occur due

to the presence of loss of function UCP2 SNPS, like the rs659366 which has been shown to be associated with decreased expression of UCP2[28].

To address the role of this UCP SNP in vivo, we studied a cohort (n=25) of pulmonary hypertension (PHT) patients that underwent right heart catheterization and echocardiography both within 2 days from our pulmonary hypertension program. This cohort included patients with sPHT (thromboembolic PHT, COPD) or PAH (idiopathic or SSC related). In our clinic, we followed a standard guideline-directed medical therapy protocol, which means that all our PAH patients undergo the same treatment (they were all on ERA and PDE5 inhibitors and none on epoprostenol). In addition, blood from these patients was used to detect the presence of the UCP2 SNP using ddPCR as previously published[22,86]. We found that within patients with similar mean PA pressure, a decrease in TAPSE was associated with the presence of this loss of function UCP2 SNP **(Figure 3. 12B).** Although the sample size of this cohort is small, we believe that if this provocative mechanism is confirmed in a larger cohort, it could have significant clinical implications, predicting further RV failure in the UCP2 SNP carriers.

3.5. Discussion

Our work shows that cardiac myofibroblasts are activated during the transition from cRVH to dRVH. The decreased mCa^{++} due to MICU1 methylation in addition to UCP2 decrease is the potential mechanism of cMF activation. Furthermore, we showed that a UCP2 SNP is correlated with worse RV function in patients with PAH. Our work also showed for the first time a paracrine relationship between the cMFG and CM in the RV, in that the lactate secreted by cMFB can be imported to CM and used as fuel. The potential mechanism is shown in **Figure 3. 10H and 3. 12C**.

Our work questions the concept that RV heart failure is due to cardiomyocyte inotropic dysfunction as we found that the RV pressure from isolated dRVH heart is decreased compared to cRVH, while the contractility of dRVH CM is not different from cRVH CM. We found that the cell number of cMFB increased in dRVH compared with normal RV and cRVH. Moreover, the dRVH cMFB showed a proliferative and glycolytic phenotype. Therefore, considering the features of myofibroblasts, with collagen and cytokine production, contraction (which would result in RV diastolic dysfunction), we think the transformation of cFB into cMFB contributes to, or drives the transition from cRVH to dRVH. We propose that the therapeutical target of dRVH in PAH could be the changing the cell fate of cMFB or preventing the transformation of cFB to cMFB.

cFB differentiating into cMFB has been shown to depend on decreased mCa++, which decreases the activity of mitochondrial enzymes and the production of diffusible metabolites that regulate the epigenetic changes involved in the change of cell identity. Our work shows dRVH cMFB have decreased citrate which would promote decreased histone acetylation. This is in keeping with the theory that myofibroblast activation requires histone deacetylation-mediated gene repression[82,89]. Therefore, targeting this epigenetic change could inhibit the differentiation of cFB into cMFB. In addition, as we know that the TGFβ signaling pathway (SMAD 2/3/4) promotes the cFB differentiation into cMFB[92], using a drug that inhibits this pathway, for example, sotatercept[93], could be beneficial in preventing or delaying cMFB activation, as well as dRVH in PAH. Another component of MCU in regulating mCa^{++} is UCP2. Our work shows that PAH patients with a loss of function UCP2 SNP have worse RV function compared to those that don't have it. Our work offers a novel potential biomarker that could identify patients predisposed to earlier dRVH. There are advantages of this potential biomarker. First, it is a non-invasive method as genotyping can be

performed with blood samples. Second, this biomarker could “predict” the RV function in PAH patients, making the patients who predispose to earlier dRVH be considered for early combined therapies and referred to transplantation preferentially. This of course will be true only if this is proven in prospective, independent, and multicenter cohorts.

Another aspect of ours indicates that c(M)FB and CM have crosstalk in fuel communication, that is c(M)FB secrete lactate which is imported by CM and used as fuel. This phenomenon is more common in dRVH as the cMFB generate and secrete more lactate than normal cFB. However, we still need to know whether this effect is harmful to CM or not. This needs to be studied in the future. Nevertheless our work suggests that the interpretation of functional RV metabolic imaging (for example by FDG-PET, needs to be interpreted differently, considering that the majority of the signal may come from non-cardiomyocyte cells and may not directly reflect the energetic or metabolic status of the myocardium.

Table 3.1. Clinical information of human RV samples.

Category	Diagnosis	Age	Sex	RVSP (mmHg)	CI (L/min/m^2)	ERA/PDE5i	Epoprostenol
CTRL	Sudden death	43	F	N/A	N/A	N/A	N/A
CTRL	Sudden death	52	F	N/A	N/A	N/A	N/A
CTRL	Sudden death	29	M	N/A	N/A	N/A	N/A
CTRL	Sudden death	48	F	N/A	N/A	N/A	N/A
CTRL	Sudden death	49	F	N/A	N/A	N/A	N/A
cRVH	PHT (CHD)	29	M	35	2.54	no	no
cRVH	PHT (CHD)	30	F	42	3.00	no	no
cRVH	PHT (CHD)	32	F	78	3.00	no	no
cRVH	PHT (CHD)	30	F	19	3.70	no	no
cRVH	PHT (CHD)	28	F	53	2.57	no	no
dRVH	SSc-PAH	54	F	60	1.51	yes	no
dRVH	SSc-PAH	77	M	44	1.70	yes	no
dRVH	SSc-PAH	47	F	80	0.70	yes	yes
dRVH	SSc-PAH	53	F	110	1.96	yes	no
dRVH	IPAH	61	F	100	1.73	yes	no

SSc: systemic sclerosis; IPAH: Idiopathic pulmonary arterial hypertension; PHT(CHD): Pulmonary hypertension due to congenital heart disease; CI: cardiac index (L/min/m2); ERA: endothelin receptor antagonist; PDE5i: phosphodiesterase-5 inhibitor.

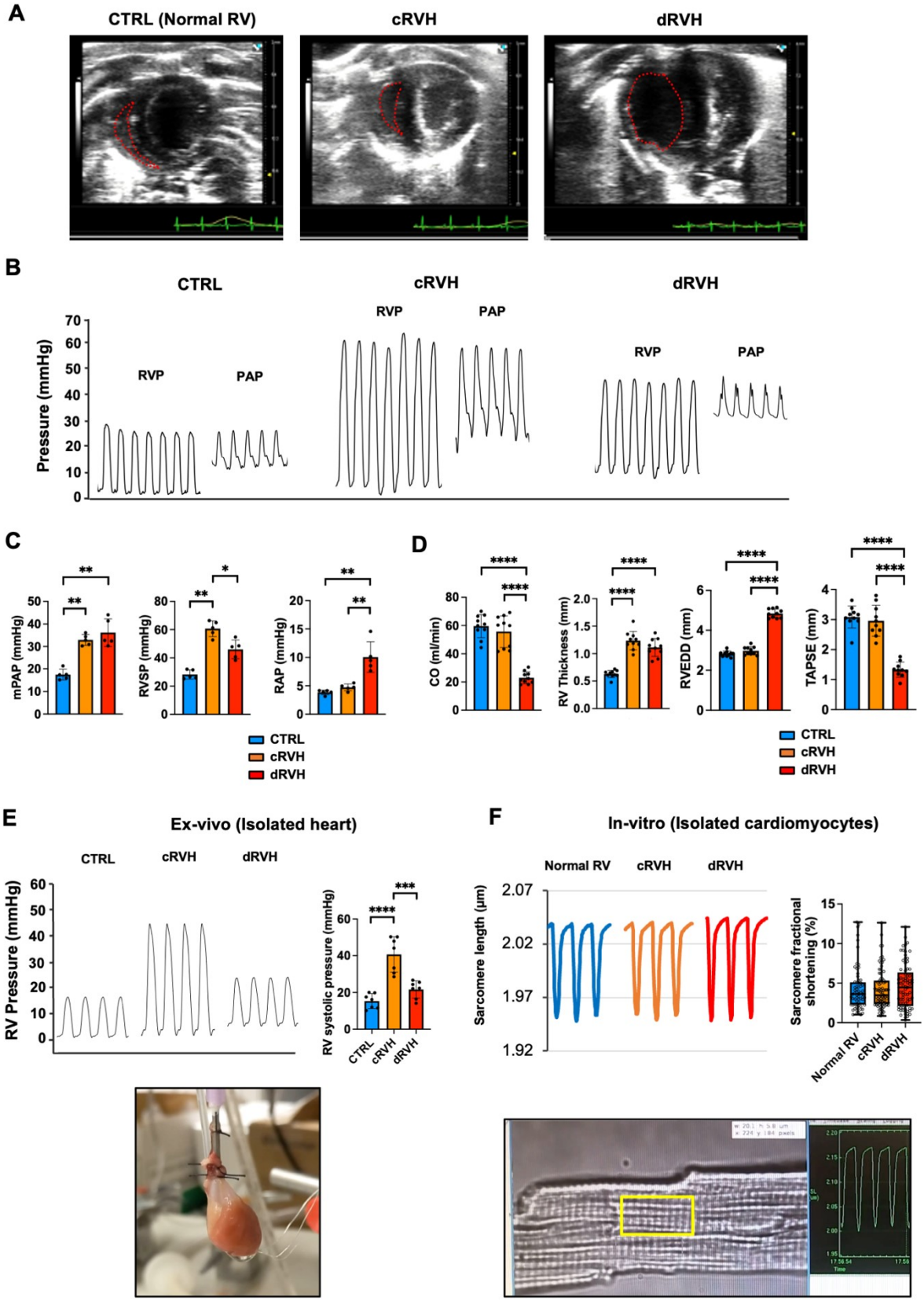
A
CTRL (Normal RV)
cRVH
dRVH
B
CTRL
cRVH
dRVH
RVP
PAP
Pressure (mmHg)
C
mPAP (mmHg)
RVSP (mmHg)
RAP (mmHg)
CTRL
cRVH
dRVH
D
CO (ml/min)
RV Thickness (mm)
RVEDD (mm)
TAPSE (mm)
CTRL
cRVH
dRVH
E
Ex-vivo (Isolated heart)
CTRL
cRVH
dRVH
RV Pressure (mmHg)
RV systolic pressure (mmHg)
F
In-vitro (Isolated cardiomyocytes)
Normal RV
cRVH
dRVH
Sarcomere length (µm)
Sarcomere fractional shortening (%)

Figure 3. 1. RV pressure is decreased in decompensated RV both in-vivo and ex-vivo, but cardiomyocyte contractility is not different among CTRL, cRVH and dRVH in rats.

A. Representative echocardiography pictures (short axis) show the size of RV chamber (red dotted line) in the three stages.

B. Representative tracings of RV and PA pressures in CTRL, cRVH and dRVH rats.

C. Several parameters are measured by close chest right heart catheterization (meanPAP, RVSP, RAP). Quantification values are expressed as mean ± SEM; n = 5 animals for each group. *P<0.05, **P<0.01.

D. Parameters are measured by echocardiography (cardiac output, RV free wall thickness, RVEDD, TAPSE). Quantification values are expressed as mean ± SEM; n = 10 animals for each group. ****P<0.0001.

E. Representative tracings and quantification of RV pressures in Ex-vivo (isolated heart) in CTRL, cRVH and dRVH rats. The picture below shows how the perfused isolated heart works, with a balloon inserted in RV (back) and pacemaker wires in the myocardium. Quantification values are expressed as mean ± SEM; n = 7 animals for each group. ***P<0.001. ****P<0.001.

F. Representative tracings of sarcomere length and quantification of RV cardiomyocyte contractility (showed as sarcomere shortening) in normal RV, cRVH and dRVH. Quantification values are expressed as median ± interquartile range (IQR); n = 6 animals for each group.

CTRL, control (without monocrotaline injection), cRVH, compensated right ventricular hypertrophy; dRVH, decompensated right ventricular hypertrophy; RVP, right ventricle pressure; PAP, pulmonary artery pressure; mPAP, mean PA pressure; RVSP: right ventricular systolic pressure; RAP, right atrium pressure; RVEDD, right ventricular end-diastolic diameter; TAPSE, tricuspid annular plane systolic excursion.

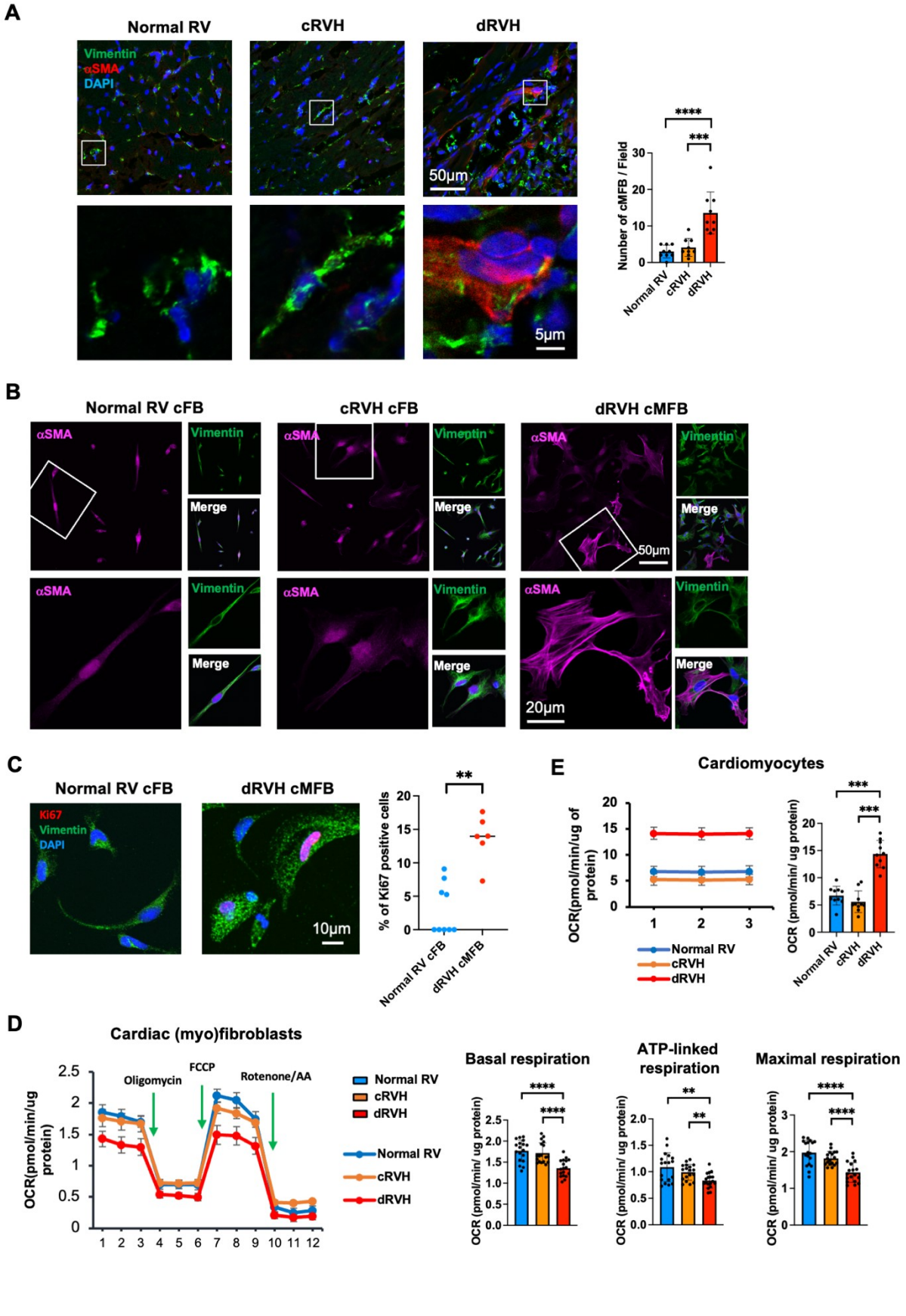
A
Normal RV
cRVH
dRVH
Vimentin
αSMA
DAPI
50μm
5μm
Number of cMFB / Field
Normal RV
cRVH
dRVH
B
Normal RV cFB
cRVH cFB
dRVH cMFB
αSMA
Vimentin
Merge
50μm
20μm
C
Normal RV cFB
dRVH cMFB
Ki67
Vimentin
DAPI
10μm
% of Ki67 positive cells
Normal RV cFB
dRVH cMFB
D
Cardiac (myo)fibroblasts
OCR(pmol/min/ug protein)
Oligomycin
FCCP
Rotenone/AA
Normal RV
cRVH
dRVH
Basal respiration
ATP-linked respiration
Maximal respiration
OCR (pmol/min/ ug protein)
E
Cardiomyocytes
OCR(pmol/min/ug of protein)
Normal RV
cRVH
dRVH
OCR (pmol/min/ ug protein)

Figure 3. 2. The cell number of myofibroblasts is increased in dRVH, and the dRVH myofibroblasts are more proliferative and glycolytic compared with normal RV and cRVH fibroblasts.

A. Confocal microscope shows the number of myofibroblasts (positive with both a-SMA and Vimentin) in right ventricle frozen sections from Control, cRVH and dRVH rats. Quantification values are expressed as mean ± SEM; n = 3 animals for each group. ***P < 0.001; ****P < 0.0001.

B. Confocal microscope shows the a-SMA pattern of cultured (myo)fibroblasts of normal RV, cRVH and dRVH.

C. Confocal microscope shows the ratio of Ki67 positive (with nuclear Ki67) cells in (myo)fibroblasts from normal RV and dRVH rats. Quantification values are expressed as mean ± SEM; n = 3 animals for each group. **P < 0.01.

D. Seahorse setup shows the oxygen consumption rate (OCR) in (myo)fibroblasts from normal RV, cRVH and dRVH rats. Quantification values are expressed as mean ± SEM; n = 3 animals for each group. Basal respiration is the OCR before adding drugs; ATP-linked respiration is the difference between basal OCR and OCR post Oligomycin. Maximal respiration is the OCR post FCCP. **P < 0.01; ****P < 0.0001.

E. Seahorse setup shows the oxygen consumption rate (OCR) in cardiomyocytes from normal RV, cRVH and dRVH rats. As the cell viability of cardiomyocytes drops quickly after basal respiration measurement, we only show the basal respiration data. Quantification values are expressed as mean ± SEM; n = 3 animals for each group. ***P < 0.0001.

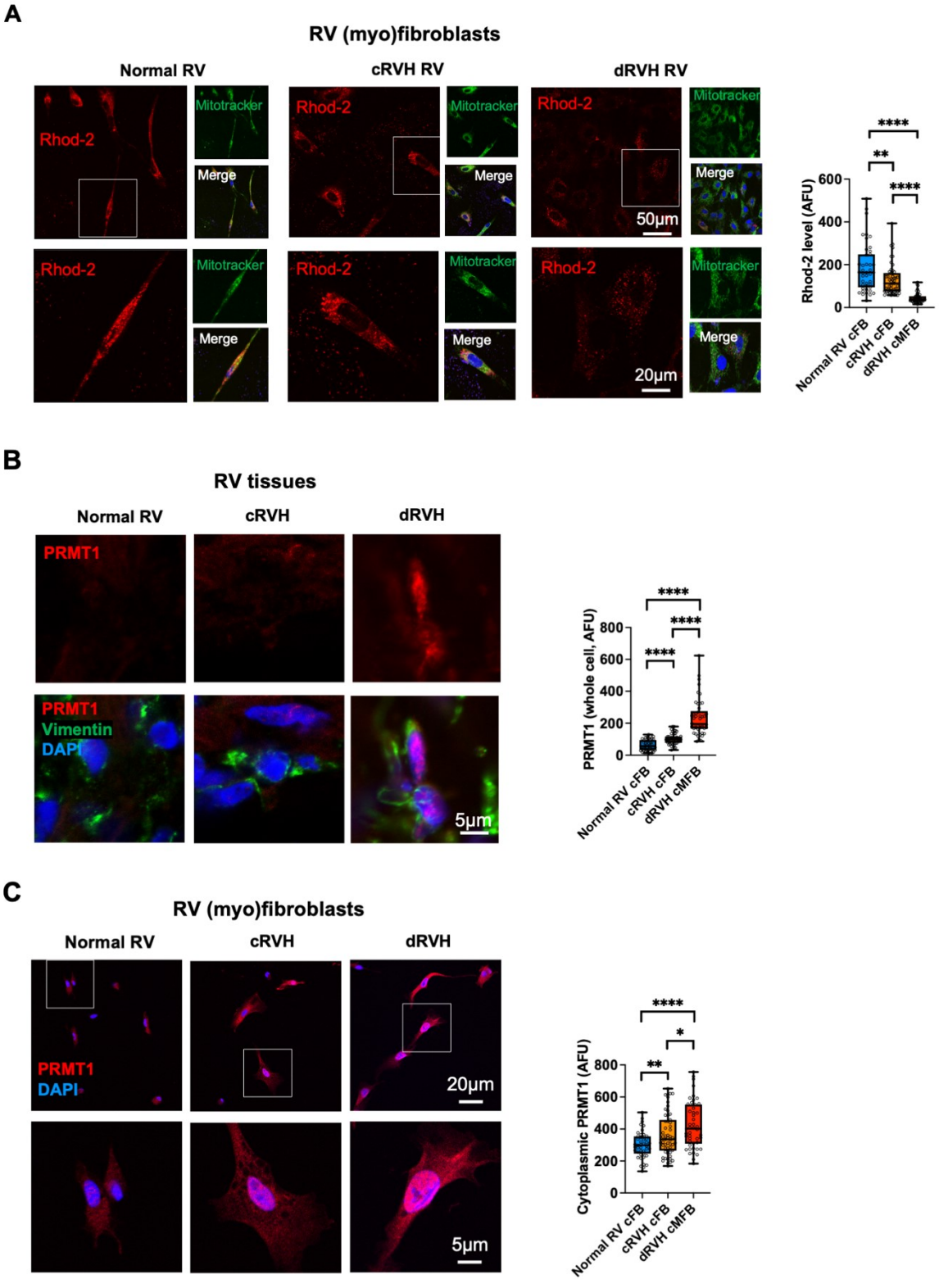
A
RV (myo)fibroblasts
Normal RV
cRVH RV
dRVH RV
Rhod-2
Mitotracker
Merge
50μm
20μm
Rhod-2 level (AFU)
Normal RV cFB
cRVH cFB
dRVH cMFB
B
RV tissues
Normal RV
cRVH
dRVH
PRMT1
Vimentin
DAPI
5μm
PRMT1 (whole cell, AFU)
C
RV (myo)fibroblasts
Normal RV
cRVH
dRVH
PRMT1
DAPI
20μm
5μm
Cytoplasmic PRMT1 (AFU)

Figure 3. 3. Mitochondrial calcium level is decreased, and the arginine methyltransferase is increased in dRVH myofibroblasts compared with normal RV and cRVH fibroblasts.

A. Confocal microscope shows the mitochondrial calcium level (Rhod-2 fluorescence level) in cultured (myo)fibroblasts from normal RV, cRVH and dRVH. Quantification values are expressed as median ± IQR; n = 50 cells from 3 animals for each group. **P < 0.01; ****P < 0.0001.

B. Confocal microscope shows the PRMT1 (i.e. arginine methyltransferase) level in (myo)fibroblasts (vimentin-positive cells) from right ventricle frozen sections of Control, cRVH and dRVH. Quantification values are expressed as median ± IQR; n = 50 cells from 3 animals for each group. ****P < 0.0001.

C. Confocal microscope shows the cytoplasmic (could colocalize with mitochondrial) PRMT1 level in cultured (myo)fibroblasts from normal RV, cRVH and dRVH. Quantification values are expressed as median ± IQR; n = 50 cells from 3 experiments. *P < 0.05; **P < 0.01; ****P < 0.0001.

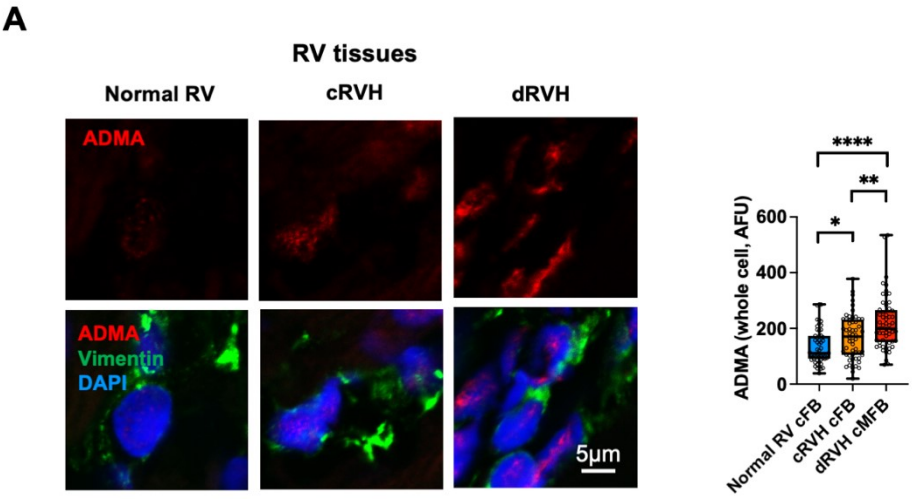
A
RV tissues
Normal RV
cRVH
dRVH
ADMA
ADMA
Vimentin
DAPI
5μm
ADMA (whole cell, AFU)
****
**
*
600
400
200
0
Normal RV cFB
cRVH cFB
dRVH cMFB

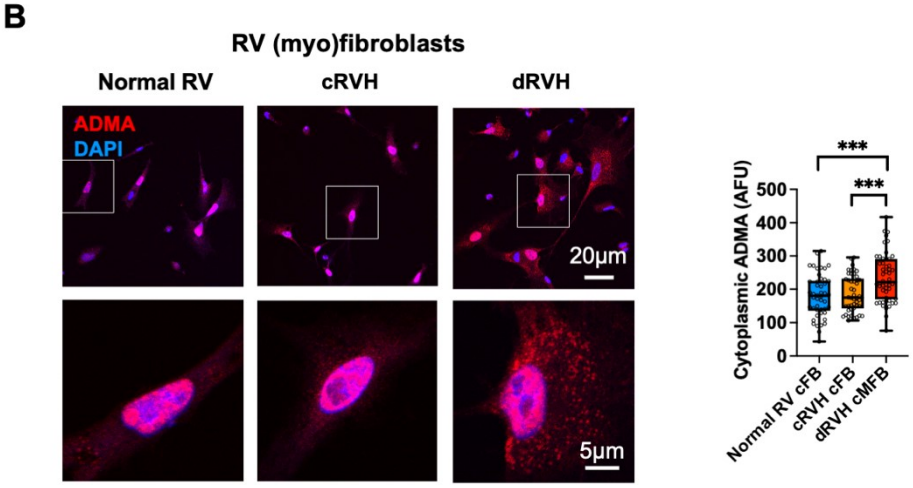
B
RV (myo)fibroblasts
Normal RV
cRVH
dRVH
ADMA
DAPI
20μm
5μm
Cytoplasmic ADMA (AFU)
***
***
500
400
300
200
100
0
Normal RV cFB
cRVH cFB
dRVH cMFB

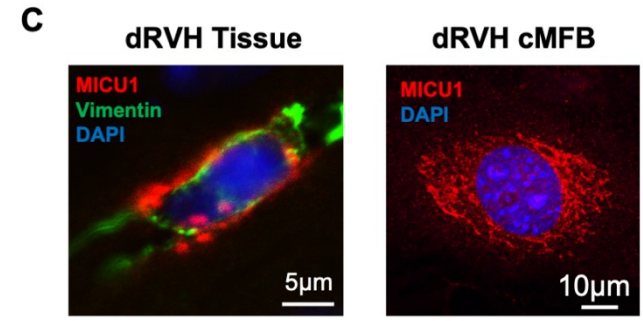
C
dRVH Tissue
dRVH cMFB
MICU1
Vimentin
DAPI
5μm
MICU1
DAPI
10μm

Figure 3. 4. The status of Arginine methylation is increased in dRVH myofibroblasts compared with normal RV and cRVH fibroblasts.

A. Confocal microscope shows the AMDA level (i.e. arginine methylation level) in (myo)fibroblasts (vimentin-positive cells) from right ventricle frozen sections of Control, cRVH and dRVH. Quantification values are expressed as median ± IQR; n = 50 cells from 3 animals for each group. *P < 0.05; **P < 0.01; ****P < 0.0001.

B. Confocal microscope shows the cytoplasmic (could colocalize with mitochondrial) ADMA level in cultured (myo)fibroblasts from normal RV, cRVH and dRVH. Quantification values are expressed as median ± IQR; n = 50 cells from 3 experiments. ***P < 0.001.

C. Confocal microscope shows the pattern of MICU1 in dRVH myofibroblasts both in-vivo (RV tissue) and in-vitro (cultured cells).

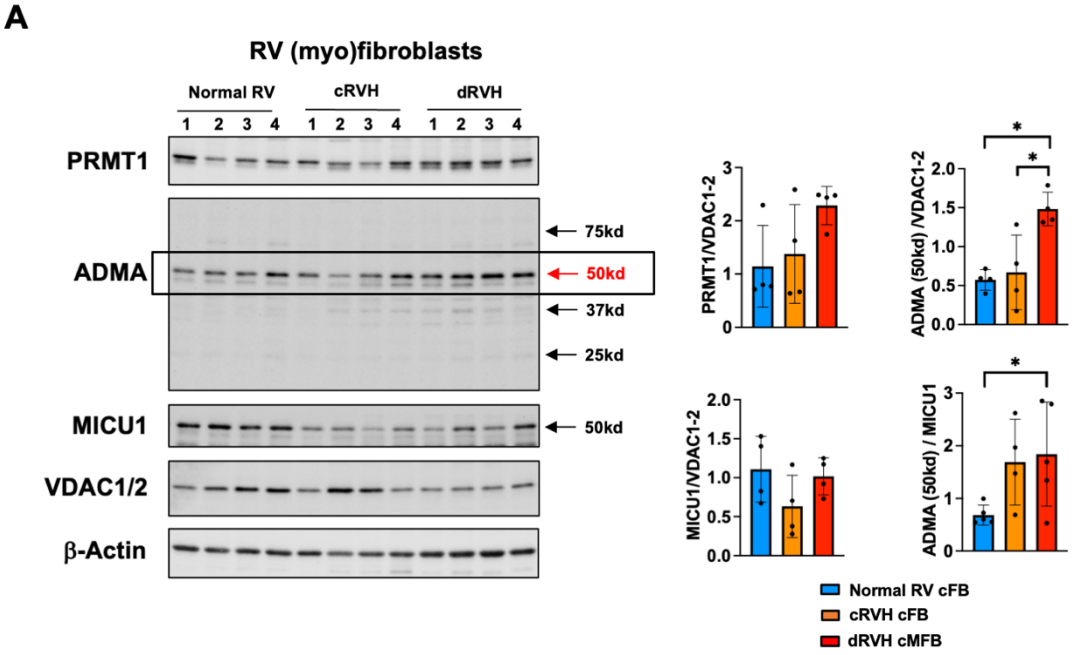
A
RV (myo)fibroblasts
Normal RV
cRVH
dRVH
1 2 3 4 1 2 3 4 1 2 3 4
PRMT1
ADMA
MICU1
VDAC1/2
β-Actin
75kd
50kd
37kd
25kd
50kd
PRMT1/VDAC1-2
ADMA (50kd) /VDAC1-2
MICU1/VDAC1-2
ADMA (50kd) / MICU1
Normal RV cFB
cRVH cFB
dRVH cMFB

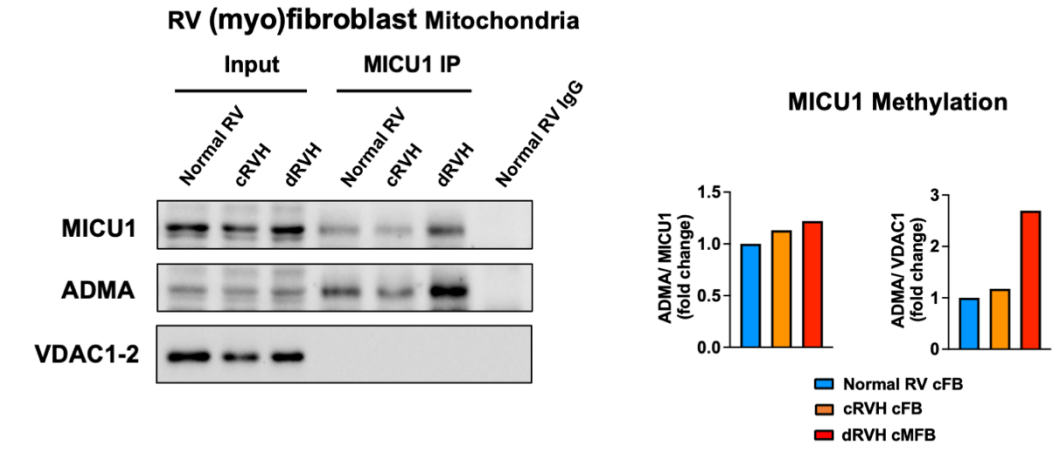
B
RV (myo)fibroblast Mitochondria
Input
MICU1 IP
Normal RV
cRVH
dRVH
Normal RV
cRVH
dRVH
Normal RV IgG
MICU1
ADMA
VDAC1-2
MICU1 Methylation
ADMA/ MICU1 (fold change)
ADMA/ VDAC1 (fold change)
Normal RV cFB
cRVH cFB
dRVH cMFB

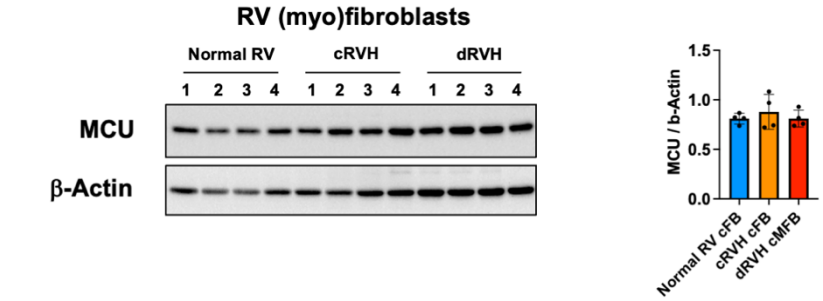
C
RV (myo)fibroblasts
Normal RV
cRVH
dRVH
1 2 3 4 1 2 3 4 1 2 3 4
MCU
β-Actin
MCU / b-Actin
Normal RV cFB
cRVH cFB
dRVH cMFB

Figure 3. 5. MICU1 methylation is increased in dRVH myofibroblasts compared with normal RV and cRVH fibroblasts while MCU level is not different.

A. Immunoblot shows the amount of PRMT1, ADMA, MICU1, VDAC1/2 and β-Actin in (myo)fibroblasts from normal RV, cRVH and dRVH. The ADMA band in the black rectangle is in 50kd, same as the molecular weight of MICU1. Quantification values are expressed as mean ± SEM; n = 4 animals for each group. *$P < 0.05$.

B. MICU1 Immunoprecipitation of isolated (myo)fibroblast mitochondrial shows the amount of MICU1 and ADMA. MICU1 is calculated as ADMA/MICU1; Methylated MICU1 is shown as the ADMA level in this MICU1 immunoprecipitation.

C. Immunoblot shows the amount of MCU and β-Actin. Quantification values are expressed as mean ± SEM; n = 4 animals for each group.

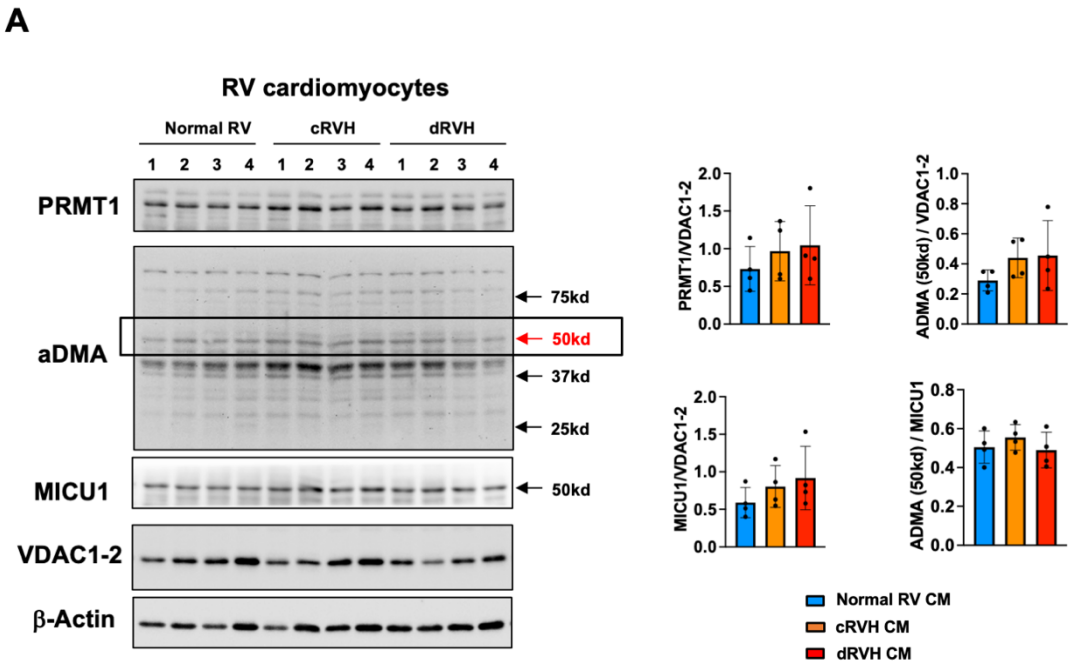

Figure 3. 6. MICU1 methylation is not different in cardiomyocytes among normal RV, cRVH and dRVH.

A. Immunoblot shows the amount of PRMT1, ADMA, MICU1, VDAC1/2 and β-Actin in cardiomyocytes from normal RV, cRVH and dRVH. The ADMA band in the black rectangle is in 50kd, same as the molecular weight of MICU1. Quantification values are expressed as mean ± SEM; n = 4 animals for each group.

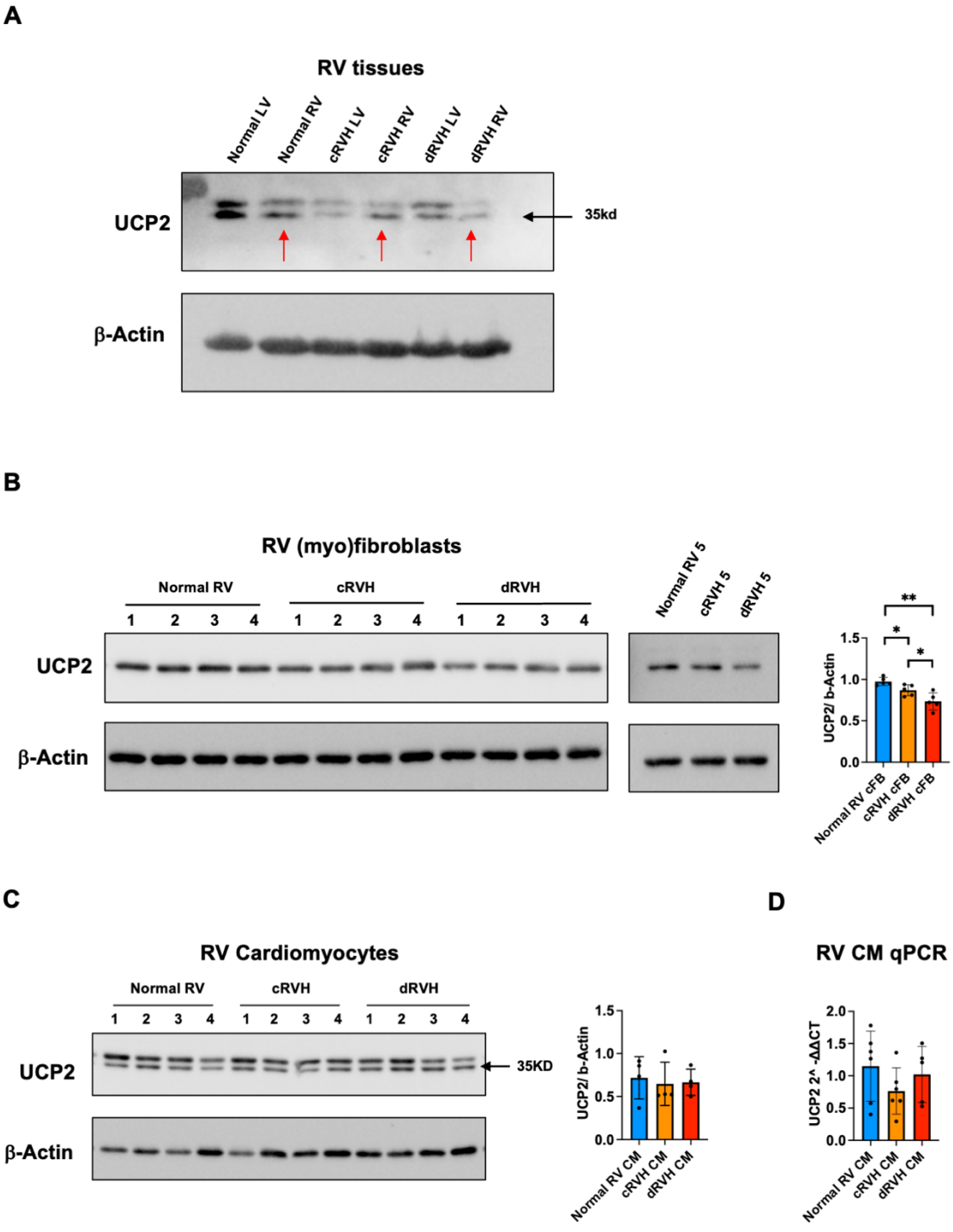
A
RV tissues
Normal LV
Normal RV
cRVH LV
cRVH RV
dRVH LV
dRVH RV
UCP2
35kd
β-Actin
B
RV (myo)fibroblasts
Normal RV
cRVH
dRVH
1 2 3 4 1 2 3 4 1 2 3 4
Normal RV 5
cRVH 5
dRVH 5
UCP2
β-Actin
UCP2/ b-Actin
Normal RV cFB
cRVH cFB
dRVH cFB
C
RV Cardiomyocytes
Normal RV
cRVH
dRVH
1 2 3 4 1 2 3 4 1 2 3 4
UCP2
35KD
β-Actin
UCP2/ b-Actin
Normal RV CM
cRVH CM
dRVH CM
D
RV CM qPCR
UCP2 2^ -ΔΔCT
Normal RV CM
cRVH CM
dRVH CM

Figure 3. 7. UCP2 level is decreased in (myo)fibroblasts from normal RV to cRVH to dRVH, not in cardiomyocytes.

A. Immunoblot shows the amount of UCP2 and β-Actin in the myocardium of the left ventricle and right ventricle from Control, cRVH and dRVH rats. UCP2 is the lower band with a molecular weight of 35kd (Verified by UCP2 WT and KO immunoblot) and red arrows point the right ventricles.

B. Immunoblot shows the amount of UCP2 and β-Actin in (myo)fibroblasts from normal RV, cRVH and dRVH. Quantification values are expressed as mean ± SEM; n = 5 animals for each group. *P < 0.05; **P < 0.01.

C. Immunoblot shows the amount of UCP2 and β-Actin in cardiomyocytes from normal RV, cRVH and dRVH. Quantification values are expressed as mean ± SEM; n = 4 animals for each group.

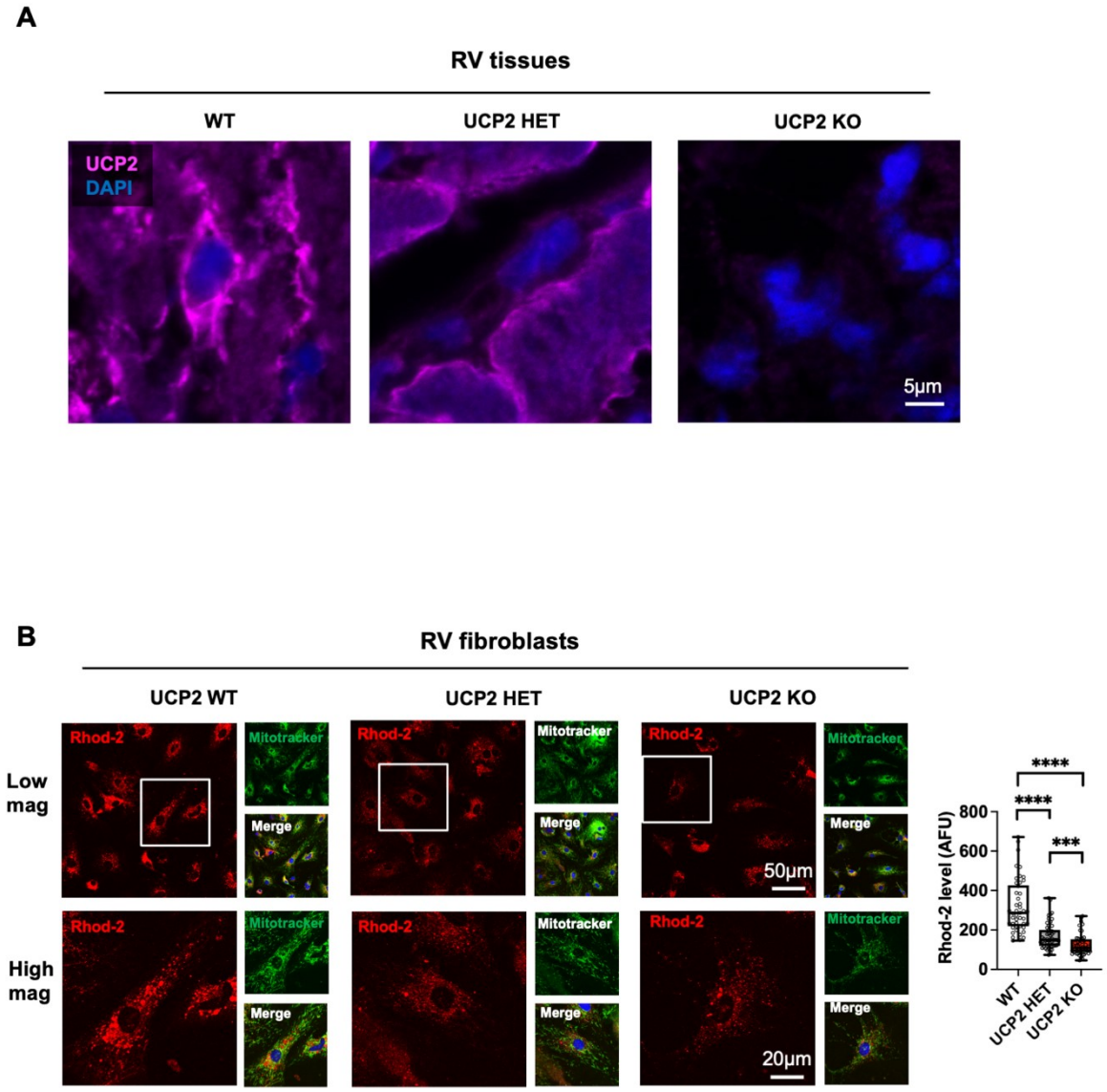
A
RV tissues
WT
UCP2 HET
UCP2 KO
UCP2
DAPI
5μm
B
RV fibroblasts
UCP2 WT
UCP2 HET
UCP2 KO
Low mag
High mag
Rhod-2
Mitotracker
Merge
50μm
20μm
Rhod-2 level (AFU)
0
200
400
600
800
****
****
***
WT
UCP2 HET
UCP2 KO

Figure 3. 8. A gene dose-dependent decrease is found in mitochondrial calcium as UCP2 levels decrease.

A. Confocal microscope shows the UCP2 (magenta) level in RV frozen tissue from WT, UCP2 heterozygous and UCP2 knockout mice.

B. Confocal microscope shows the mitochondrial calcium level (Rhod-2 fluorescence level) in cultured right ventricular (myo)fibroblasts from WT, UCP2 heterozygous and UCP2 knockout mice. Quantification values are expressed as median ± IQR; n = 50 cells from 3 experiments. ***P < 0.001; ****P < 0.0001.

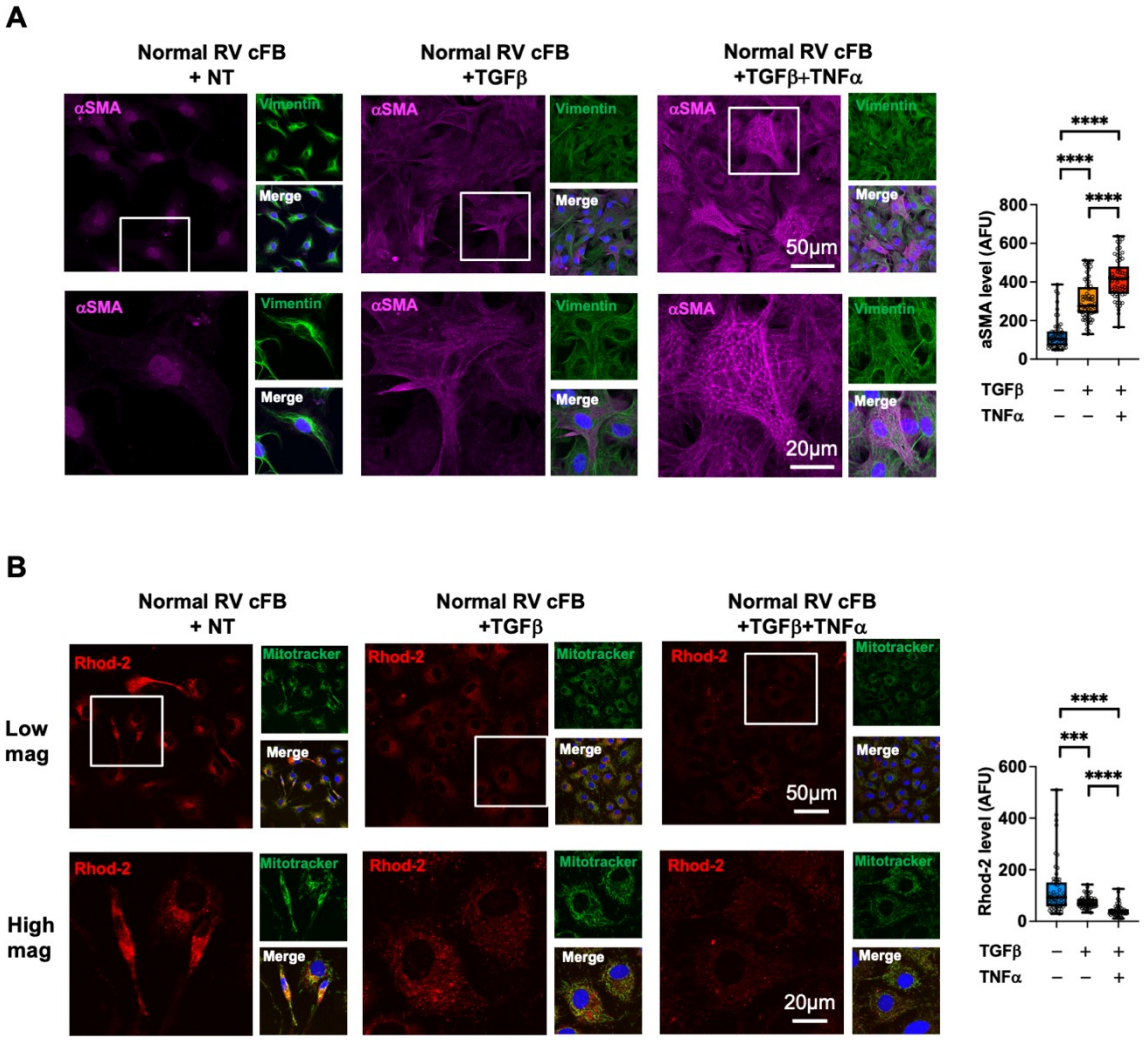
A
Normal RV cFB
+ NT
Normal RV cFB
+TGFβ
Normal RV cFB
+TGFβ+TNFα
αSMA
Vimentin
Merge
50μm
20μm
aSMA level (AFU)
800
600
400
200
0
****
****
****
TGFβ – + +
TNFα – – +
B
Low
mag
High
mag
Rhod-2
Mitotracker
Merge
50μm
20μm
Rhod-2 level (AFU)
600
400
200
0
***
****
****
TGFβ – + +
TNFα – – +

Figure 3. 9. TGFb induces myofibroblasts activation and mitochondrial decrease, but these effects are further induced by TNFα and TGFβ co-treatment.

A. Confocal microscope shows the α-SMA level in normal right ventricular fibroblast treated with NT (no treatment), TGFβ (10ng/ml, 72h) or TGFβ +TNFα (20ng/ml, 72h). Quantification values are expressed as median ± IQR; n = 50 cells from 3 experiments. ****P < 0.0001.

B. Confocal microscope shows the mitochondrial calcium level (Rhod-2 fluorescence level) in normal right ventricular fibroblast treated with NT (no treatment), TGFβ (10ng/ml, 72h) or TGFβ +TNFα (20ng/ml, 72h). Quantification values are expressed as median ± IQR; n = 50 cells from 3 experiments. ***P < 0.001; ****P < 0.0001.

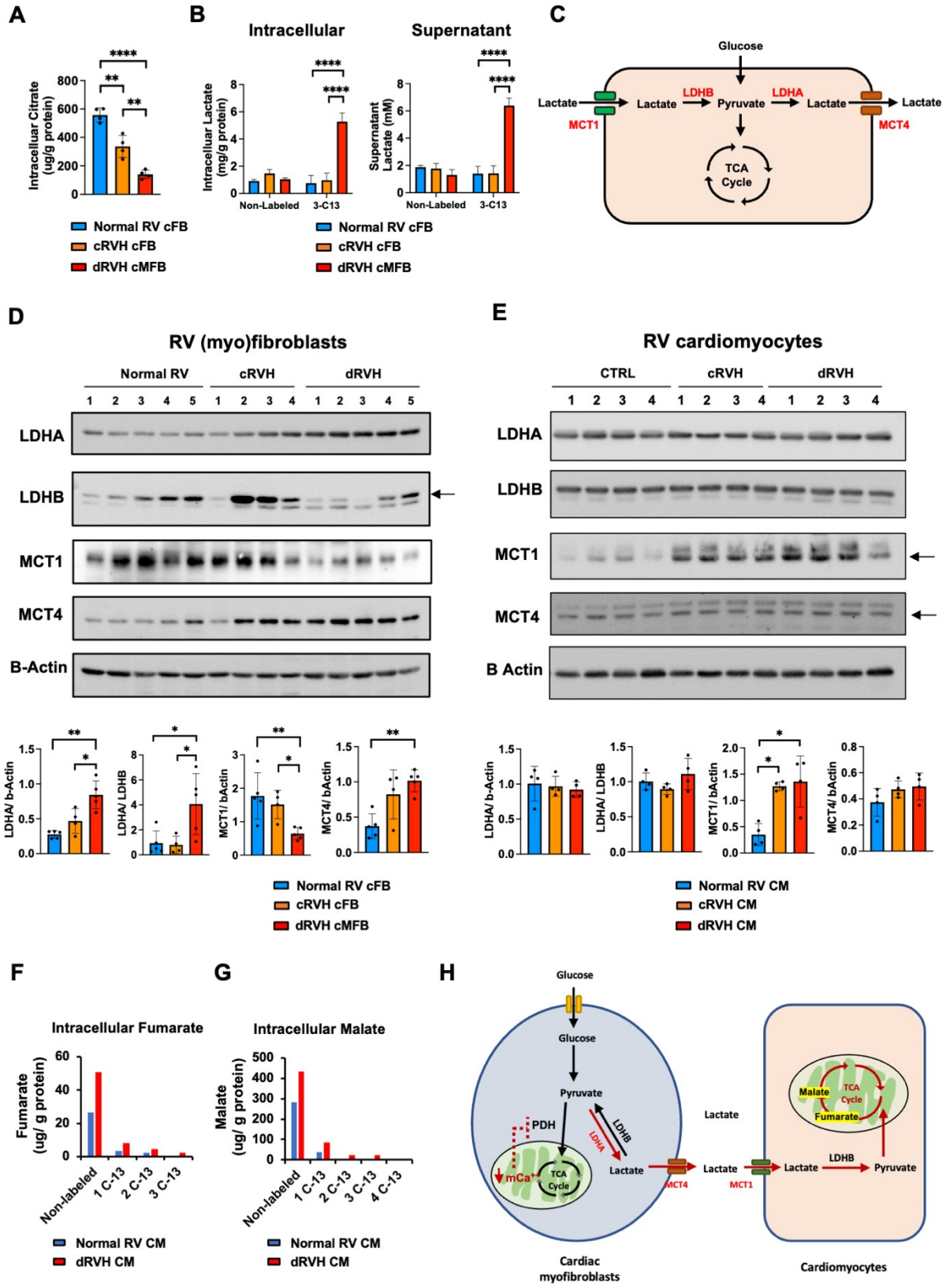
A
Intracellular Citrate (ug/g protein)
Normal RV cFB
cRVH cFB
dRVH cMFB
B
Intracellular
Supernatant
Intracellular Lactate (mg/g protein)
Supernatant Lactate (mM)
Non-Labeled
3-C13
C
Glucose
Lactate
LDHB
Pyruvate
LDHA
MCT1
MCT4
TCA Cycle
D
RV (myo)fibroblasts
Normal RV
cRVH
dRVH
LDHA
LDHB
MCT1
MCT4
B-Actin
LDHA/ b-Actin
LDHA/ LDHB
MCT1/ bActin
MCT4/ bActin
E
RV cardiomyocytes
CTRL
cRVH
dRVH
B Actin
Normal RV CM
cRVH CM
dRVH CM
F
Intracellular Fumarate
Fumarate (ug/ g protein)
Non-labeled
1 C-13
2 C-13
3 C-13
G
Intracellular Malate
Malate (ug/ g protein)
4 C-13
H
Glucose
Pyruvate
PDH
mCa
TCA Cycle
Lactate
Malate
Fumarate
Cardiac myofibroblasts
Cardiomyocytes

Figure 3. 10. The intracellular citrate level is decreased in DRVH myofibroblasts. DRVH myofibroblasts secrete lactate which is used by cardiomyocytes as a fuel.

A. Mass Spectrometry shows the intracellular citrate level in (myo)fibroblasts from normal RV, cRVH and dRVH. Quantification values are expressed as mean ± SEM; n = 4 animals for each group. **P < 0.01; ****P < 0.0001.

B. Mass Spectrometry shows the intracellular and supernatant lactate level of (myo)fibroblasts from normal RV, cRVH and dRVH after treatment with C-13 glucose (17.5mM) for 12h. Quantification values are expressed as mean ± SEM; n = 4 animals for each group. **P < 0.01; ****P < 0.0001.

C. The schematic of two enzymes (LDHA and LDHB) and two transporters (MCT1 and MCT4) related to lactate generation and transportation.

D, E. Immunoblot shows the amount of LDHA, LDHB, MCT1, MCT4 and β-Actin in (myo)fibroblasts **(D)** and cardiomyocytes **(E)** from normal RV, cRVH and dRVH. Quantification values are expressed as mean ± SEM; n = 4-5 animals for each group *P < 0.05; **P < 0.01.

F, G. Mass Spectrometry shows the intracellular fumarate **(F)** and malate **(G)** level in cardiomyocytes from normal RV and dRVH rats after being treated with C-13 lactate (5mM) for 2h. H, the potential schematic of how lactate be secreted by myofibroblasts and used by cardiomyocytes.

H. The potential schematic of fuel communication between myofibroblasts and cardiomyocytes.

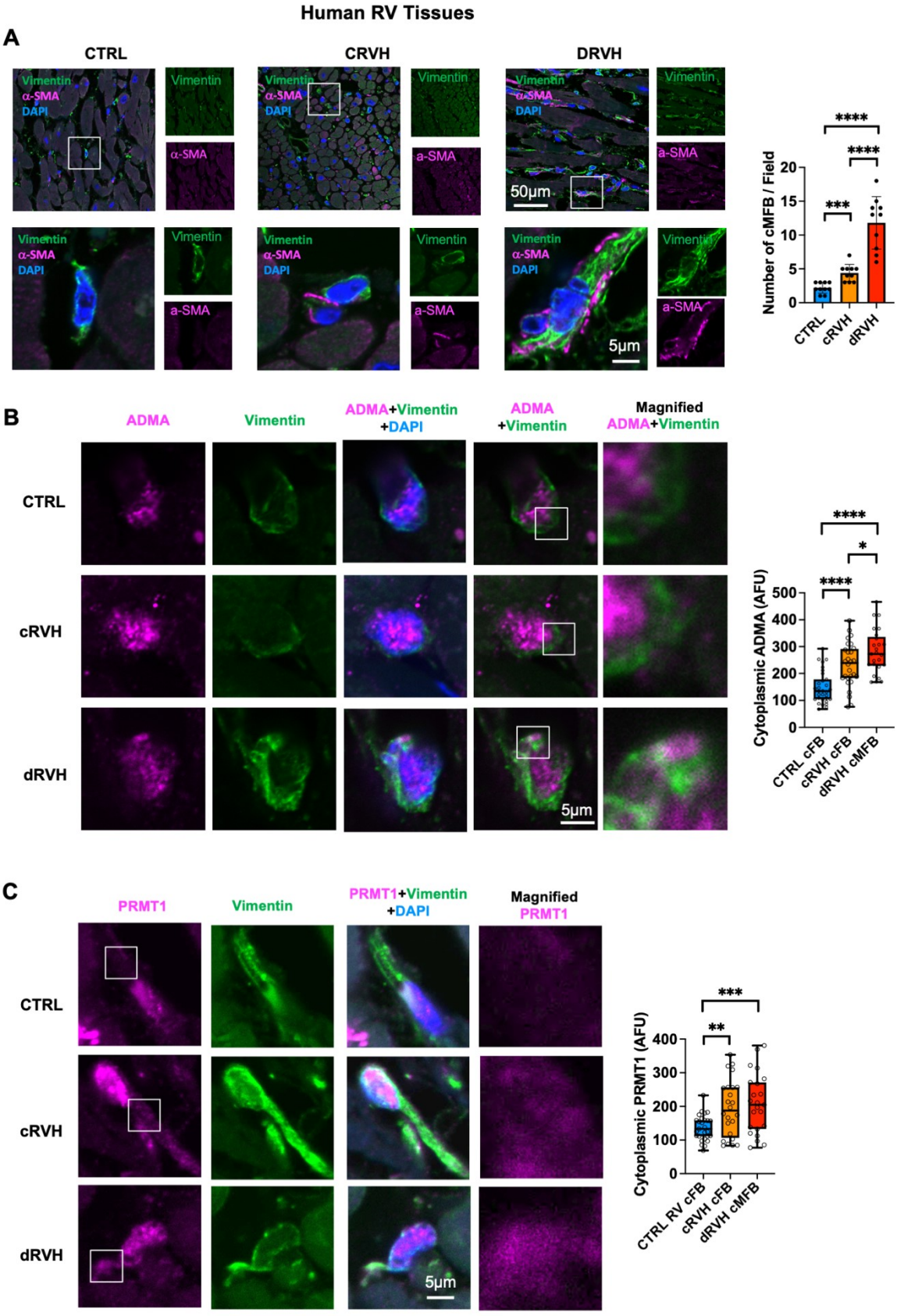
Human RV Tissues
A
CTRL
CRVH
DRVH
Vimentin
α-SMA
DAPI
a-SMA
50μm
5μm
Number of cMFB / Field
CTRL
cRVH
dRVH
B
ADMA
Vimentin
ADMA+Vimentin +DAPI
ADMA +Vimentin
Magnified ADMA+Vimentin
Cytoplasmic ADMA (AFU)
CTRL cFB
cRVH cFB
dRVH cMFB
C
PRMT1
PRMT1+Vimentin +DAPI
Magnified PRMT1
Cytoplasmic PRMT1 (AFU)
CTRL RV cFB

Figure 3. 11. The number of myofibroblasts is increased from CTRL RV to cRVH to dRVH while the arginine methyltransferase in (myo)fibroblasts increases from CTRL RV to cRVH but did not increase any further in dRVH in human.

A. Confocal microscope shows the number of myofibroblasts (positive with both a-SMA and Vimentin) in right ventricle paraffin-embedded sections from Control (CTRL), cRVH and dRVH patients. Quantification values are expressed as mean ± SEM; n = 5 patients for each group. ***P < 0.001.

B. Confocal microscope shows the cytoplasmic AMDA level (i.e. arginine methylation level) in (myo)fibroblasts (vimentin-positive cells) from right ventricle frozen sections of Control, cRVH and dRVH. Quantification values are expressed as median ± IQR; n = 50 cells from 5 patients in each group. *P < 0.05; ****P < 0.0001.

C. Confocal microscope shows the cytoplasmic PRMT1 level in (myo)fibroblasts (vimentin-positive cells) from right ventricle frozen sections of Control, cRVH and dRVH. Quantification values are expressed as median ± IQR; n = 50 cells from 5 patients in each group. **P < 0.01; ***P < 0.001.

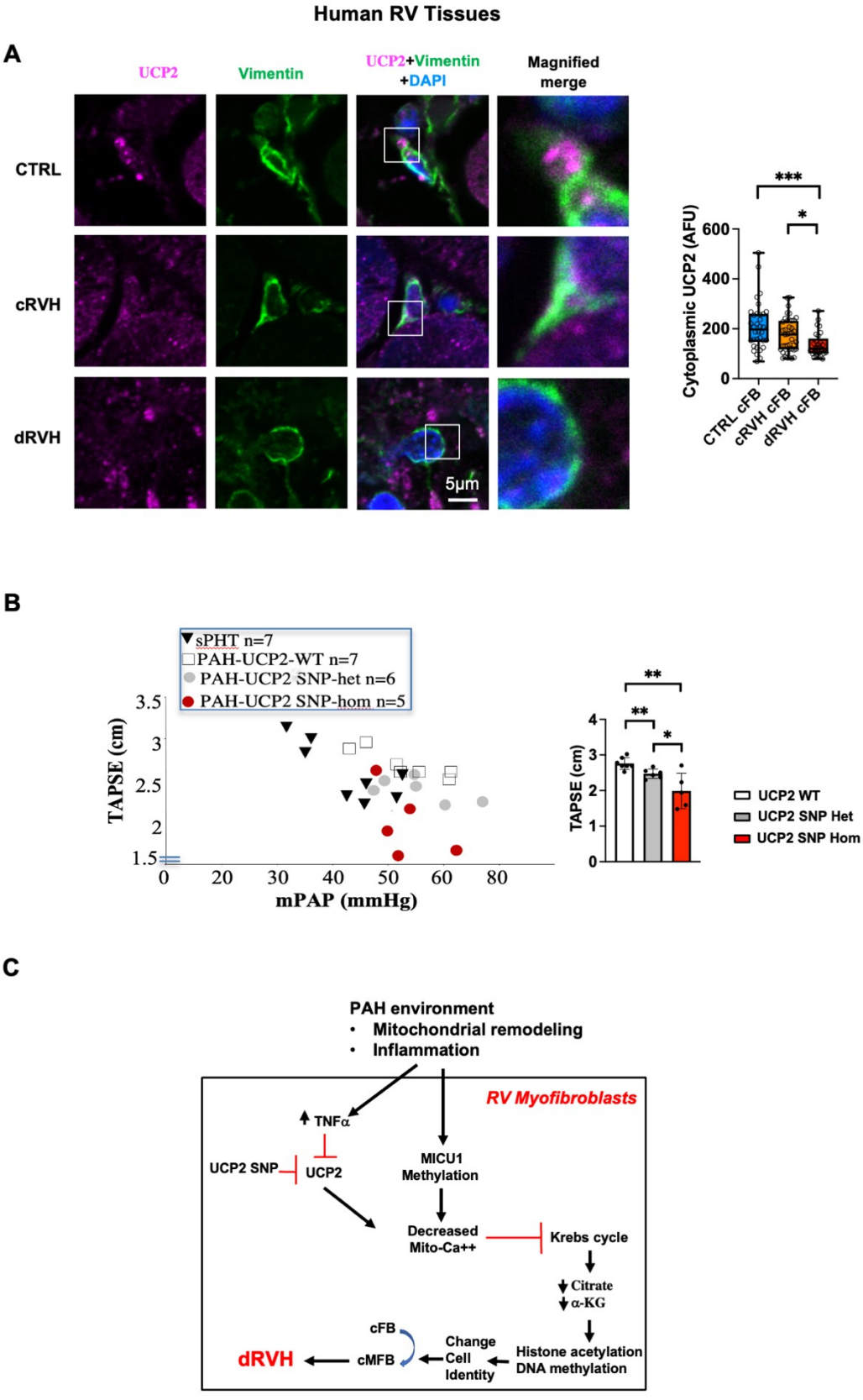
Human RV Tissues
A
UCP2
Vimentin
UCP2+Vimentin +DAPI
Magnified merge
CTRL
cRVH
dRVH
5μm
Cytoplasmic UCP2 (AFU)
CTRL cFB
cRVH cFB
dRVH cFB
B
sPHT n=7
PAH-UCP2-WT n=7
PAH-UCP2 SNP-het n=6
PAH-UCP2 SNP-hom n=5
TAPSE (cm)
mPAP (mmHg)
UCP2 WT
UCP2 SNP Het
UCP2 SNP Hom
C
PAH environment
Mitochondrial remodeling
Inflammation
RV Myofibroblasts
TNFα
UCP2 SNP
UCP2
MICU1 Methylation
Decreased Mito-Ca++
Krebs cycle
Citrate
α-KG
Histone acetylation DNA methylation
Change Cell Identity
cFB
cMFB
dRVH

Figure 3.12. UCP2 level is decreased in (myo)fibroblasts from CTRL RV to cRVH to dRVH in human. UCP SNP in patients with pulmonary hypertension is correlated with worse RV function.

A. Confocal microscope shows the cytoplasmic UCP2 level in (myo)fibroblasts (vimentin-positive cells) from right ventricle frozen sections of Control (CTRL), cRVH and dRVH. Quantification values are expressed as median ± IQR; n = 50 cells from 5 patients in each group. *P < 0.05; ***P < 0.001.

B. Echocardiography and in-chest catheterization show the correlation between mean pulmonary arterial pressure (mPAP) and TAPSE (i.e. RV function) in sPHT, UCP2-WT (wildtype) PAH, UCP2 -SNP-het (heterozygous) and UCP2-SNP-hom (homozygous). Quantification values are expressed as mean ± SEM; n = 6-7 patients for each group. *P < 0.05; **P < 0.01.

C. A proposed mechanism of how myofibroblasts are activated in PAH patients and its effect on RV decomposition.

Chapter four

Discussion

The body of the work described in Chapters 2 and 3 focuses on lung vascular biology and RV physiology and biology. These two areas may appear to be quite different from each other at first. However, they have common denominator, ie. changes in cell identity.

In Chapter 2, knock out two genes (Sirt3 and Ucp2) that encode methandriol proteins, produced a mouse model that is quite close to human PAH, exhibiting severe PAH at a young age, RV failure, insulin resistance, and more importantly, frequent plexogenic lesion that appear quite early in the development of the disease. This suggests that they may directly contribute to the development of the disease, rather than representing late complications of the disease. We have already obtained some preliminary data (after the publication of our paper describing this model, suggesting that the plexogenic lesion may be driven by one cell type, rather than anarchic proliferation of 3 cell types (endothelial, smooth muscle, fibroblasts)). We used simultaneous staining and high-definition confocal microscopy of these plexogenic lesions and showed that a single cell type expresses all 3 proteins: von Willebrand factor (VWF), alpha smooth muscle actin (α-SMA) and Vimentin which are the markers for endothelial cells, smooth muscle cells and fibroblasts (**Fig 4.1**). This suggests that this cell type may be a myofibroblast, which is known to express all 3 proteins. This cell can be derived by either endothelial or smooth muscle or fibroblasts cells. In other words, this is may be the result of a change in cell identity process occurring in the pulmonary artery wall similar to the change in cell identity that occurs in the RV, described in chapter 3. Since the TGF-β axis is important in changes in cell identity[94] and since mutations on the TGF receptor family are in all cell types in PAH patients[95], and since inflammation (eg. TNFα) can promote the formation of myofibroblasts[96], it is attractive to speculate that this is happening in parallel in the pulmonary vessels and the RV. And it is also important to realize that the myofibroblasts are pro-inflammatory and produce cytokines[97]; in other words they both produce and get activated by

inflammation, creating a spiral positively reinforcing feedback loop that may underscore the progression of PAH. To prove this theory many more studies need to take place, beyond the scope of this thesis in the next several years, including cell origin tracking in the pulmonary artery cell population during the development of the plexogenic lesion (which will now be possible with our newly described mouse model), and confirmation of the prominent myofibroblast presence in human tissues from large cohorts.

We propose that the first thing that may happen to the pulmonary arteries in response to an early injury/loss of endothelial cells, is the transformation of vascular cells into myofibroblasts, in an attempt to repair the damage. This may be particularly enhanced in patients carrying mutations in the TGFβ axis (eg. familial PAH) or in patients with increase burden of inflammation (eg. scleroderma). This will be further accelerated through a second hit, like a primary mitochondrial dysfunction, like the abnormal mitochondria caused by the loss of function SNPs that we described. Initially, like it happens in wound healing in general, these myofibroblasts are very proliferative. However, there is evidence that after some time, they stop proliferating and they reach a state of senesce[98]. Recent work has described that senescence is prevalent in human PAH and rat model[99]. Because these cells are not actively proliferating. It is not surprising that they do not respond to antiproliferative drugs, like the complete lack of response of human plexogenic lesions to epoprostenol long-term therapy[46,47]. Rather, such therapies caused regression of PAH only after a senolytic drug was given to the rat PAH model[99]. This means that the future treatment of PAH may include: a) senolytic drugs; b) drugs that may be able to reverse the change of cell identity in the pulmonary artery, including mitochondria-targeting drugs (like dichloroacetate or similar drugs) and epigenetics-targeting drugs (like histone deacetylation inhibitors or similar drugs. It is

important to note that some of the most promising experimental PAH drugs, like Sotatercept (that has successfully complete phase 1 and 2 clinical trials[10,93]) may actually work, at least in part, through epigenetic mechanisms, since its downstream effects, in addition to SMADS, involve histone acetylation. Unfortunately, in the sotatercept development studies, this possibility has not been addressed and it is unknown whether this drug affects the plexogenic lesions or (even more intriguingly) whether it affects the transformation of cMF in the RV.

Lastly, my work in chapter3 suggests a similar approach for the treatment of dRVH, for which there is currently no available therapy. This may include senolytic, anti-inflammatory drugs (eg. anti-TNFα biologics), mitochondria- and epigenetic-targeting drugs, particularly in patients carrying the SIRT3 and UCP2 SNPs. It needs to be determined with future work a) whether the role of these SNPs in predicting dRVH is confirmed in large and independent cohorts and b) whether these therapies can simply prevent/delay the onset of dRVH, or actually they can reverse established dRVH. The beauty of such therapies is that they may be able to target the plexogenic lesions and the dRVH in parallel and independent from each other. However, this also means that to show direct and independent effects on the pulmonary arteries and the RV, "the PA/RV unit" needs to be experimentally disrupted, by using additional models, including the "PA banding" model.

Overall, my work provides further support to the metabolic theory of PAH and also opens a new window in the field, ie. the role of Cell Identity on PAH, which I believe may dominate the field in the future.

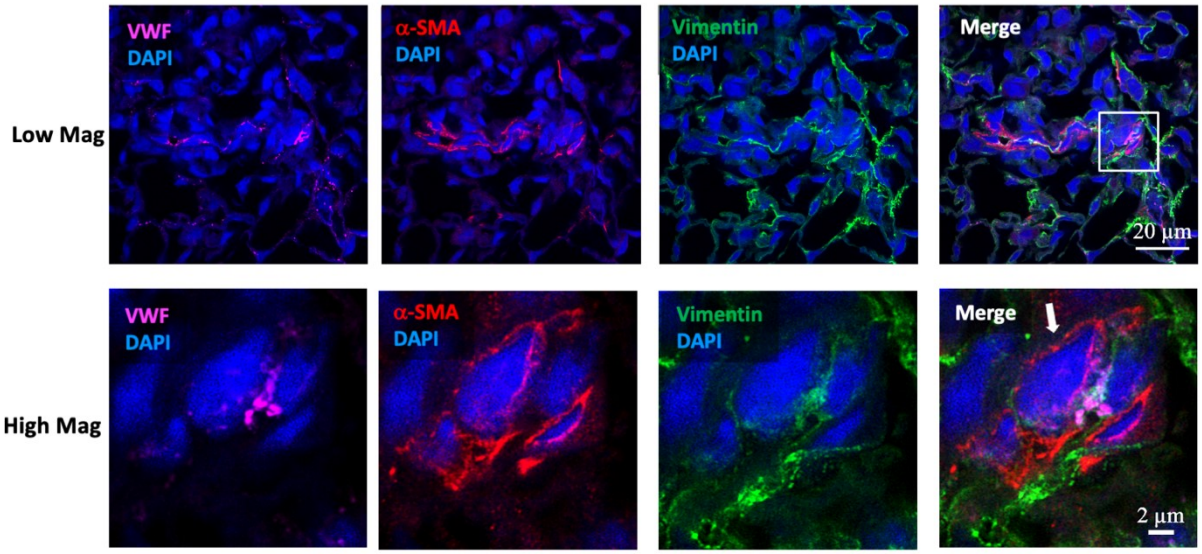

Figure 4. 1. Cells in plexogenic lesions simultaneously express von Willebrand factor (VWF), alpha smooth muscle actin (α –SMA) and Vimentin.

Confocal microscope shows the staining of VWF, a –SMA and Vimentin in plexogenic lesions from the lung of SIRT3/UCP2 double knockout mice. The white arrow pointed cell simultaneously expresses positive signals for VWF, SMA and Vimentin.

References

1. Sutendra G, Michelakis ED. Pulmonary arterial hypertension: challenges in translational research and a vision for change. *Sci Transl Med*. 2013;5:208sr205. doi: 10.1126/scitranslmed.3005428

2. Sutendra G, Michelakis ED. The metabolic basis of pulmonary arterial hypertension. *Cell Metab*. 2014;19:558-573. doi: 10.1016/j.cmet.2014.01.004

3. Bonnet S, Rochefort G, Sutendra G, Archer SL, Haromy A, Webster L, Hashimoto K, Bonnet SN, Michelakis ED. The nuclear factor of activated T cells in pulmonary arterial hypertension can be therapeutically targeted. *Proc Natl Acad Sci U S A*. 2007;104:11418-11423. doi: 10.1073/pnas.0610467104

4. Sutendra G, Bonnet S, Rochefort G, Haromy A, Folmes KD, Lopaschuk GD, Dyck JR, Michelakis ED. Fatty acid oxidation and malonyl-CoA decarboxylase in the vascular remodeling of pulmonary hypertension. *Sci Transl Med*. 2010;2:44ra58. doi: 10.1126/scitranslmed.3001327

5. Bonnet S, Michelakis ED, Porter CJ, Andrade-Navarro MA, Thebaud B, Bonnet S, Haromy A, Harry G, Moudgil R, McMurtry MS, et al. An abnormal mitochondrial-hypoxia inducible factor-1alpha-Kv channel pathway disrupts oxygen sensing and triggers pulmonary arterial hypertension in fawn hooded rats: similarities to human pulmonary arterial hypertension. *Circulation*. 2006;113:2630-2641. doi: 10.1161/CIRCULATIONAHA.105.609008

6. Paulin R, Courboulin A, Meloche J, Mainguy V, Dumas de la Roque E, Saksouk N, Cote J, Provencher S, Sussman MA, Bonnet S. Signal transducers and activators of transcription-3/pim1 axis plays a critical role in the pathogenesis of human pulmonary arterial

hypertension. *Circulation*. 2011;123:1205-1215. doi: 10.1161/CIRCULATIONAHA.110.963314

7. Pietra GG, Capron F, Stewart S, Leone O, Humbert M, Robbins IM, Reid LM, Tuder RM. Pathologic assessment of vasculopathies in pulmonary hypertension. *J Am Coll Cardiol*. 2004;43:25S-32S. doi: 10.1016/j.jacc.2004.02.033

8. Soubrier F, Chung WK, Machado R, Grunig E, Aldred M, Geraci M, Loyd JE, Elliott CG, Trembath RC, Newman JH, et al. Genetics and genomics of pulmonary arterial hypertension. *J Am Coll Cardiol*. 2013;62:D13-21. doi: 10.1016/j.jacc.2013.10.035

9. Chan SY, Loscalzo J. Pathogenic mechanisms of pulmonary arterial hypertension. *J Mol Cell Cardiol*. 2008;44:14-30. doi: 10.1016/j.yjmcc.2007.09.006

10. Yung LM, Yang P, Joshi S, Augur ZM, Kim SSJ, Bocobo GA, Dinter T, Troncone L, Chen PS, McNeil ME, et al. ACTRIIA-Fc rebalances activin/GDF versus BMP signaling in pulmonary hypertension. *Sci Transl Med*. 2020;12. doi: 10.1126/scitranslmed.aaz5660

11. Yamamura H, Yamamura A, Ko EA, Pohl NM, Smith KA, Zeifman A, Powell FL, Thistlethwaite PA, Yuan JX. Activation of Notch signaling by short-term treatment with Jagged-1 enhances store-operated Ca(2+) entry in human pulmonary arterial smooth muscle cells. *Am J Physiol Cell Physiol*. 2014;306:C871-878. doi: 10.1152/ajpcell.00221.2013

12. Li X, Zhang X, Leathers R, Makino A, Huang C, Parsa P, Macias J, Yuan JX, Jamieson SW, Thistlethwaite PA. Notch3 signaling promotes the development of pulmonary arterial hypertension. *Nat Med*. 2009;15:1289-1297. doi: 10.1038/nm.2021

13. Sutendra G, Dromparis P, Bonnet S, Haromy A, McMurtry MS, Bleackley RC, Michelakis ED. Pyruvate dehydrogenase inhibition by the inflammatory cytokine TNFalpha contributes to the pathogenesis of pulmonary arterial hypertension. *J Mol Med (Berl)*. 2011;89:771-783. doi: 10.1007/s00109-011-0762-2

14. Fijalkowska I, Xu W, Comhair SA, Janocha AJ, Mavrakis LA, Krishnamachary B, Zhen L, Mao T, Richter A, Erzurum SC, et al. Hypoxia inducible-factor1alpha regulates the metabolic shift of pulmonary hypertensive endothelial cells. *Am J Pathol*. 2010;176:1130-1138. doi: 10.2353/ajpath.2010.090832

15. MacKenzie ED, Selak MA, Tennant DA, Payne LJ, Crosby S, Frederiksen CM, Watson DG, Gottlieb E. Cell-permeating alpha-ketoglutarate derivatives alleviate pseudohypoxia in succinate dehydrogenase-deficient cells. *Mol Cell Biol*. 2007;27:3282-3289. doi: 10.1128/MCB.01927-06

16. Dromparis P, Michelakis ED. Mitochondria in vascular health and disease. *Annu Rev Physiol*. 2013;75:95-126. doi: 10.1146/annurev-physiol-030212-183804

17. Ahn BH, Kim HS, Song S, Lee IH, Liu J, Vassilopoulos A, Deng CX, Finkel T. A role for the mitochondrial deacetylase Sirt3 in regulating energy homeostasis. *Proc Natl Acad Sci U S A*. 2008;105:14447-14452. doi: 10.1073/pnas.0803790105

18. Bondarenko AI, Parichatikanond W, Madreiter CT, Rost R, Waldeck-Weiermair M, Malli R, Graier WF. UCP2 modulates single-channel properties of a MCU-dependent Ca(2+) inward current in mitochondria. *Pflugers Arch*. 2015;467:2509-2518. doi: 10.1007/s00424-015-1727-z

19. Motloch LJ, Larbig R, Gebing T, Reda S, Schwaiger A, Leitner J, Wolny M, Eckardt L, Hoppe UC. By Regulating Mitochondrial Ca2+-Uptake UCP2 Modulates Intracellular Ca2+. *PLoS One*. 2016;11:e0148359. doi: 10.1371/journal.pone.0148359

20. Paulin R, Dromparis P, Sutendra G, Gurtu V, Zervopoulos S, Bowers L, Haromy A, Webster L, Provencher S, Bonnet S, et al. Sirtuin 3 deficiency is associated with inhibited mitochondrial function and pulmonary arterial hypertension in rodents and humans. *Cell Metab*. 2014;20:827-839. doi: 10.1016/j.cmet.2014.08.011

21. Dromparis P, Paulin R, Sutendra G, Qi AC, Bonnet S, Michelakis ED. Uncoupling protein 2 deficiency mimics the effects of hypoxia and endoplasmic reticulum stress on mitochondria and triggers pseudohypoxic pulmonary vascular remodeling and pulmonary hypertension. *Circ Res*. 2013;113:126-136. doi: 10.1161/CIRCRESAHA.112.300699

22. Michelakis ED, Gurtu V, Webster L, Barnes G, Watson G, Howard L, Cupitt J, Paterson I, Thompson RB, Chow K, et al. Inhibition of pyruvate dehydrogenase kinase improves pulmonary arterial hypertension in genetically susceptible patients. *Sci Transl Med*. 2017;9. doi: 10.1126/scitranslmed.aao4583

23. Goldthorpe H, Jiang JY, Taha M, Deng Y, Sinclair T, Ge CX, Jurasz P, Turksen K, Mei SH, Stewart DJ. Occlusive lung arterial lesions in endothelial-targeted, fas-induced apoptosis transgenic mice. *Am J Respir Cell Mol Biol*. 2015;53:712-718. doi: 10.1165/rcmb.2014-0311OC

24. Maurer B, Reich N, Juengel A, Kriegsmann J, Gay RE, Schett G, Michel BA, Gay S, Distler JH, Distler O. Fra-2 transgenic mice as a novel model of pulmonary hypertension

associated with systemic sclerosis. *Ann Rheum Dis*. 2012;71:1382-1387. doi: 10.1136/annrheumdis-2011-200940

25. Abe K, Toba M, Alzoubi A, Ito M, Fagan KA, Cool CD, Voelkel NF, McMurtry IF, Oka M. Formation of plexiform lesions in experimental severe pulmonary arterial hypertension. *Circulation*. 2010;121:2747-2754. doi: 10.1161/CIRCULATIONAHA.109.927681

26. D'Adamo M, Perego L, Cardellini M, Marini MA, Frontoni S, Andreozzi F, Sciacqua A, Lauro D, Sbraccia P, Federici M, et al. The -866A/A genotype in the promoter of the human uncoupling protein 2 gene is associated with insulin resistance and increased risk of type 2 diabetes. *Diabetes*. 2004;53:1905-1910. doi: 10.2337/diabetes.53.7.1905

27. Dalgaard LT. Genetic Variance in Uncoupling Protein 2 in Relation to Obesity, Type 2 Diabetes, and Related Metabolic Traits: Focus on the Functional -866G>A Promoter Variant (rs659366). *J Obes*. 2011;2011:340241. doi: 10.1155/2011/340241

28. Wang H, Chu WS, Lu T, Hasstedt SJ, Kern PA, Elbein SC. Uncoupling protein-2 polymorphisms in type 2 diabetes, obesity, and insulin secretion. *Am J Physiol Endocrinol Metab*. 2004;286:E1-7. doi: 10.1152/ajpendo.00231.2003

29. Hirschey MD, Shimazu T, Jing E, Grueter CA, Collins AM, Aouizerat B, Stancakova A, Goetzman E, Lam MM, Schwer B, et al. SIRT3 deficiency and mitochondrial protein hyperacetylation accelerate the development of the metabolic syndrome. *Mol Cell*. 2011;44:177-190. doi: 10.1016/j.molcel.2011.07.019

30. Bogaard HJ, Abe K, Vonk Noordegraaf A, Voelkel NF. The right ventricle under pressure: cellular and molecular mechanisms of right-heart failure in pulmonary hypertension. *Chest*. 2009;135:794-804. doi: 10.1378/chest.08-0492

31. Haddad F, Hunt SA, Rosenthal DN, Murphy DJ. Right ventricular function in cardiovascular disease, part I: Anatomy, physiology, aging, and functional assessment of the right ventricle. *Circulation*. 2008;117:1436-1448. doi: 10.1161/CIRCULATIONAHA.107.653576

32. McLaughlin VV, Archer SL, Badesch DB, Barst RJ, Farber HW, Lindner JR, Mathier MA, McGoon MD, Park MH, Rosenson RS, et al. ACCF/AHA 2009 expert consensus document on pulmonary hypertension: a report of the American College of Cardiology Foundation Task Force on Expert Consensus Documents and the American Heart Association: developed in collaboration with the American College of Chest Physicians, American Thoracic Society, Inc., and the Pulmonary Hypertension Association. *Circulation*. 2009;119:2250-2294. doi: 10.1161/CIRCULATIONAHA.109.192230

33. Haddad F, Doyle R, Murphy DJ, Hunt SA. Right ventricular function in cardiovascular disease, part II: pathophysiology, clinical importance, and management of right ventricular failure. *Circulation*. 2008;117:1717-1731.

34. Bogaard HJ, Natarajan R, Henderson SC, Long CS, Kraskauskas D, Smithson L, Ockaili R, McCord JM, Voelkel NF. Chronic pulmonary artery pressure elevation is insufficient to explain right heart failure. *Circulation*. 2009;120:1951-1960. doi: 10.1161/CIRCULATIONAHA.109.883843

35. Dromparis P, Sutendra G, Michelakis ED. The role of mitochondria in pulmonary vascular remodeling. *J Mol Med*.88:1003-1010. doi: 10.1007/s00109-010-0670-x

36. Zamanian RT, Hansmann G, Snook S, Lilienfeld D, Rappaport KM, Reaven GM, Rabinovitch M, Doyle RL. Insulin resistance in pulmonary arterial hypertension. *Eur Respir J*. 2009;33:318-324. doi: 10.1183/09031936.00000508

37. Hassoun PM, Mouthon L, Barbera JA, Eddahibi S, Flores SC, Grimminger F, Jones PL, Maitland ML, Michelakis ED, Morrell NW, et al. Inflammation, growth factors, and pulmonary vascular remodeling. *J Am Coll Cardiol*. 2009;54:S10-S19. doi: 10.1016/j.jacc.2009.04.006

38. Pendergrass SA, Hayes E, Farina G, Lemaire R, Farber HW, Whitfield ML, Lafyatis R. Limited systemic sclerosis patients with pulmonary arterial hypertension show biomarkers of inflammation and vascular injury. *PLoS One*. 2010;5:e12106. doi: 10.1371/journal.pone.0012106

39. Soon E, Holmes AM, Treacy CM, Doughty NJ, Southgate L, Machado RD, Trembath RC, Jennings S, Barker L, Nicklin P, et al. Elevated levels of inflammatory cytokines predict survival in idiopathic and familial pulmonary arterial hypertension. *Circulation*. 2010;122:920-927. doi: 10.1161/CIRCULATIONAHA.109.933762

40. Michelakis ED, Wilkins MR, Rabinovitch M. Emerging concepts and translational priorities in pulmonary arterial hypertension. *Circulation*. 2008;118:1486-1495. doi: 10.1161/CIRCULATIONAHA.106.673988

41. Bishop SP, Altschuld RA. Increased glycolytic metabolism in cardiac hypertrophy and congestive failure. *Am J Physiol*. 1970;218:153-159. doi: 10.1152/ajplegacy.1970.218.1.153

42. Piao L, Fang YH, Cadete VJ, Wietholt C, Urboniene D, Toth PT, Marsboom G, Zhang HJ, Haber I, Rehman J, et al. The inhibition of pyruvate dehydrogenase kinase improves impaired cardiac function and electrical remodeling in two models of right ventricular

hypertrophy: resuscitating the hibernating right ventricle. *J Mol Med (Berl)*. 2010;88:47-60. doi: 10.1007/s00109-009-0524-6

43. Sutendra G, Dromparis P, Paulin R, Zervopoulos S, Haromy A, Nagendran J, Michelakis ED. A metabolic remodeling in right ventricular hypertrophy is associated with decreased angiogenesis and a transition from a compensated to a decompensated state in pulmonary hypertension. *J Mol Med (Berl)*. 2013;91:1315-1327. doi: 10.1007/s00109-013-1059-4

44. Gibb AA, Lazaropoulos MP, Elrod JW. Myofibroblasts and Fibrosis: Mitochondrial and Metabolic Control of Cellular Differentiation. *Circ Res*. 2020;127:427-447. doi: 10.1161/CIRCRESAHA.120.316958

45. Burr SD, Stewart JA, Jr. Rap1a Regulates Cardiac Fibroblast Contraction of 3D Diabetic Collagen Matrices by Increased Activation of the AGE/RAGE Cascade. *Cells*. 2021;10. doi: 10.3390/cells10061286

46. Pogoriler JE, Rich S, Archer SL, Husain AN. Persistence of complex vascular lesions despite prolonged prostacyclin therapy of pulmonary arterial hypertension. *Histopathology*. 2012;61:597-609. doi: 10.1111/j.1365-2559.2012.04246.x

47. Rich S, Pogoriler J, Husain AN, Toth PT, Gomberg-Maitland M, Archer SL. Long-term effects of epoprostenol on the pulmonary vasculature in idiopathic pulmonary arterial hypertension. *Chest*. 2010;138:1234-1239. doi: 10.1378/chest.09-2815

48. Paulin R, Michelakis ED. The metabolic theory of pulmonary arterial hypertension. *Circ Res*. 2014;115:148-164. doi: 10.1161/CIRCRESAHA.115.301130

49. Rabinovitch M, Guignabert C, Humbert M, Nicolls MR. Inflammation and immunity in the pathogenesis of pulmonary arterial hypertension. *Circ Res*. 2014;115:165-175. doi: 10.1161/CIRCRESAHA.113.301141

50. MacIver NJ, Michalek RD, Rathmell JC. Metabolic regulation of T lymphocytes. *Annu Rev Immunol*. 2013;31:259-283. doi: 10.1146/annurev-immunol-032712-095956

51. Malenfant S, Potus F, Fournier F, Breuils-Bonnet S, Pflieger A, Bourassa S, Tremblay E, Nehme B, Droit A, Bonnet S, et al. Skeletal muscle proteomic signature and metabolic impairment in pulmonary hypertension. *J Mol Med (Berl)*. 2015;93:573-584. doi: 10.1007/s00109-014-1244-0

52. Enache I, Charles AL, Bouitbir J, Favret F, Zoll J, Metzger D, Oswald-Mammosser M, Geny B, Charloux A. Skeletal muscle mitochondrial dysfunction precedes right ventricular impairment in experimental pulmonary hypertension. *Mol Cell Biochem*. 2013;373:161-170. doi: 10.1007/s11010-012-1485-6

53. Pak O, Sommer N, Hoeres T, Bakr A, Waisbrod S, Sydykov A, Haag D, Esfandiary A, Kojonazarov B, Veit F, et al. Mitochondrial hyperpolarization in pulmonary vascular remodeling. Mitochondrial uncoupling protein deficiency as disease model. *Am J Respir Cell Mol Biol*. 2013;49:358-367. doi: 10.1165/rcmb.2012-0361OC

54. Stacher E, Graham BB, Hunt JM, Gandjeva A, Groshong SD, McLaughlin VV, Jessup M, Grizzle WE, Aldred MA, Cool CD, et al. Modern age pathology of pulmonary arterial hypertension. *Am J Respir Crit Care Med*. 2012;186:261-272. doi: 10.1164/rccm.201201-0164OC

55. Trenker M, Malli R, Fertschai I, Levak-Frank S, Graier WF. Uncoupling proteins 2 and 3 are fundamental for mitochondrial Ca2+ uniport. *Nat Cell Biol*. 2007;9:445-452. doi: 10.1038/ncb1556

56. Sesti G, Cardellini M, Marini MA, Frontoni S, D'Adamo M, Del Guerra S, Lauro D, De Nicolais P, Sbraccia P, Del Prato S, et al. A common polymorphism in the promoter of UCP2 contributes to the variation in insulin secretion in glucose-tolerant subjects. *Diabetes*. 2003;52:1280-1283. doi: 10.2337/diabetes.52.5.1280

57. Qiu H, He Y, Ouyang F, Jiang P, Guo S, Guo Y. The Role of Regulatory T Cells in Pulmonary Arterial Hypertension. *J Am Heart Assoc*. 2019;8:e014201. doi: 10.1161/JAHA.119.014201

58. Tamosiuniene R, Tian W, Dhillon G, Wang L, Sung YK, Gera L, Patterson AJ, Agrawal R, Rabinovitch M, Ambler K, et al. Regulatory T cells limit vascular endothelial injury and prevent pulmonary hypertension. *Circ Res*. 2011;109:867-879. doi: 10.1161/CIRCRESAHA.110.236927

59. Sutendra G, Dromparis P, Wright P, Bonnet S, Haromy A, Hao Z, McMurtry MS, Michalak M, Vance JE, Sessa WC, et al. The role of Nogo and the mitochondria-endoplasmic reticulum unit in pulmonary hypertension. *Sci Transl Med*. 2011;3:88ra55. doi: 10.1126/scitranslmed.3002194

60. McMurtry MS, Archer SL, Altieri DC, Bonnet S, Haromy A, Harry G, Bonnet S, Puttagunta L, Michelakis ED. Gene therapy targeting survivin selectively induces pulmonary vascular apoptosis and reverses pulmonary arterial hypertension. *J Clin Invest*. 2005;115:1479-1491. doi: 10.1172/JCI23203

61. Michelakis ED, Sutendra G, Dromparis P, Webster L, Haromy A, Niven E, Maguire C, Gammer TL, Mackey JR, Fulton D, et al. Metabolic modulation of glioblastoma with dichloroacetate. *Sci Transl Med*. 2010;2:31ra34. doi: 10.1126/scitranslmed.3000677

62. Virtue S, Vidal-Puig A. GTTs and ITTs in mice: simple tests, complex answers. *Nat Metab*. 2021;3:883-886. doi: 10.1038/s42255-021-00414-7

63. Esterbauer H, Schneitler C, Oberkofler H, Ebenbichler C, Paulweber B, Sandhofer F, Ladurner G, Hell E, Strosberg AD, Patsch JR, et al. A common polymorphism in the promoter of UCP2 is associated with decreased risk of obesity in middle-aged humans. *Nat Genet*. 2001;28:178-183. doi: 10.1038/88911

64. Pi J, Bai Y, Daniel KW, Liu D, Lyght O, Edelstein D, Brownlee M, Corkey BE, Collins S. Persistent oxidative stress due to absence of uncoupling protein 2 associated with impaired pancreatic beta-cell function. *Endocrinology*. 2009;150:3040-3048. doi: 10.1210/en.2008-1642

65. Zhang CY, Baffy G, Perret P, Krauss S, Peroni O, Grujic D, Hagen T, Vidal-Puig AJ, Boss O, Kim YB, et al. Uncoupling protein-2 negatively regulates insulin secretion and is a major link between obesity, beta cell dysfunction, and type 2 diabetes. *Cell*. 2001;105:745-755. doi: 10.1016/s0092-8674(01)00378-6

66. Petersen KF, Dufour S, Befroy D, Garcia R, Shulman GI. Impaired mitochondrial activity in the insulin-resistant offspring of patients with type 2 diabetes. *N Engl J Med*. 2004;350:664-671. doi: 10.1056/NEJMoa031314

67. Dromparis P, Paulin R, Stenson TH, Haromy A, Sutendra G, Michelakis ED. Attenuating endoplasmic reticulum stress as a novel therapeutic strategy in pulmonary hypertension. *Circulation*. 2013;127:115-125. doi: 10.1161/CIRCULATIONAHA.112.133413

68. Ryan JJ, Marsboom G, Fang YH, Toth PT, Morrow E, Luo N, Piao L, Hong Z, Ericson K, Zhang HJ, et al. PGC1alpha-mediated mitofusin-2 deficiency in female rats and humans with pulmonary arterial hypertension. *Am J Respir Crit Care Med*. 2013;187:865-878. doi: 10.1164/rccm.201209-1687OC

69. Archer SL. Mitochondrial dynamics--mitochondrial fission and fusion in human diseases. *N Engl J Med*. 2013;369:2236-2251. doi: 10.1056/NEJMra1215233

70. Michelakis ED, Hampl V, Nsair A, Wu X, Harry G, Haromy A, Gurtu R, Archer SL. Diversity in mitochondrial function explains differences in vascular oxygen sensing. *Circ Res*. 2002;90:1307-1315. doi: 10.1161/01.res.0000024689.07590.c2

71. Jablonski RP, Kim SJ, Cheresh P, Williams DB, Morales-Nebreda L, Cheng Y, Yeldandi A, Bhorade S, Pardo A, Selman M, et al. SIRT3 deficiency promotes lung fibrosis by augmenting alveolar epithelial cell mitochondrial DNA damage and apoptosis. *FASEB J*. 2017;31:2520-2532. doi: 10.1096/fj.201601077R

72. Koshenov Z, Oflaz FE, Hirtl M, Bachkoenig OA, Rost R, Osibow K, Gottschalk B, Madreiter-Sokolowski CT, Waldeck-Weiermair M, Malli R, et al. The contribution of uncoupling protein 2 to mitochondrial Ca(2+) homeostasis in health and disease - A short revisit. *Mitochondrion*. 2020;55:164-173. doi: 10.1016/j.mito.2020.10.003

73. Mallilankaraman K, Doonan P, Cardenas C, Chandramoorthy HC, Muller M, Miller R, Hoffman NE, Gandhirajan RK, Molgo J, Birnbaum MJ, et al. MICU1 is an essential

gatekeeper for MCU-mediated mitochondrial Ca(2+) uptake that regulates cell survival. *Cell*. 2012;151:630-644. doi: 10.1016/j.cell.2012.10.011

74. Giaid A, Saleh D. Reduced expression of endothelial nitric oxide synthase in the lungs of patients with pulmonary hypertension. *N Engl J Med*. 1995;333:214-221. doi: 10.1056/NEJM199507273330403

75. Lander N, Chiurillo MA, Bertolini MS, Storey M, Vercesi AE, Docampo R. Calcium-sensitive pyruvate dehydrogenase phosphatase is required for energy metabolism, growth, differentiation, and infectivity of Trypanosoma cruzi. *J Biol Chem*. 2018;293:17402-17417. doi: 10.1074/jbc.RA118.004498

76. Smith ER, Hewitson TD. TGF-beta1 is a regulator of the pyruvate dehydrogenase complex in fibroblasts. *Sci Rep*. 2020;10:17914. doi: 10.1038/s41598-020-74919-8

77. Henderson J, Duffy L, Stratton R, Ford D, O'Reilly S. Metabolic reprogramming of glycolysis and glutamine metabolism are key events in myofibroblast transition in systemic sclerosis pathogenesis. *J Cell Mol Med*. 2020;24:14026-14038. doi: 10.1111/jcmm.16013

78. Zhang J, Chen W, Du J, Chu L, Zhou Z, Zhong W, Liu D, Huang H, Huang Y, Qiao Y, et al. RNF130 protects against pulmonary fibrosis through suppressing aerobic glycolysis by mediating c-myc ubiquitination. *Int Immunopharmacol*. 2023;117:109985. doi: 10.1016/j.intimp.2023.109985

79. Wellen KE, Hatzivassiliou G, Sachdeva UM, Bui TV, Cross JR, Thompson CB. ATP-citrate lyase links cellular metabolism to histone acetylation. *Science*. 2009;324:1076-1080. doi: 10.1126/science.1164097

80. Mizerska-Kowalska M, Slawinska-Brych A, Niedziela E, Brodovskiy V, Zdzisinska B. Alpha Ketoglutarate Downregulates the Neutral Endopeptidase and Enhances the Growth Inhibitory Activity of Thiorphan in Highly Aggressive Osteosarcoma Cells. *Molecules*. 2022;28. doi: 10.3390/molecules28010097

81. Zhang S, Xie H, Du Y, Wang B, Lan B, Wang H. DNMT1-induced miR-133b suppression via methylation promotes myocardial fibrosis after myocardial infarction. *Gen Physiol Biophys*. 2023;42:417-429. doi: 10.4149/gpb_2023018

82. Smith ER, Wigg B, Holt S, Hewitson TD. TGF-beta1 modifies histone acetylation and acetyl-coenzyme A metabolism in renal myofibroblasts. *Am J Physiol Renal Physiol*. 2019. doi: 10.1152/ajprenal.00513.2018

83. Graier WF, Trenker M, Malli R. Mitochondrial Ca2+, the secret behind the function of uncoupling proteins 2 and 3? *Cell Calcium*. 2008;44:36-50. doi: 10.1016/j.ceca.2008.01.001

84. Madreiter-Sokolowski CT, Klec C, Parichatikanond W, Stryeck S, Gottschalk B, Pulido S, Rost R, Eroglu E, Hofmann NA, Bondarenko AI, et al. PRMT1-mediated methylation of MICU1 determines the UCP2/3 dependency of mitochondrial Ca(2+) uptake in immortalized cells. *Nat Commun*. 2016;7:12897. doi: 10.1038/ncomms12897

85. Paulin R, Sutendra G, Gurtu V, Dromparis P, Haromy A, Provencher S, Bonnet S, Michelakis ED. A miR-208-Mef2 axis drives the decompensation of right ventricular function in pulmonary hypertension. *Circ Res*. 2015;116:56-69. doi: 10.1161/CIRCRESAHA.115.303910

86. Zhang Y, Zervopoulos SD, Boukouris AE, Lorenzana-Carrillo MA, Saleme B, Webster L, Liu Y, Haromy A, Tabatabaei Dakhili SA, Ussher JR, et al. SNPs for Genes Encoding the Mitochondrial Proteins Sirtuin3 and Uncoupling Protein 2 Are Associated With Disease Severity, Type 2 Diabetes, and Outcomes in Patients With Pulmonary Arterial Hypertension and This Is Recapitulated in a New Mouse Model Lacking Both Genes. *J Am Heart Assoc*. 2021;10:e020451. doi: 10.1161/JAHA.120.020451

87. Lorenzana-Carrillo MA, Gopal K, Byrne NJ, Tejay S, Saleme B, Das SK, Zhang Y, Haromy A, Eaton F, Mendiola Pla M, et al. TRIM35-mediated degradation of nuclear PKM2 destabilizes GATA4/6 and induces P53 in cardiomyocytes to promote heart failure. *Sci Transl Med*. 2022;14:eabm3565. doi: 10.1126/scitranslmed.abm3565

88. Merial C, Bouloumie A, Trocheris V, Lafontan M, Galitzky J. Nitric oxide-dependent downregulation of adipocyte UCP-2 expression by tumor necrosis factor-alpha. *Am J Physiol Cell Physiol*. 2000;279:C1100-1106. doi: 10.1152/ajpcell.2000.279.4.C1100

89. Jones DL, Haak AJ, Caporarello N, Choi KM, Ye Z, Yan H, Varelas X, Ordog T, Ligresti G, Tschumperlin DJ. TGFbeta-induced fibroblast activation requires persistent and targeted HDAC-mediated gene repression. *J Cell Sci*. 2019;132. doi: 10.1242/jcs.233486

90. Jha MK, Morrison BM. Lactate Transporters Mediate Glia-Neuron Metabolic Crosstalk in Homeostasis and Disease. *Front Cell Neurosci*. 2020;14:589582. doi: 10.3389/fncel.2020.589582

91. Liu L, MacKenzie KR, Putluri N, Maletic-Savatic M, Bellen HJ. The Glia-Neuron Lactate Shuttle and Elevated ROS Promote Lipid Synthesis in Neurons and Lipid Droplet

Accumulation in Glia via APOE/D. *Cell Metab*. 2017;26:719-737 e716. doi: 10.1016/j.cmet.2017.08.024

92. Frangogiannis N. Transforming growth factor-beta in tissue fibrosis. *J Exp Med*. 2020;217:e20190103. doi: 10.1084/jem.20190103

93. Humbert M, McLaughlin V, Gibbs JSR, Gomberg-Maitland M, Hoeper MM, Preston IR, Souza R, Waxman A, Escribano Subias P, Feldman J, et al. Sotatercept for the Treatment of Pulmonary Arterial Hypertension. *N Engl J Med*. 2021;384:1204-1215. doi: 10.1056/NEJMoa2024277

94. Walker EJ, Heydet D, Veldre T, Ghildyal R. Transcriptomic changes during TGF-beta-mediated differentiation of airway fibroblasts to myofibroblasts. *Sci Rep*. 2019;9:20377. doi: 10.1038/s41598-019-56955-1

95. Harrison RE, Berger R, Haworth SG, Tulloh R, Mache CJ, Morrell NW, Aldred MA, Trembath RC. Transforming growth factor-beta receptor mutations and pulmonary arterial hypertension in childhood. *Circulation*. 2005;111:435-441. doi: 10.1161/01.CIR.0000153798.78540.87

96. Hou J, Ma T, Cao H, Chen Y, Wang C, Chen X, Xiang Z, Han X. TNF-alpha-induced NF-kappaB activation promotes myofibroblast differentiation of LR-MSCs and exacerbates bleomycin-induced pulmonary fibrosis. *J Cell Physiol*. 2018;233:2409-2419. doi: 10.1002/jcp.26112

97. Powell DW, Mifflin RC, Valentich JD, Crowe SE, Saada JI, West AB. Myofibroblasts. I. Paracrine cells important in health and disease. *Am J Physiol*. 1999;277:C1-9. doi: 10.1152/ajpcell.1999.277.1.C1

98. Jun JI, Lau LF. Cellular senescence controls fibrosis in wound healing. *Aging (Albany NY)*. 2010;2:627-631. doi: 10.18632/aging.100201

99. van der Feen DE, Bossers GPL, Hagdorn QAJ, Moonen JR, Kurakula K, Szulcek R, Chappell J, Vallania F, Donato M, Kok K, et al. Cellular senescence impairs the reversibility of pulmonary arterial hypertension. *Sci Transl Med*. 2020;12. doi: 10.1126/scitranslmed.aaw4974